

UNIVERSITY OF STUDIES OF NAPLES FEDERICO II
DEPARTMENT OF CHEMICAL ENGINEERING



Ph.D. Thesis
in
Chemical Engineering,
Engineering of Materials and Production

XIX CYCLE

**EXPERIMENTAL AND NUMERICAL STUDY OF LIQUID JETS
INJECTED IN HIGH-DENSITY AIR CROSSFLOW**

SCIENTIFIC COMMITTEE

Prof. Eng. Antonio Cavaliere (*tutor*)
Eng. Raffaele Ragucci
Eng. Pasquale Di Martino

CANDIDATE

Eng. Alessandro Bellofiore

PH.D. COURSE SUPERVISOR

Prof. Eng. Nino Grizzuti

ACADEMIC YEAR 2005-2006

SUMMARY

CHAPTER 1. TECHNOLOGICAL FRAME OF REFERENCE.....	1
1.1. Guidelines to Gas Turbine Emissions Reduction	1
1.2. Strategies for NO _x emissions reduction	2
1.3. Towards Lean Combustion.....	6
1.4. Lean Premixed and Prevaporized Systems.....	8
CHAPTER 2. STATE OF ART.....	11
2.1. General aspects of liquid atomization	12
2.2. Liquid injection in crossflow	14
2.2.1. <i>Phenomenological description</i>	16
2.2.2. <i>Process Analysis</i>	20
2.3. Experimental investigation of liquid injection in crossflow.....	26
2.3.1. <i>Features of jets in crossflow and dimensionless parameters</i>	27
2.4. Modeling the injection of liquids in crossflow	33
CHAPTER 3. EXPERIMENTAL FACILITY AND DIAGNOSTICS	39
3.1. Experimental Facility	39
3.2. Monitoring and control of the experimental system	44
3.3. Diagnostic setup	45
CHAPTER 4. TEST CONDITIONS	49
4.1. Liquid properties	49
4.2. Test cases	50
CHAPTER 5. IMAGE STATISTICAL ANALYSIS PROCEDURES.....	61
5.1. Jet trajectory and momentum coherence breakdown	61

5.2. Morphological analysis of the spray	66
5.3. The centerline of the spray	69
5.4. Determination of the spray centerline	73
5.5. Instability and intermittency of the spray	74
CHAPTER 6. EXPERIMENTAL RESULTS	77
6.1. Qualitative study of spray morphology	77
6.1.1. <i>Modified diagnostic configuration</i>	77
6.1.2. <i>Experimental conditions for phenomenological analysis</i>	79
6.1.3. <i>Mechanisms of atomization</i>	80
6.1.4. <i>Dependence on dimensionless parameters</i>	84
6.2. Momentum breakdown and trajectory of the liquid jet.....	85
6.2.1. <i>Tests on cold sprays</i>	85
6.2.2. <i>Test on sprays injected in hot airflow</i>	88
6.2.3. <i>Empirical model for liquid jets in crossflow</i>	91
6.3. Morphology and fluctuations of the spray.....	94
6.3.1. <i>Angle of spray</i>	94
6.3.2. <i>Normalized intermittency index</i>	99
6.4. Relevance of the evaporation process	101
CHAPTER 7. DESCRIPTION OF THE ABCD MODEL	105
7.1. Mathematical Formulation.....	105
7.1.1. <i>Momentum balance</i>	105
7.1.2. <i>Jet cross-section deformation and drag forces</i>	107
7.1.3. <i>Mass balance and atomization model</i>	109
7.2. Boundary conditions.....	110
7.2.1. <i>Determination of air velocity profile</i>	110

7.3. Model validation	112
CHAPTER 8. RESULTS OF THE NUMERICAL MODEL	113
CHAPTER 9. DISCUSSION	119
9.1. Ruling mechanisms in the crossflow atomization process	120
9.2. Penetration and dispersion of the liquid jet	126
9.3. Modeling the injection of liquids in crossflowing airstreams.....	130
CHAPTER 10. CONCLUSIONS.....	133
CHAPTER 11. BIBLIOGRAPHIC REFERENCES	137

Chapter 1. TECHNOLOGICAL FRAME OF REFERENCE

1.1. Guidelines to Gas Turbine Emissions Reduction

The mitigation of gas turbine emissions in terms of their environmental impact is a priority for both air quality (local impact) and the greenhouse effect (global impact). Current environmental emission concerns center around the airport community and, if not addressed, may threaten future growth of air travel. Air traffic is rapidly increasing today and projections estimate it will have doubled by 2020. Against this background, it is essential to consider the environmental impacts of aviation to ensure in advance that such a rate of development is sustainable. The health of populations in relation to air quality and the risk of climate change linked to the effects of greenhouse gases are two major concerns. The European Union and the U.S. Environmental Protection Agency (EPA) are applying pressure on the International Civil Aviation Organization (ICAO) that regulates aircraft emissions for additional nitrogen oxide (NO_x) reductions from aircraft. The ICAO Committee on Aviation Environmental Protection (CAEP) is considering more stringent standards for engine emissions during landing and takeoff (LTO) cycle, that is to say below 900 meters altitude, as well as new standards for cruise operations.

Combustors in most commercial aircraft today meet the current 1998 ICAO LTO NO_x limits (see figure 1.1) with some margin, and concerns are increasing relative to cruise NO_x emissions effects on the ozone layer and global warming. More stringent NO_x limits could result in emissions landing fees on airlines or limited access to some countries or airports. In Europe, greater stringency in air quality directives is to be foreseen. The European Union recognized the need for NO_x reduction in aircraft engines and has set a goal of 50% for CO₂ and of 80% for NO_x emission reductions by 2020 in a report entitled "The European Aeronautics: A vision for 2020". As regards United States, NASA recently proposed an Emissions Reduction Project within the so-called Ultra-Efficient Engine Technology (UEET) Program and will work with the U.S. aero-propulsion industry to promote and develop combustion technologies to reduce NO_x emissions by 70% over

the LTO cycle from 1998 ICAO standards with no increase in other emission constituents (carbon monoxide, smoke, and unburned hydrocarbons) and with comparable NO_x reduction during cruise operations.

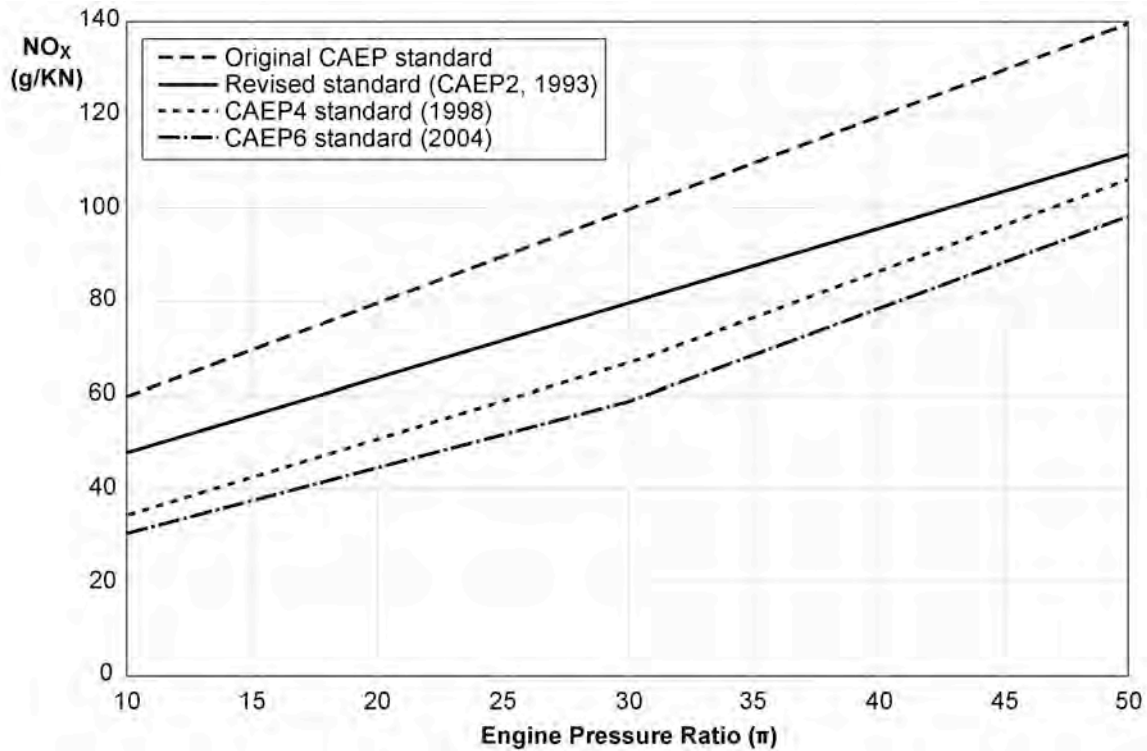


Figure 1.1. Standard limits for admitted NO_x emissions, expressed as mass of pollutant per unit of thrust. Allowed emissions increase with the engine pressure ratio.

Whereas the reduction in CO_2 (aiming to match the Kyoto protocol guidelines) will mainly be achieved by improvements in engine efficiency and aircraft performance characteristics, NO_x and others species such as CO, UHC (Unburned HydroCarbons) and particulate emissions can be significantly reduced by focusing on combustor technology, in particular by introducing new concepts for injection systems.

1.2. Strategies for NO_x emissions reduction

The problem of NO_x is mainly connected to the level of temperature reached in correspondence of the reaction zone, often referred to as primary temperature. At least as regards the thermal amount of produced nitrogen oxides, it can be stated that an increase of the primary temperature

directly makes the NO_x emissions grow. As reported in figure 1.2, the amount of emitted NO_x becomes unacceptable if the primary temperature overcomes the value of 1900 K. On the other hand it must be considered the more complex dependence of CO emissions from temperature. In order to ensure the fulfillment of the emission standards for carbon monoxide, the temperature should not be allowed being below about 1670 K. As a consequence the combustor is required to operate within a very narrow band of admitted primary temperature. Further emphasis must be placed on the local nature of this constraint, because the presence of even small regions at higher temperature would push up NO_x emissions beyond admitted limits. Finally temperature must be kept within the allowed band over the entire power range of the engine.

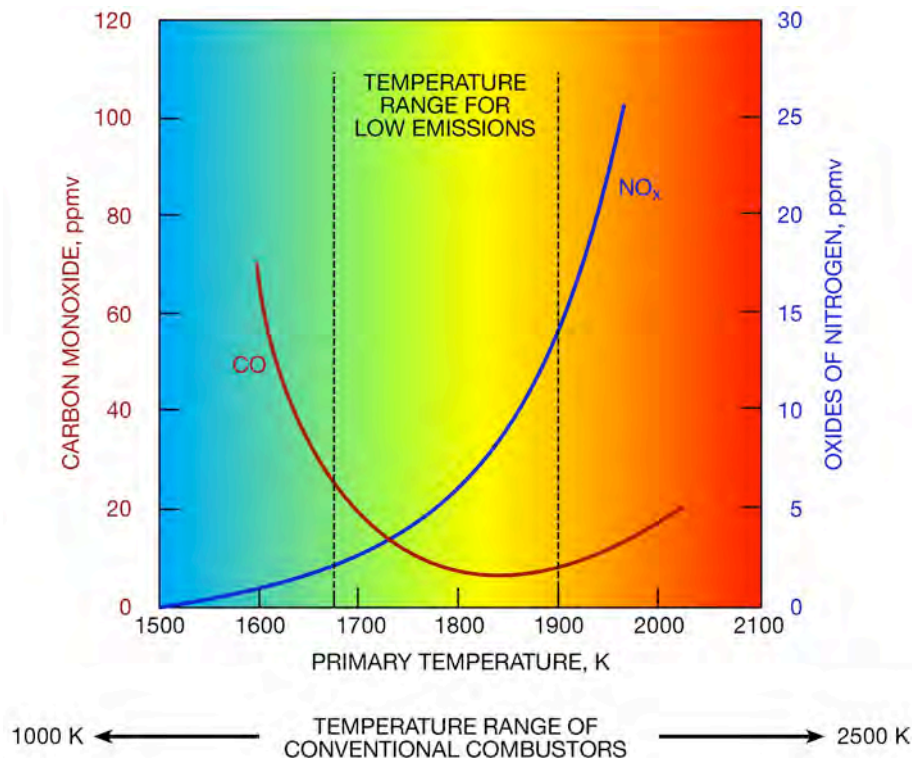


Figure 1.2. Level of emission of CO and NO_x as a function of the primary temperature reached in the reaction zone of the combustor (adapted from Lefebvre, 1995)

Several strategies for primary temperature containment have been so far developed. In order to control the temperature pattern across the combustor it is possible to introduce flexibility in the air feed system. Air distribution can be modified as the regime of the engine varies. Another classical approach is the already mentioned staged combustion, which allows switching the fuel feed from

one zone to another in dependence of the power requirement.

Wet low NO_x strategy relies on the injection of water (or steam) directly into the combustion zone, so exploiting the high thermal capacity of water to subtract heat and lower the temperature. The potential of this approach for NO_x reduction is counterbalanced by a number of drawbacks, connected to cost increase, higher fuel consumption and poorer combustor performance in terms of stability and CO and UHC emissions. In addition such kind of solution is obviously unfeasible for aircraft applications. This encouraged the development of *dry low NO_x* combustors, among which should be mentioned combustors based on the Exhaust Gas Recirculation (EGR) approach, catalytic combustors, RQL combustors and LPP combustors.

The idea to exploit a heat sink different from either water or air (this latter contains O₂ and so modifies the equivalence ratio) led to the development of the EGR approach. Exhaust gases are to the combustion zone, so realizing ultra-lean conditions in which the combustion process is sustained by the sensible enthalpy of the diluting gas (*MILD combustion*).

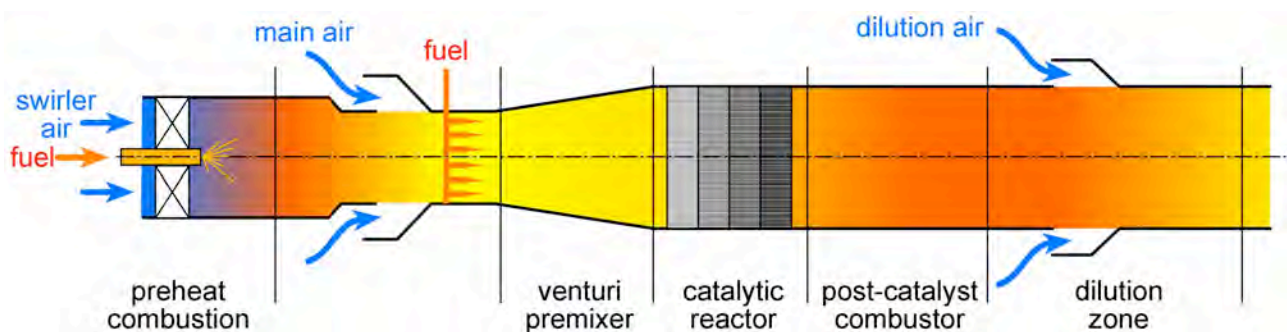


Figure 1.3. Outline of a catalytic combustor. The preliminary diffusive combustion provides preheating. Premixed conditions are realized in the venturi placed just before the catalytic reactor.

The use of catalysts to promote fuel combustion at low temperature (below 1000 K), thus preventing NO_x formation, is promising but presently unfeasible because of the very narrow range of temperature admitted for good catalyst performance and short catalyst lifetime. A possible scheme of this kind of combustor is reported in figure 1.3.

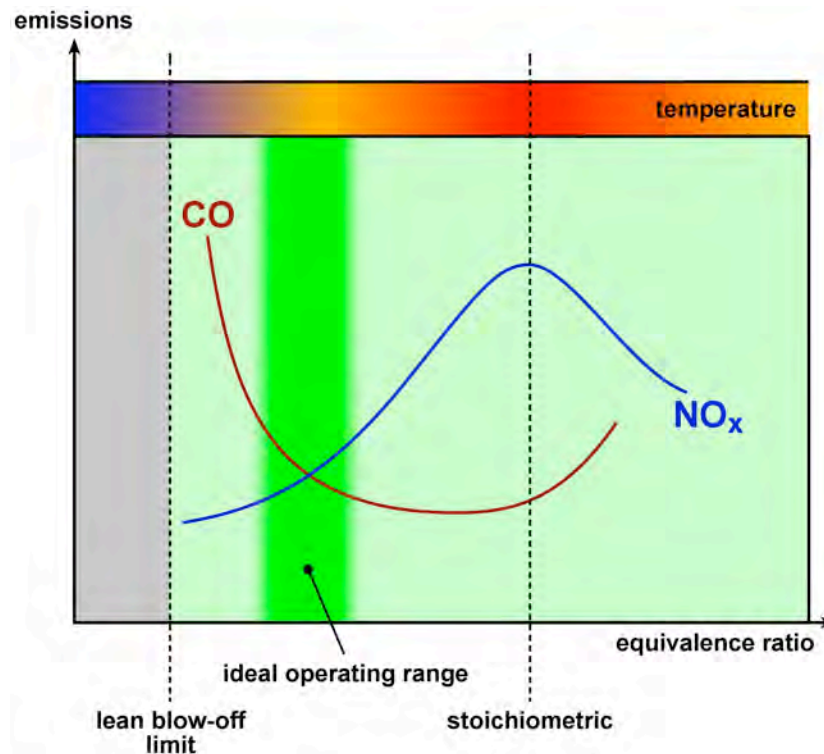


Figure 1.4. Qualitative behavior of CO and NO_x emissions as a function of the equivalence ratio. The ideal operating range refers to conditions, near the lean blow-off limit, where overall emissions are minimized.

Rich-burn, Quick-quench, Lean-burn (RQL) combustors are characterized by the presence of two separate reaction zones, operating respectively in rich and lean conditions. As it is showed in figure 1.4, where CO and NO_x emissions are plotted as a function of the equivalence ratio, the production of nitrogen oxides presents a maximum near stoichiometric conditions, because there is reached the highest temperature. The primary zone of the RQL combustor, sketched in figure 1.5, realizes rich combustion in order to lower temperature and also reduce the availability of oxygen for NO_x formation. In any case the combustion process cannot be completed with only a rich stage, also in consideration of the amount of soot produced in this zone. The process can be successfully finalized by instantaneously switching the burning conditions from rich to lean, so skipping the stoichiometric zone. The quick quench is performed by means of air jets placed in correspondence of a throat where gases speed up and so strong turbulent conditions favor rapid mixing and cooling. In addition in the design of RQL combustor the temperature in the lean zone following the quick

quench must be carefully selected in order to limit NO_x formation and, at the same time, eliminate the soot and the residual CO and UHC from the rich zone.

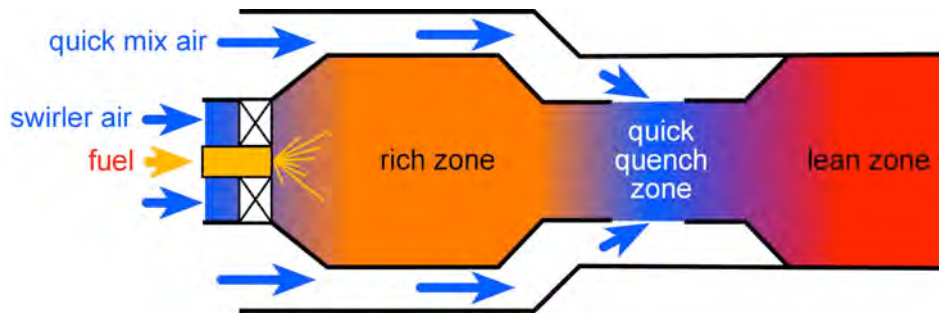


Figure 1.5 Outline of the RQL combustor

1.3. Towards Lean Combustion

Among the several new strategies for NO_x emissions containment, great interest is now focused on lean burning combustors, which are being developed and evaluated to achieve major reductions in pollutant emissions for both large and regional subsonic engines without impacting operability for safety of flight, affordability, and maintainability.

In recent decades, continuous improvements in technology have substantially reduced all the emissions from modern aircraft. This is clearly the case for CO_2 (with reductions of more than 40% in fuel burn per kg km in 40 years), for CO and UHC. These levels of reduction have been achieved by working both on engine and aircraft technology.

The latest Single Annular Combustor (SAC) generation in service combines the General Electric LEC combustor (already in service on CF6 engines and CF34), the Rolls-Royce Phase 5 combustor (already in service on Trent engines) and the P&W Talon II concept (already in service on PW4000 engines). Technology with similar emission performance levels has been developed by Snecma Moteurs for future SM146 engine, which should be certified in 2007. All these concepts are based on combustion close to stoichiometry (slightly rich or slightly lean in average in the primary zone of the combustor, depending on the technology).

The Double Annular Combustor (DAC) family of the CFM56 (-5B and -7B) is the only

technology of its kind in service, enabling even greater levels of NO_x reduction, of up to almost 50% of the current CAEP regulatory limit. By favoring sufficient lean combustion at high power (take-off), the concept also improves particulate emissions in term of smoke number (the parameter used by the regulation). The combustor is designed by General Electric. Radial staging with a pilot dome and a main dome provides greater freedom for optimizing the combustor at different regimes. In particular, the main dome operates slightly lean (under the stoichiometry) and is optimized for maximum thrust at take-off conditions. Nevertheless, this Double Annular Combustor slightly deteriorates CO and UHC emission levels in comparison with a Single Annular Combustor, particularly at low regime. In addition, the weight and complexity of the system are increased. New single annular technology with fuel staging has been therefore explored by US company General Electric with the TAPS (Twin Annular Premix System), a concept already tested on CFM56 engines. The idea is to combine the two domes into one with fuel staging using two fuel manifolds. Emission performance characteristics already show this approach to be highly promising, making it possible to reduce all types of emissions compared with a Double Annular Combustor. However CO and UHC emissions remain higher than on a conventional Single Annular Combustor engine. Operability constraints are also still to be checked. Rolls-Royce is also currently developing a similar approach with the ANTLE technology. In both the TAPS and ANTLE technology, the injection system is of the LP (*Lean Premixed*) type, which means that principally for high power the mixture is lean and premixed before reaching the reaction zone, but the fuel is not yet fully pre-vaporized.

Another alternative has been adopted with the CLEAN combustor approach developed by Snecma Moteurs, MTU and Avio Group. In this case, an axially-staged combustor is used, and the main dome is designed to achieve the best possible Lean Premixed and Pre-vaporized combustion thanks to an purposely designed injection system. The use of a Double Annular Combustor makes it easier to meet operability constraints (stability, altitude relight) and in parallel makes it possible to improve the optimization of the main dome injection system to achieve lean combustion. If

premixing and pre-vaporizing are satisfactorily accomplished, one can expect greater levels of NO_x reductions (and particulate reductions at the same time) than those demonstrated with the TAPS combustor, resulting in a reduction of more than 60% in relation to the current CAEP limit. Once again, however, CO and UHC levels increase slightly in relation to the Single Annular Combustor design, combustor mass and complexity are higher, and the cooling issue is more difficult to solve. This is the main reason why all European engine manufacturers are currently looking at fuel staging on a single annular combustor, using an LPP injection system in order to achieve a significant pollutant emission reduction along with a relatively simpler and lighter propulsion system.

1.4. Lean Premixed and Prevaporized Systems

The Lean Premixed and Prevaporized (LPP) gas turbine is a recent technological approach, promising to achieve satisfactory compromise between the demand for reliable heavy-duty engines and low NO_x emissions. The main features of these systems are the use both of large amount of air, exploiting its thermal inertia to contain the temperature and, as a consequence, the NO_x emissions, and of largely premixed burning conditions implying higher efficiencies. A successful implementation of such technology in the case of liquid fuels relies on the development of efficient and stable fast premix systems capable of dispersing, evaporating and mixing the fuel in the airflow in small time and space intervals. In fact, the efficiency of these initial stages of the process reflects on the overall performance and stability of the system as well as on the pollutant emission. Since at the actual pressures and temperatures the ignition delay time is in the order of millisecond, characteristic time and space of atomization process represent a limiting step in achieving a satisfying level of mixing before ignition occurrence. Therefore, the design of spraying system must satisfy the constraint of the highest possible effectiveness and reliability. A common technique to achieve these results makes use of one or more plain nozzles injecting liquid fuel jets perpendicularly to the high-temperature/high-pressure air current flowing in the premixing channel. The quality of the resulting spray is expected to be enhanced by the strong interaction of the jets

with the airflow whose effectiveness is even more increased due to the high air density and velocity. In addition, a good design of the jet/airflow coupling could allow for the exploitation of the strong air dragging forces in promoting an effective dispersion of fuel droplets in the premixing duct improving vaporization and mixing process. Finally, these injection schemes make use of very simple plain nozzles, assuring the highest reliability of the spraying system.

Various European technological programs have been addressing the lean combustion target. A special attention was paid to injection systems of LPP type. In particular these programs investigated LPP injection system designs covering every level of engine Overall Pressure Ratio, from OPR=15 for small engines to OPR=40 for large engines. Except for small engines, all the manufacturers were working on axially or radially-staged concepts. The main conclusion of the projects, as observed in the final reports, was that LPP technology was easier to develop for smaller OPR engines. The NO_x reduction targets were met in some cases (small engines: -50% NO_x reduction compared to conventional technology; medium engines -60% in relation to CAEP limits). Unexpected difficulties arose in the case of large engines at high pressure: a higher OPR not only increases the risk of auto-ignition but seems to generate a propensity for instability in well premixed systems. This issue is attributable to the fact that ignition delay decreases almost linearly with pressure, posing the problem that residence time in premixing duct must be further reduced as pressure grows. Airflow velocity cannot be increased, in order to prevent higher instability risks, and so the actual trend is to reduce the premixing channel length. The individuation of the oscillations sources and the development of control technologies for instability dampening are two major concerns in current studies. In particular the aim of this research is to improve the understanding of physical processes of liquid injection in intersecting airflow, in order to clarify their role in the achievement of a fast and effective dispersion of fuel before the onset of ignition.

Chapter 2. STATE OF ART

The use of lean premixed and prevaporized liquid fuel technologies for the realization of flexible, efficient and less pollutant gas turbine engines to be used in aero-propulsion and power generation systems appears to be very promising. A key task in the development of such technologies is, obviously, the preparation of the air-fuel mixture. This implies the availability of devices capable of achieving efficient atomization, mixing and vaporization sub-processes within the size and thermo-fluid-dynamical constraints of these systems. In this thesis the stress is posed on the atomization sub-process that represents the first (and probably the most relevant) stage in the fuel preparation process.

The analysis of atomization process cannot neglect the consideration of the injector geometry and of the inner and outer fluid-dynamics of the atomizers. This is due to the strong dependence of the overall process evolution both on the liquid field of motion in the peculiar geometry of the considered injector and on the subsequent interaction with the surrounding airflow. This interaction can assume a fundamental role in the determination of the efficiency of the process (as matter of facts in most cases the atomization takes place in consequence of this interaction). In this sense a general analysis is far from being feasible in the context of a PhD thesis. For these reasons in the followings only a brief introduction to the general aspects of the atomization is given. This part aims mainly to define the nomenclature that will be used in the remaining of the chapter where a deeper analysis of the liquid atomization of jet in crossflow is reported. The general approach avoids the detailed listing of the huge literature on the topics, pursuing a classical bottom-up approach, but attempts instead to rationalize the presentation of the topics trying to outline a top-down approach to the problem. This approach is quite uncommon in the atomization field, mainly because of the intrinsic complexity of the underpinning physics and for the resulting prevalence of empirical studies. Nevertheless, recent advances in the study of jets in crossflow and the reconsideration of the valuable efforts made in the field since the early fifties make now possible

this attempt.

2.1. General aspects of liquid atomization

A complete introduction to the theory of atomization and to spray systems design is out of the scope of this section. Extensive information on these topics is available in Lefebvre (1989) and Bayvel and Orzechowski (1993).

From a general point of view, atomizing a liquid means disintegrating the continuous phase in small fragments and droplets, in order to increase the liquid-gas interfacial area, thus enhancing mass and heat transfer between phases. This goal can be achieved in a number of ways, having in common the effort to provide enough energy to the liquid to overcome both the reacting forces due to surface tension and the dissipating action of liquid viscosity. From an energetic point of view the process can be viewed as an energy transfer to the liquid in order to increase its surface energy (which is essentially the product of the liquid surface tension and the extension of its interfacial area). The conversion of any kind of provided energy into surface energy is indeed an ineffective process, with efficiency generally lower than 5%, even though most of the provided energy results in increased kinetic energy of the produced droplets, which can be desirable in many applications (Nasr *et al.*, 2002). The process of transferring energy to the liquid phase is usually promoted by the onset of a relative motion between phases, inducing the arise of pressure forces and tangential stresses at the interface that counterbalance capillary pressure thus allowing for the inception and propagation of wavy disturbances. Wave crests can eventually evolve in elongated ligaments and undergo detachment from the liquid. They may, finally, grow enough to cause the liquid structure disruption. Characteristic wavelengths of the disturbances depend on numerous elements and are difficult to evaluate, both theoretically and experimentally. In any case the spectrum of frequencies of the disturbances covers a wide range, from large-scale waves producing deflection and convolution of the liquid medium, at least close to the interface, to small-scale ripples, mostly connected to the generation of a very fine spray of droplets. Amplification or dumping of a

disturbance is in general dependent upon its wavelength through a dispersion relationship that is a function both of geometrical and fluid-dynamic conditions and of liquid physical properties.

If the mechanism of energy conversion to increase the interface is essentially the one described above, the techniques utilized to provide energy to the liquid phase are as many as human inventiveness could elaborate. An attempt of classification individuated two main sources of energy: kinetic energy, provided either to liquid or gas phase or both, and mechanical energy, provided by rotating or vibrating elements in contact with the flowing liquid. This classification is somewhat scholastic, since it is possible to state that the most efficient atomization systems usually embed heterogeneous energy sources. For instance ultrasonic atomizers are often designed to carry vibrations in presence of a relative velocity between liquid and gas. In addition the reported categorization does not include some unconventional techniques, among which electrostatic atomization must be mentioned. Within the huge category of spray systems promoted by kinetic energy, a sub-classification separates *pressure* atomizers in which the kinetic energy is carried by the sole liquid phase from the so called *twin-fluid* (or *pneumatic*) atomizers, in which a significant part of the kinetic energy is provided by means of the gas phase. Further categorizations are based on the characteristics of the relative motion (*jet* or *swirl* atomizers) or, in case of pneumatic atomizers, on the order of occurrence of the liquid pressure drop (occurring in correspondence of the nozzle) and the interaction with the gas flow. This latter discrimination produces the definition of *internal mixing*, if the nozzle is placed after the interaction between phases, and *external mixing*, if placed before. Alternatively twin-fluid atomizers can be also distinguished on the basis of the features of the airflow: in the *air assisted* atomizers small amounts of gas with large dynamic pressure interact with the liquid, while the presence of larger airflow rates with moderate specific energy characterizes the definition of *air blast* atomizers.

Another relevant feature of spray systems is connected to the shape of the liquid medium undergoing atomization. It is quite obvious that a bulk of liquid with little surface/volume ratio has little or no chance to be completely atomized in a reasonably short time extent. In addition the effect

of liquid viscosity damps the propagation of disturbances into the liquid bulk. As a consequence the liquid to be atomized must be pre-arranged in order to increase the surface/volume ratio even before the occurrence of the actual atomization process. It is in general easy and little expensive (except for very viscous liquids) to reshape a liquid in form of thin sheets or jets. Liquid sheets have one size much smaller than the other two, whereas jets have two sizes smaller than the third. In both cases the disturbances arisen at the interface easily propagate to the whole medium. A general rule is that, in order to achieve an efficient atomization, the thickness of the liquid sheet or jet should be comparable to the amplitude of the interfacial perturbations with the highest amplification. Incidentally, the existence of a characteristic thickness of the liquid medium gives sense to the otherwise vague reference to large-scale and small-scale waves made before.

2.2. Liquid injection in crossflow

The above-presented classification aims to define the general frame in which the science of atomization evolved so far, as well as the reference background for the development of a specific solution for air/fuel mixture preparation in new concept gas turbines. The experience gathered by scientific and industrial research individuated some indications for the design of efficient premixer. As a result the adoption of a system based on the injection of liquid fuel in high-density air crossflow is expected to match both the opportunities and the constraints posed by the premixer design. In a LPP gas turbine a large amount of high-pressure high-temperature air flows through the premixer from the compressor to the combustion chamber. In the premixer air meets the liquid fuel, thus atomization, dispersion and evaporation processes occur and a homogeneous uniform mixture is delivered to the combustor inlet. In this scheme the premixer embeds both air passage duct and liquid supplier. The basic design of the premixer incorporates a main duct roughly aligned with the airflow, while the nozzles for liquid supply are accommodated either in the center or in the sidewalls. Actual design is quite more complex, for instance due to the use of swirlers to add centrifugal motion and increase turbulence. The complexity of such configurations induced to focus

the investigation on a simplified scheme, in which the interaction between liquid and gas could be studied in absence of convoluted airflow pattern. The theoretical motivation of this choice is the progressive approach to the study of complex phenomena, based first on the individuation of the elementary mechanisms of the investigated process, and then on the correct sorting of these mechanisms, starting from the phenomenon elected as fundamental and progressively enlarging the target to take into account concurrent phenomena. From a practical point of view a simplified test rig is of extreme usefulness, since it can provide a higher level of accessibility, for on-line diagnostics, than the complete configuration.

The simplified scheme investigated in this thesis (described in detail in section 3) holds most of the functional features of the actual reference premixer. The system can be considered as a whole a twin-fluid atomizer. In addition, since the liquid interaction with the airflow occurs after the pressure drop at the nozzle, atomization occurs by means of external mixing. It must be noted that, while the resort to pneumatic atomization systematically recurs in gas turbines, the external mixing is not the only adopted solution in that field. Some atomization schemes (Masuda and McDonell, 2006) include both internal and external mixing, and so there is a preliminary mixing between liquid and air upstream of the nozzle. From a more general point of view, in the open literature several different configurations are referred to as crossflow atomizers. For instance the papers by Inamura and Nagai (1985) and by Tanno et al. (1985) can be mentioned. The former authors investigated a twin-fluid spray system, with external mixing, in which the liquid is injected through a circular slit, surrounded by a thin annular airflow. The liquid film flows out of the slit, until it is suddenly deflected and then disintegrated by the air crossflow. Tanno et al. (1985) set up a pneumatic atomizer with internal mixing, in which just upstream of the discharge nozzle airflow and liquid jet impinge at an angle of about 135° . The violent deflection aligns the jet with the airflow direction, and then the already atomizing liquid is discharged through the nozzle.

As regards the crossflow injection configuration investigated in this thesis, the scheme is a squared channel swept by the airflow. One of the sidewalls holds a circular plain nozzle with

injection axis perpendicular to the airstream. This system design has been employed in scientific research for more than fifty years, since the first available study by Chelko (1950). Until the end of the 70's this kind of crossflow atomizer was mostly used with supersonic airstreams due to the interest for scramjet combustors. In recent decades the interest for liquid-fuelled gas turbines and other applications far from combustion purposes pushed toward the investigation of liquid injection in subsonic crossflow.

The process can be summarized as follows: the liquid jet issuing from the discharge section of the nozzle impinges on the transverse airflow and is progressively deflected until its eventual alignment with the duct axis; in the meanwhile the air drag promotes the distortion of the cross section of the jet and the stripping of small liquid fragments from the sharp edges of the bent and flattened column. A detailed phenomenological description of the injection of liquids in crossflow is the item of subsection 2.2.1, while subsection 2.2.2 introduces an attempt to evaluate the complexity of the investigated process from comparison with other atomization systems. Subsection 2.2.3 presents the macroscopic and microscopic features of the jets in crossflow, as they have been so far investigated in the open literature, along with the dimensionless parameters considered relevant for this process.

2.2.1. *Phenomenological description*

In the case, here investigated, of exclusive external mixing, the liquid issues from the nozzle as a continuous medium. In general the nozzle is required to be simple and robust, and so the discharge section can be either a circular hole or a rectangular slot. Up to date both researchers and designers seem to prefer circular holes, probably aiming to simpler design of the liquid supplier.

The characteristics of the nozzle affect the quality of the final spray in a number of ways. The main reason is that the relative velocity between liquid and gas enlarges and intensifies wavy disturbances already incepted on liquid surface. The onset of oscillatory perturbation of the interface is due to several phenomena, taking place inside the nozzle or in correspondence of the

discharge section. In case of laminar flow, the liquid would completely adhere to the inner walls of the nozzle, with all the streamlines aligned to the injection axis, the sticking to the walls implying a parabolic velocity profile. Once the liquid column issues from the nozzle, the zero-velocity boundary condition almost vanishes and the subsequent velocity profile relaxation is responsible for the onset of small instabilities on the liquid surface. The increase of discharge pressure produces higher liquid velocity and higher turbulence. In a first stage the effect of growing turbulence is a flattening of the liquid velocity profile. This should result in a more stable jet, as seems to be indicated by the existence of a range of liquid velocity (in the turbulent flow region), characterized by increasing jet breakup length (Lefebvre, 1989). On the other hand higher relative velocity means higher aerodynamic enhancement of surface instabilities, therefore by increasing the liquid velocity the breakup length reaches a maximum and then decreases due to the fact that this latter effect eventually prevails on turbulence-driven stabilization.

Another possible source of wavy disturbances is cavitation. The liquid adduction system is made up of pipelines with larger passage section than the nozzle outlet, in order to reduce liquid velocity and pressure drops down the line. As a consequence close to the discharge section of the nozzle the cross section of the liquid pipe is reduced by means of a gradual narrowing, usually referred to as taper. The possible presence of sharp edges in correspondence of the taper, together with the high velocity of the liquid, could be responsible of a low-pressure zone downstream of the sharp edge. Local evaporation of liquid generates bubbles, eventually bursting after the pressure drop at the nozzle outlet. This phenomenon strongly promotes the onset of wavy disturbances in pressure atomizers, whereas is considered less relevant in pneumatic atomizers, since liquid velocity inside the nozzle is lower. Nevertheless some authors (Sallam *et al.*, 2004) took special care of the internal design of the nozzle, arranging for supercavitating flow to reduce to a minimum the level of liquid turbulence inside the nozzle. The authors observed that in absence of crossflow the liquid issues from the nozzle as a smooth column, even at relatively high values of liquid Reynolds number. In absence of both cavitation and aerodynamic enhancement the disturbances due to the sole liquid

turbulence are too weak to self-sustain and are rapidly swept out by viscosity. This fact marks a major difference from pressure atomizer, whose successfulness strongly relies on the very high level of inner turbulence, due to the elevated injection pressure, and even more on cavitation.

In the case of pneumatic atomizers, the otherwise ineffective initial disturbances on liquid surface are quickly amplified due to the energy supplied by the air impingement and entrainment. In these conditions the liquid flows out of the nozzle as a continuous column, initially characterized by the presence of small wavy surface perturbations. The crossflow configuration implies that the liquid column passes through an orthogonal airflow, and so an intense momentum exchange takes place. Liquid entrains air due to the presence of small disturbances and, reciprocally, the air dynamic pressure amplifies these disturbances. The superimposition of aerodynamically enhanced waves spreads both wave frequency and amplitude over a wide range. The further effect of the high air density is to increase the growth rate of instabilities and also to produce a quite strong eulerian buckling load sustaining the development of asymmetric instabilities, even more amplified by the transverse energy transfer from the airflow. As a consequence the interaction between liquid and airflow is schematically referable to the so-called *second wind-induced* or *turbulent regime* rather than the *atomization regime* (Lefebvre, 1989). Even if this classification properly refers to atomization in co-flowing gas, it has been already used by Oda *et al.* (1994) as a reference scheme for crossflow atomization regimes. The analogy between the regime observed for transverse injection in a crossflow and the turbulent regime identified in the co-flowing air case is further supported by the similar dependence of liquid penetration on injection velocity. As matter of facts the approximately linear dependence, reported by many authors (Hojnacki, 1972, Yates, 1972, Baranovsky and Schetz, 1978, Chen *et al.*, 1993, Wu *et al.*, 1997, Ragucci *et al.*, 2004) is significantly closer to the linear dependence predicted for turbulent regime than to the substantial independence observed in atomization regime typical of diesel injection.

As already pointed out, the first peculiar feature of the crossflow injection configuration, with respect to coaxial pneumatic atomizers, is the macroscopic shape of the liquid jet, which is

deflected by the orthogonal airflow. In addition a stronger energy transfer from gas to liquid takes place, mainly due to the deeper air entrainment in the liquid jet. Evidence of that is the intense deceleration of the airflow due to liquid blockage, which produces a wake downstream of the liquid column. The steep gas velocity gradient around the liquid jet establishes a pressure profile substantially equivalent to the behavior of a liquid drop. By analogy it is therefore assumed that the cross section of the liquid column is stretched and deformed by the air drag analogously to what observed for drops exposed to an airflow (Taylor, 1963, Ranger and Nicholls, 1969, Igra and Takayama, 2001, Han and Tryggvason, 1999).

The complex propagation of the interface oscillations couples with the global bending of the liquid column due to the drag force exerted by the air crossflow. Schetz *et al.* (1980) hypothesize that the velocity variation of liquid windward surface due to the bending can also be responsible of the development of acceleration waves. As a result the pattern of wave propagation over the jet surface loses any regularity, showing a complicated three-dimensional structure (Inamura and Nagai, 1997). The wave amplitude growth promotes the formation of ligaments protruding from jet surface. The length of ligaments has been proved to depend on liquid viscosity that delays their rupture (Nejad and Schetz, 1983). In case of moderate aerodynamic effects, the ligament cross-sectional size determines the initial size of liquid fragments detaching from the jet basically by Rayleigh breakup mechanism (Wu and Faeth, 1993). The size distribution of liquid fragments detached from ligaments is expected to be quite wide, as spread as the wave frequency range. In case of higher air density the stronger aerodynamic effects induce a merging of Rayleigh and secondary breakup, resulting in an overall shifting of the size distribution toward lower values (Wu and Faeth, 1993). As relative velocity and gas density further grow fast short waves climb up longer waves and are the main responsible of mass shedding by means of stripping mechanisms. As a result in these extreme conditions large ligaments are not supposed to survive, and moreover ample slow waves no longer play a dominant role in the atomization process. The variegate phenomenology of concurrent bag and shear breakup observed in moderate conditions become

ineffective and the characteristics of the produced droplets only depend on the wavelength of the short ripples excited by the strong aerodynamic effects. As point of fact the balance between aerodynamic forces and capillary forces no longer affects the atomization mechanisms, but only the drop size distribution. The shape of the jet seems to undergo less column instabilities, as the distortions only act on a smaller scale producing a fine spray, mostly close to the injection point. Unfortunately the jet appears unable to sustain a pure stripping mechanism. As matter of fact at a certain distance from the nozzle the progressive loss of mass and continuity deteriorates the liquid column, until it finally breaks down into a cluster of relatively large fragments, as the results on drop size distribution presented by Becker and Hassa (2002) seem to corroborate.

2.2.2. Process Analysis

Critical aspects of any atomization process are the kinetic energy supply and the competition between aerodynamic and capillary pressure. The former issue is related to the relative amount of energy, required for liquid disintegration, provided by air and liquid. As already discussed before, this parameter strongly affects both atomizer design and atomization quality. If the liquid phase carries the burden of the whole needed energy, thus the system is a pressure atomizer. At the opposite is the case of air assisted and air blast atomizers, where the liquid is fed at relatively low velocity and the energy is provided by the air phase. The process investigated in this thesis places midway between these two extremes. For instance, being the ratio of densities of liquid and gas in the order of 100, it can be concluded that for a value of the ratio of liquid and gas momenta in the order of 100 the velocities of the two phases are locally comparable. But, since the actual q values (i.e. the ones of interest for gas turbine applications) are in the order of few tens, the velocity of the gas should be sensibly higher than the one of the liquid jet. In any case the velocity is not a measure of the energy contribution of each phase. In this sense the specific kinetic energy of the liquid phase is much higher (q times) of the energy of the gas phase. It could, thus, be concluded that the influence on the trajectory of the jet of the liquid kinetic energy should be predominant. The effect

of the aerodynamic pressure is, on the contrary, very effective in the deformation of the liquid column shape. This deformation has a twofold effect. The flattening of the column cross section increases its effective area and increases largely the effectiveness of the aerodynamic pressure in bending the liquid column. In the same time the deformation of the column is the basic step in the onset of the liquid atomization mechanisms. In particular, at lower gas velocities the deformation of the interface can proceed through the formation of bags and elongated ligaments while at higher velocities the flattening of the cross section allows for a faster and intense liquid removal by means of classical liquid stripping phenomena. In this sense the lower energetic contribution coming from the gas can be more relevant to the atomization quality than the higher one connected to the liquid velocity. As matter of facts this is, in general, the advantage of air assisted atomization systems with respect to the pressure ones: being the aerodynamic forces active directly at the interface they can be very effective in the disruption of the liquid-gas interface (i.e. in promoting liquid atomization). Liquid phase kinetic energy being distributed in the whole liquid bulk is less effective even if its role cannot be, in principle, ignored.

As a consequence the mathematical modeling of the interaction results more complex, since the kinetic content of neither phase can be neglected. The process embeds features of both air blast and pressure atomization. A simple modeling approach is further hindered by the multi-dimensional nature of the process, so that even the definition of a characteristic relative velocity is much less straightforward than in the case of coaxial pneumatic atomizers.

As regards the interplay between aerodynamic and capillary forces, the role of the curvature of the interface must be stressed. A general formulation of the pressure jump Δp_σ at the interface, due to the surface tension σ , is

$$\Delta p_\sigma = \sigma \left(\frac{1}{R_1} + \frac{1}{R_2} \right) \quad (1)$$

where R_1 and R_2 are the two principal radii of surface curvature.

The basic case of a flat liquid surface above which gas flows generating ripples and waves can be considered a zero-curvature problem. This is also the case of a thin liquid sheet, characterized by the initial lack of curvature. In these cases the airflow is parallel to the interface. Another well-investigated problem is the spherical droplet submerged in an airstream. The airflow impinges on the double curvature of the droplet, which for this very reason results more resistant than a flat surface perpendicularly hit by air. The curvature of the liquid droplet couples with the characteristic frequencies of the surface disturbances excited by the airflow, resulting in a variety of distortion and disruption mechanisms. If the excited frequencies are small, as in the case of slow airflow, an ensemble deformation of the droplet occurs, and so it eventually breaks up into few large fragments. In particular a slow airflow is able to blow into the drop, forming a bag with curvature opposite to the initial one. Stronger airflow excites higher frequencies, and so small ripples form on the drop surface. In the meanwhile the shorter time scale prevents the formation of a bag, and only a flattening of the drop occurs, due to the dynamical pressure profile surrounding it. The airflow pushes the ripples toward the sharpened edges of the flattened drop, and then strips them off as droplets much smaller than the parent.

In the case of a liquid jet, it becomes relevant if the airflow is directed parallel or normal to the jet axis. A jet is characterized by the existence of one curvature only. In the case of parallel flow, as in the case of coaxial jets, the presence of this curvature is of little importance, and the system behaves similarly to a thin sheet of liquid, the main difference being that the wavelengths of the asymmetric instability modes (Yang, 1992) are submultiples of the jet diameter. The case of airflow directed normally to the jet axis is the one considered in this thesis and is sketched in figure 2.1.

Here the existence of one curvature only (directed as ξ in figure) opposing to the airflow makes the problem different from all the others. This fact splits the atomization process into two distinct phenomena. The former is relative to the interaction between the airflow and the flat principal axis η of the jet. The primary effect of the air drag in this direction is the deflection of the jet. The momentum transfer from the gas phase causes the liquid jet to progressively bend up to complete

alignment. The secondary effect is the enhancement of surface instabilities. Promoted by air entrainment and aerodynamic drag, in the jet axis direction large-scale asymmetric oscillations can develop, thus giving snake-like appearance to the jet. As already pointed out this mechanism is effective mainly at low aerodynamic pressure. The airflow also promotes the onset and propagation of small surface waves, thus resulting in a wide range of wavelengths active on the jet windward profile. The observed phenomenology is essentially akin to coaxial injection, apart from the underlying small curvature due to the bending.

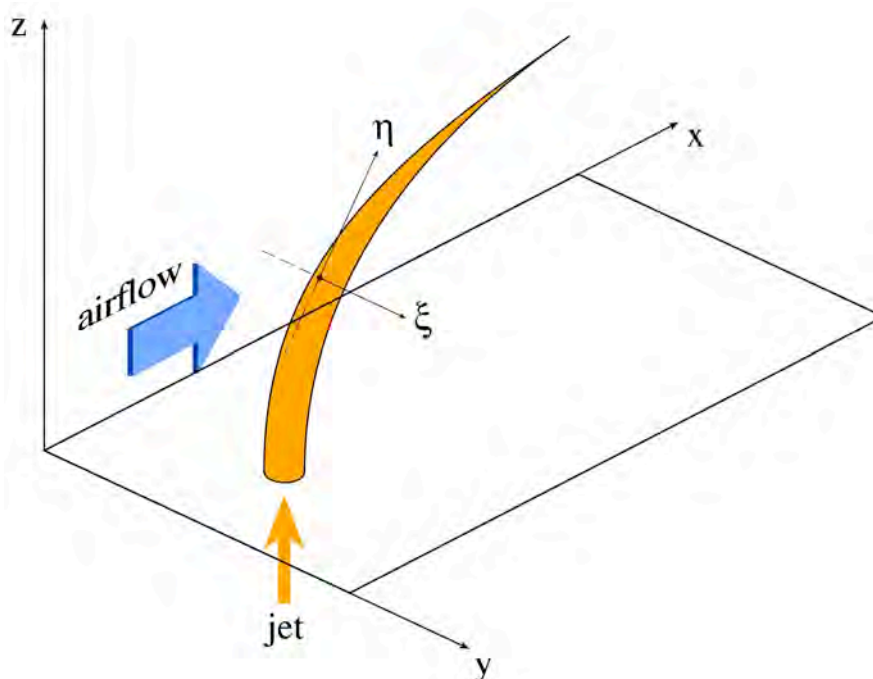


Figure 2.1. Scheme of the liquid injection in crossflow. Axes ξ and η individuate the principal directions of the liquid surface opposing to the airflow.

In the other principal direction, ξ , the initial radius of curvature of the jet is equal to the injection diameter. In this case the primary effect of the interaction with the airstream is the deformation of the initially circular cross-section of the liquid jet. Experimental investigation was so far unable to determine the kind of deformation. A flattening of the jet is supposed to occur, even if it is not clear whether the cross-section takes elliptical or lenticular shape. The secondary effect in the ξ direction again concerns the promotion of surface instabilities. This mechanism becomes

dominant at high aerodynamic pressure. In this case only high frequency disturbances grow, reproducing atomization mechanisms very similar to the ones observed in the above-described process of drop breakup (Mazallon *et al.*, 1999).

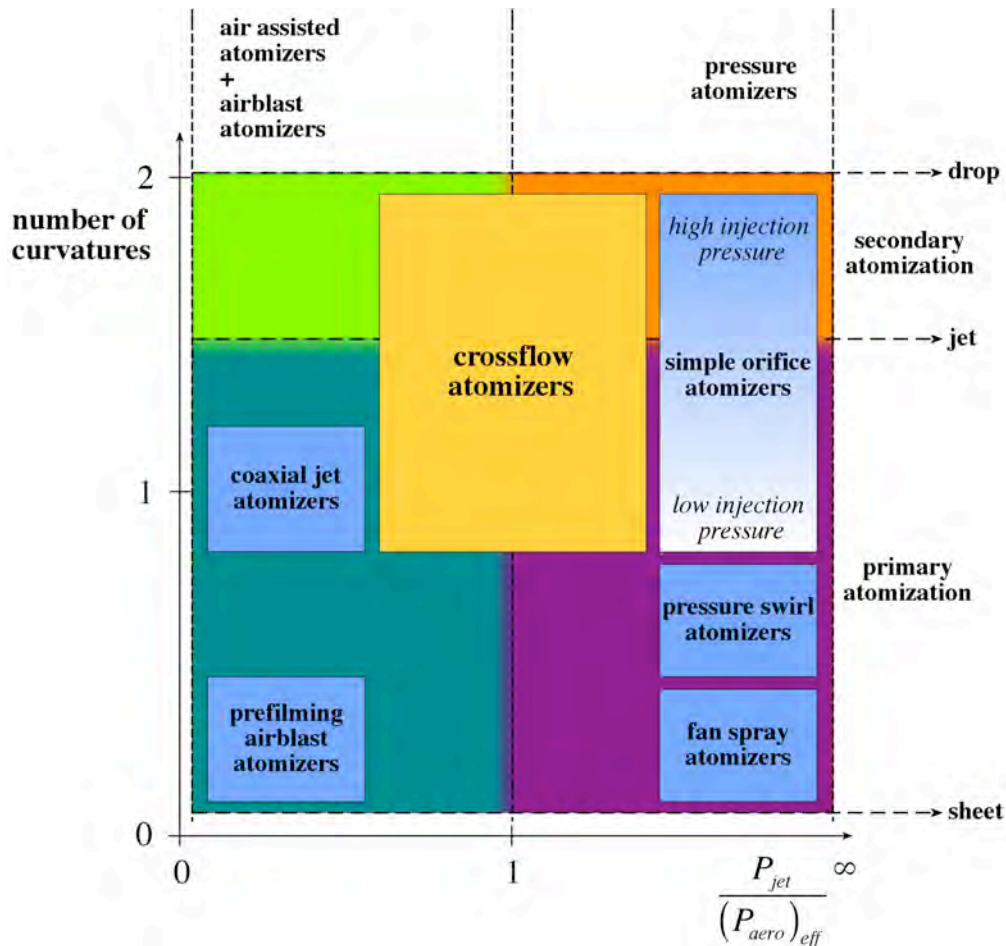


Figure 2.2. Classification of the atomization systems as a function of liquid-to-air power ratio and curvature number. The map is based on the characteristics of the primary atomization.

All the considerations made so far suggest the possibility to classify the main atomization systems in terms of curvature number and energy load partition. In a continuously flowing system the latter parameter may be expressed as liquid-to-air power ratio. The resulting plot is reported in figure 2.2. The plane is divided in four main regions, as a consequence of the partition between pressure and pneumatic atomizers (depending on the value of the power ratio) and between primary and secondary atomization (depending on the curvature number). The former division distinguishes

between systems where the air energy share is negligible with respect to liquid (pressure atomizers), and so the power ratio diverges to infinite, and pneumatic atomizers where the power ratio is close to zero, even though the liquid phase always retains a little amount of kinetic energy.

The latter separation between primary and secondary atomization is a little simplistic but very common in the open literature, and it assumes that the former step of the atomization process is the primary breakup of a liquid medium (jet or sheet) into drops, which as a secondary step can be further atomized into smaller droplets. First of all it must be stressed that in the classification here proposed the curvature number has been assigned, to each atomizer, in consideration of the primary atomization mode. In the case of jet atomizer with very high injection pressure (as for diesel-like sprays), liquid continuity is destroyed at the very nozzle outlet (Cavaliere *et al.*, 1991, Wang *et al.*, 2006), and so the so-called primary atomization involves droplet, thus the collocation of this atomizer in the top-right zone of the plot. When the same kind of injector is operated at lower pressure the atomization regime is replaced by second wind-induced regime, in which a continuous liquid jet survives the ejection from the nozzle and undergoes primary atomization. Other kinds of pressure atomizers are the *pressure swirl atomizers* in which supplying a tangential velocity component to the liquid inside the nozzle produces a conical liquid sheet, behaving midway between a jet and a flat sheet. Other pressure atomizers rely on an oblong and convergent shape of the terminal section of the injector to produce a *fan spray*, behaving like a liquid sheet. In the field of pneumatic atomizer both air assisted and air blast systems are embraced. Among the several existing designs, *prefilming air blast atomizers* are widely used in gas turbines. They aim to produce a thin liquid film stressed on both sides by airflow. Another classic scheme is the *coaxial jet air assisted atomizer*, in which the curvature number is 1.

All the presented atomizers place near the boundaries of the map. On the contrary the atomizers based on the principle of crossflow injection, as pointed out, involve features of both pressure and air blast atomizers, and moreover they partly behave as 1-curvature jets and partly as 2-curvatures droplets. As regards the liquid-to-air power ratio, it has been estimated to be, for the system

investigated in this case, of the order of unity. The same order of magnitude is expected for all the atomizers with analogous design.

2.3. Experimental investigation of liquid injection in crossflow

One of the reasons why some aspects of the process of liquid injection in crossflow are still little understood is the difficulty to experimentally study the dynamics and breakup of the jet, since the occurrence of the atomization produces large fragments and a dense aerosol of drops, enveloping the continuous jet in the near field. This fact creates serious problems to diagnostic investigation, mostly based on the collection of light scattering or extinction signal from liquid interface. In fact, the dense cloud of droplets interposing between the jet and the observing device optically obscures the liquid column. As matter of fact, the overall amount of interface of the drop cloud, which is much larger than the liquid corrugated surface, results in a high scattering intensity that masks any scattering signal coming from the liquid column interface. For the same reason diagnostics based on the detection of the extinction signal, like the shadowgraphic techniques, can only furnish a picture of the external plume of drops surroundings the jet. Further drawbacks come from the fact that the light travels through a plume with non-negligible depth, and so the occurrence of multiple scattering adds noise to the detected signal (Sedarsky *et al.*, 2006). These problems appear to be even more important for high air density conditions, where the onset of fragment detachment takes place closer to the nozzle outlet, preventing the observation of the liquid jet at all (Ragucci *et al.*, 2000, 2003, Ragucci and Cavaliere, 2002, Cavaliere *et al.*, 2003). As a consequence up to date information about jet actual behavior is really exiguous, except some particular cases where operating conditions or liquid properties reduce the atomization effectiveness to a minimum, allowing a direct observation of the liquid jet (Inamura and Nagai, 1997, Kihm *et al.*, 1995, Wu *et al.*, 1997, 1998). This difficulty is strongly evident in the problem of liquid jet cross-section deformation. Hypothesizing a substantial analogy of the liquid jet case with the well known phenomenology of gaseous jets injected in a crossflow, early works (Heister *et al.*, 1989, Nguyen and Karagozian,

1992) hypothesized that the occurrence of a progressive flattening of the liquid column, due to the acceleration of the gas flow around the jet, could induce a bow (or kidney) shape deformation of jet cross section. The experimental observation of light scattering, collected by “slicing” the jet with laser sheets, seemingly confirmed this conjecture (Ragucci and Cavaliere, 2002, Oda *et al.*, 1994), but it must be noted that in these measurements the scattering signal mainly comes from the small droplets enveloping the jet, so that even if it could be considered proved that the spray plume assumes a kidney shape, the same cannot be straightforwardly assumed true for the liquid jet cross section. The evidence collected about drop spatial distribution around the jet cross section seems to suggest the existence of a liquid stripping mechanism analogous to the shear breakup observed for atomizing drops (Pilch and Erdman, 1987), which are flattened by the airflow and so small fragments are stripped away from the bent edges of the ellipsoid. In the case of a liquid jet it is not clear yet whether high-curvature edges are attributable to the development of surface waves around the cross section or to an actual flattening of the jet. On the other hand the contribution to the droplet plume observed in the jet wakes in the leeward direction due to the dragging by the crossing airflow of already detached liquid parcel, formed in consequence of the aerodynamically induced jet atomization due to the relative velocity at the jet surface, can be hardly separated from the contribution due to the removal of liquid from the jet edges.

As regards the near field, the study of liquid jets has been usually based on image collection by means of high-speed digital cameras (Schetz *et al.*, 1980, Wu *et al.*, 1997, Becker and Hassa, 1999, 2000, 2002) and on Mie scattering data obtained by slicing the spray with a laser sheet (Ragucci *et al.*, 2000, Oda *et al.*, 1994). The use of diagnostic techniques for flow field data or single-point drop sizing is possible only outside of the dense spray region (Wu *et al.*, 1998, Becker and Hassa, 2002).

2.3.1. Features of jets in crossflow and dimensionless parameters

Although the investigation of liquid jets in crossflow suffers from diagnostic inadequacy, nonetheless the attempt to study characteristics and quality of the spray yielded the introduction of a

number of parameters and indicators. A first group is connected with macroscopical aspects of the spray. The most important of these items are probably the trajectory followed by the liquid jet and the so-called intact length of the jet. Both these parameters have been largely investigated in the open literature since the first studies in the 50's. Chelko (1950) investigated the behavior of a water jet injected into a high-velocity airstream. In particular the author focused on what he called the penetration of the jets, that is to say the windward boundary of the spray plume as it can be detected from a camera placed with line-of-sight perpendicular to the plane defined by gas and liquid injection axes. This definition of penetration refers to a curve line, roughly describing the trajectory of the liquid jet, and must not be confused with the maximum penetration of the spray, which is the height asymptotically reached by the spray. Speaking of jet penetration or trajectory is indifferent, because it can be supposed that the air drag promptly sweeps off the droplets stripped from the jet surface, and so the observed windward boundary provides a good approximation of the trajectory of the underlying jet. In addition it must be stressed that the penetration studied by Chelko and most of the following literature refers to long-exposure average images, thus neglecting the superimposed pattern of unsteadily growing disturbances. Even in recent studies, included the present thesis, a collection of short-exposure images was exploited to evaluate the average windward profile as representative of the jet penetration or trajectory.

Since this first study, it was clear the effort to seek out measurable correlations between the observed features of the jet and the operating conditions of the process, expressed in terms of dimensionless parameters in order to assure the largest significance to the proposed empirical models. The correlation proposed by Chelko was found by exploring narrow ranges of some operating conditions, even so it essentially resembles most of the correlations so far available in literature. This empirical model suggests that the coordinates of the spray windward boundary (defined as penetration parameter and mixing distance, and both made dimensionless by means of the injection diameter) are related by power-law dependence, with exponent equal to 0.22, about the half of the exponent currently accepted. Furthermore the curve scales with velocity and density of

both phases, so the final correlation is

$$\frac{l}{D} = 0.450 \left(\frac{V_L}{V_G} \right)^{0.95} \left(\frac{\rho_L}{\rho_G} \right)^{0.74} \left(\frac{s}{D} \right)^{0.22} \quad (2)$$

where on the left is the penetration parameter and on the right are, in order of appearance, the liquid-to-air velocity ratio, the density ratio and the dimensionless mixing distance. The correlation follows a scheme similar to another already employed by Callaghan and Ruggeri (1948) to describe the penetration of an air jet into a perpendicular airstream. In this study the authors assumed a simple dimensional analysis to group the process variables in few significant dimensionless parameters. In the case of gas-gas crossflow injection the analysis yielded that the penetration can be investigated by focusing on the Reynolds number, referred to the jet, the velocity ratio, the density ratio, the viscosity ratio, the dimensionless mixing distance and the dimensionless duct width. In the case of liquid injection in air crossflow the analysis by Callaghan and Ruggeri can be extended to account for the further variable surface tension. The revised set R of variables is

$$R = \{ \rho_L, \rho_G, V_L, V_G, \mu_L, \mu_G, \sigma, D, L \} \quad (3)$$

The variables above listed are density, velocity and viscosity of both phases, surface tension, nozzle diameter and duct width. The Buckingham's pi-theorem states that the number of independent variables can be reduced by assuming a suitable set of independent dimensionless parameters. The number of these parameters depends on the number of significant variables, which for the present process is 9, and the number of units involved in the variables, which are m , kg and s in the SI system. The resulting dimension matrix has rank equal to 3, therefore the number of independent dimensionless parameters is $9 - 3 = 6$. The choice of dimensionless combinations of the process variables is arbitrary, with the sole constrain of independency. Nevertheless it is preferable a selection accounting for the most important interactions taking place during the process. The experience so far gathered points to some major dimensionless groups. In fluid-dynamic problems the most relevant parameter is considered the Reynolds number, taking into

account for the interplay between inertial and viscous forces and characterizing the nature of a flow. In a two-phase problem the Reynolds number must refer to both liquid and gas phase. In addition the two phases exchange kinetic energy, and so the ratio of momenta should be considered. From the theory of atomization one of the foremost parameters is the Weber number, assessing the interaction between aerodynamic and capillary pressure. The density ratio ε is also contemplated in atomization problems (Pilch and Erdman, 1987). Finally a geometrical dimensionless parameter is the ratio δ between the characteristic length D of liquid supply and the characteristic length L of air supply. The set Π of selected dimensionless parameters is then

$$\Pi = \left\{ \begin{array}{l} Re_G = \frac{\rho_G V_G L}{\mu_G} \\ Re_L = \frac{\rho_L V_L D}{\mu_L} \\ q = \frac{\rho_L V_L^2}{\rho_G V_G^2} \\ We_G = \frac{\rho_G V_G^2 D}{\sigma} \\ \varepsilon = \frac{\rho_G}{\rho_L} \\ \delta = \frac{D}{L} \end{array} \right. \quad (4)$$

Five out of six dimensionless parameters contain exclusive variables. The exception is the liquid-to-air momentum ratio, denoted by q , which appears neither in Callaghan and Ruggeri's paper, nor in Chelko's. It is only in late 60's that the dependence of the penetration on densities and velocities took the shape of q , in some papers quoted by Gooderum and Bushnell (1972). Since that time the q number has been generally considered the main controlling parameter of the crossflow injection process, both for liquid and gas jets.

Clark (1964) employed two diagnostic techniques to investigate the behavior of a water jet in nitrogen subsonic crossflow. He explored a remarkably broad range of gas pressure, from atmospheric pressure up to about 2.0 MPa. Together with high-speed photographs of side and front

view of the spray, the author set up an equipment for measuring the electrical conduction of the water jet from the injection to a movable electrical probe screen. The higher the measured electrical resistance, the larger the degree of breakup of the jet. Although based on little quality photographs, the author describes the main phenomenological aspects of the process as they are currently supposed. In particular, from experimental data and comparison with previous knowledge about drop shattering by shock waves, he detects evidence of both bending and cross-sectional flattening of the liquid jet, and of the subsequent liquid stripping mechanism. Furthermore Clark figured out that at elevated values of both Reynolds and Weber number viscous and capillary forces are negligible, so that the inertia of the jet and the dynamic pressure of gas are mainly responsible of the jet behavior.

Ingebo (1967), in analogy to the evidence of a previous study by himself and Foster (1957) on drop size distribution in crossflow atomization, derived an empirical model correlating the penetration of a jet in crossflow to the ratio of liquid Reynolds number and gas Weber number. The presence of capillary forces is in contrast with the conclusions of Clark (1964). It can be noted that Clark did not really varied surface tension in his measurements, but only inferred, on the basis of dimensional analysis considerations, that a minor influence of surface tension should be expected. Up to date the question is still discussed. More recently surface tension was reported to have no effect on the spray penetration (Wu *et al.*, 1997), although it has been proved to affect strongly the surface wave evolution (Schetz and Nejad, 1983).

Chen *et al.* (1993) built up an empirical model of the jet trajectory based on the assumption of existence of three different zones (near field, ligament region and droplet region) which evolution needs three separate mathematical descriptions. The accurate tuning of three exponential terms allowed for the use of a single composite functional form. Reference experiments were carried out by injecting an undisclosed fuel in a up to 0.2 MPa subsonic airflow. Wu *et al.* (1997) used an even lower air pressure and injected different liquids but no fuel. The development of a simple phenomenological analysis led to empirical correlations pointing out that the jet trajectory well

resembles a square root behavior and moreover there is a dependence of the jet penetration, in the liquid-streamwise direction, on the square root of the liquid-to-air momentum ratio q . A similar dependence on q was also proposed by Chen *et al.* (1993) and Becker and Hassa (1999, 2002), even though the exponent of q was found to be slightly lower than 0.5. The latter authors also proposed a logarithmic functionality to fit the path followed by the liquid jet, as well as recently did Tambe *et al.* (2005) relying on the non-linear regression of data collected from water, jet-A and n-heptane jets in transverse airstream at atmospheric pressure and temperature.

Jet breakup is considered a main concept for the development of physically consistent modeling tools for spray behavior prediction. Nevertheless this parameter is still enveloped by a definition ambiguity, since in the atomization process more threshold events can be connected with the onset of discontinuities in the liquid phase. A similar abundance of breakup conditions has been already pointed out by Pilch and Erdman (1987) in their review on fragmentation mechanisms for liquid drops. In the case of liquid jets in crossflow, the simplest definitions of breakup are related to either the total penetration of the spray in the liquid-streamwise direction (Schetz *et al.*, 1980, Becker and Hassa, 2002, Chen *et al.*, 1993) or the occurrence of the first drop detachment from the jet column. Between these two extreme conditions, great interest has been devoted to the penetration of liquid jet as a continuous medium, and so the breakup point is placed in the zone where the jet, already bended, stressed and undergone liquid stripping from its surface as ligaments and drops, ultimately loses its continuity by breaking up in large fragments.

Along with the conceptual ambiguities, the aforementioned inability of diagnostic techniques to capture the actual jet dynamics represents a further problem to the study of jet breakup. The substantial inaccessibility of the liquid jet, mostly in the so called surface breakup regime (Wu *et al.*, 1997) promoted by high air density typical of LPP conditions, strongly hardens the task of individuating a column fracture point by means of direct inspection of spray images. Moreover even in the case of weak atomization (column breakup regime) the practice of evaluate the location of breakup by directly observing collected spray pictures appears to be largely unsatisfactory since it

suffers from subjectivity, non repeatability and furthermore it is necessarily bounded to the study of very few pictures, usually less than ten, so that experimental uncertainty due to the unsteady nature of the process is not overcome by a statistically significant sampling. Additional source of mistakes in the evaluation of breakup is provided by the presence of asymmetric waves along the jet, so that the liquid column is deeply distorted and its apparent section, such as it is captured by the observing device, can result remarkably thinned in some point resembling the occurrence of a discontinuity. Wu *et al.* (1997) used shadowgraph images to evaluate the occurrence of liquid column fracture and suggested that the liquid-streamwise coordinate of the breakup location only depends on the liquid-to-air momentum ratio q , while the gas-streamwise coordinate is independent of both the operating condition and the properties of the two phases. Tambe *et al.* (2005) came to the same conclusion, although they pointed out that, since the jet breakup location was determined by means of direct, non-rigorous observation of the liquid column fracture as captured by shadowgraph images, only images of sprays in the column breakup regime were useful to the purpose. The database in the surface breakup regime was therefore neglected and so the proposed correlation suffers of a strong validity limitation.

2.4. Modeling the injection of liquids in crossflow

The study of liquid jets in crossflow has to face several problems. The first difficulty is the above-mentioned fact that the process cannot be reduced to a one-dimensional scheme, so that the liquid bending induces a greater complexity than the injection in still or co-flowing gas. Moreover the turbulent regime places midway between the extreme cases of Rayleigh breakup and fully developed atomization, in a range of relative velocity conditions not much studied. The lack of understanding of the mechanisms characterizing this regime reflects on the lack of models for the atomization in the turbulent regime. The non-linear atomization models, developed in the last years, managed to describe liquid dynamics and breakup in the wind-induced regimes (Spangler *et al.*, 1995, Eggers, 1997, Yoon and Heister, 2004), but only under very controlled conditions, faraway

from the framework of this study. On the opposite side in the fully developed atomization regime the consistent hypothesis that the liquid jets collapses just after the nozzle outlet, due to the high relative velocity, allowed the successful development of blob models (Reitz, 1987), which should be considered unsuitable for the turbulent regime and yet are largely adopted for crossflow atomization. Another approach to overcome the lack of comprehension of this process is to presume the existence of an analogy with the injection of gas jets in an air crossflow (Heister *et al.*, 1989, Nguyen and Karagozian, 1992, Tambe *et al.*, 2005), even though it is proved that submerged jets are controlled by diffusivity and concentration gradients, while in case of liquid injection the controlling parameter is the surface tension sustaining the existence of a phase discontinuity at the interface.

One of the most difficult tasks in the preparation of modeling tools relies in the definition of a realistic general sub-model for the fuel atomization, evaporation and mixing stages. This difficulty is mainly related to the intrinsic complexity of the mathematical formulation of the problem that makes quite unrealistic a direct numerical approach to its solution. In addition, validation of the few proposed models is made difficult by the scarce availability of experimental data obtained in realistic operating conditions.

Up to date the general trend followed in the modeling of jets has been based on a lagrangian approach to represent the liquid column as a set of isolated drops issuing from the nozzle. The temporal evolution of each drop is assumed to be representative of the whole jet dynamics. This approach has been successfully used in case of liquid injected into quiescent or co-flowing gas, particularly when the high level of injection pressure actually prevents the existence of a liquid core even few diameters after the nozzle outlet (Reitz, 1987, Tanner, 1998). The main advantages of this approach are the ease of formulation of momentum balance equations, since the control volume coincides with the blob and only inertia and drag forces have to be accounted for.

The discrete blob method has been used also in the case of crossflow atomization (Rachner *et al.*, 2002, Madabhushi, 2003, Khosla and Crocker, 2004). The major drawback of this application can

be attributed to its difficulties in accounting for cohesive viscous forces responsible of the higher resistance of a liquid column with respect to a set of isolated droplets to the airflow induced bending. This problem is more important in the premixing ducts of a gas turbine engine than in a diesel engine chamber. In fact, in this latter case the higher momentum of the liquid jets induces a sudden breakup of the liquid column and the rapid formation of a cloud of droplets that can be well modeled using the discrete blob approach. The injection conditions in typical gas turbine premixing ducts are quite different from diesel injection, because of the much lower kinetic energy level of liquid. As a consequence it can be assumed that jet behavior is not the one defined as atomization regime, but it should be closer to the so-called turbulent regime. Even if this classification properly refers to atomization in coaxial gas stream (Lefebvre, 1989), it has been already used by Oda *et al.* (1994) as a reference scheme for crossflow atomization regimes. The analogy between atomization regime observed for transverse injection in a crossflow and the turbulent regime identified in the co-flowing air case is further supported by the similar dependence of liquid penetration on injection velocity. As matter of facts the approximately linear dependence, reported by many authors (Hojnacki, 1972, Yates, 1972, Baranovsky and Schetz, 1978, Chen *et al.*, 1992, Wu *et al.*, 1997, Ragucci *et al.*, 2004) is significantly closer to the linear dependence predicted for turbulent regime than to the substantial independence observed in atomization regime typical of diesel injection.

These considerations lead to the exploration of alternative approaches to model liquid jet dynamics. Apart from empirical and semi-empirical models, among models based on the resolution of balance equations the work by Adelberg (1967) should be recalled. He distinguished the case when surface wave development, leading to breakup, is dominated by either aerodynamic or capillary pressure. For both cases analytical expressions for jet trajectory and mass shedding are derived. Heister *et al.* (1989) and Nguyen and Karagozian (1992) proposed an eulerian approach for the dynamics and atomization of a liquid jet in both subsonic and supersonic crossflow. In this approach both external gaseous and internal liquid flow fields are taken into account along with the elliptical deformation of jet cross-section. Quite surprisingly in this model the effect of surface

tension is completely ruled out.

Another critical point in the description of the jet atomization behavior in presence of an air crossflow with a relevant momentum, as is the case of gas turbine premixers, is the determination of a consistent primary atomization sub-model. Several models are available in literature for the fragmentation of liquid drop and jets, but none of those was specifically thought for crossflow atomization. As a consequence, even if for secondary drop atomization the use of the standard model, developed for the co-flow case appears to be reasonable, less persuasive is to make the same assumption for the primary jet breakup modeling, since in this latter case a dominant role is played by the interaction of the liquid jet with the orthogonal airflow. In this process both the energy transfer and the interface evolution are characterized by a strong mutual interaction and develop with a more complex three-dimensional pattern than typical cases for which classical models have been built up. The peculiarity of crossflow atomization must be searched in the geometry of the jet, stressed and bended in the airflow direction, and in the strong deformation of its cross-section, which produces a pressure distribution around the liquid jet completely different from that observable in jet injected in still air. For instance one of the main problems connected to the adaptation of such models to crossflow problems is the inability to capture the effects of the strong wake settling downstream the liquid column. The wake affects the jet cross-section geometry and, as a consequence, the mechanism of drop and ligament stripping from the liquid surface.

Two major models have been developed to predict the amount of mass shed due to atomization. The first is the Kelvin-Helmholtz model (Reitz, 1987, Reitz and Bracco, 1982, Reitz and Diwakar, 1987), which deduces the mass removal rate from wavelength and growth rate of the fastest growing surface wave, calculated on the basis of a linearized stability analysis. The strong limitation to the use of this model is the presence of an experimentally evaluated parameter, mostly connected to the complex fluid-dynamics inside the nozzle. Stiesch (2003) reports that values suggested in literature for this parameter spread over a range wider than one order of magnitude.

The alternative model, which has been adopted in the present study, is the Boundary Layer

Stripping (BLS) model (Ranger and Nicholls, 1969, Delplanque and Sirignano, 1994). The basic assumption is that the mass removed from the jet coincides with the flow rate in the liquid boundary layer at the separation point, taken for simplicity as the equatorial plane normal to the airflow. Extreme ease of implementation and absence of parameters to be experimentally tuned are the major benefits of this model. On the other hand the BLS model shows some unrealistic features, as it is based on the hypothesis of circular cross-section and moreover it does not account for the influence of surface tension on the atomization process.

The evaluation of drag forces also requires a careful evaluation of the value assumed by the drag coefficient C_D . Adelberg (1967) reports a constant value of 1.2 for fully developed turbulent flow over a circular cylinder. From a simplified point of view the drag coefficient is dependent on fluid-dynamic conditions, i.e. the Reynolds number, and on the degree of flattening of the jet cross-section. In literature such a kind of correlation for elliptic geometry was investigated either for viscous flow with very small Reynolds number (Kropinski *et al.*, 1995, Dennis and Young, 2003), or for oscillating flow (Badr and Kocabiyik, 1997), or to design elliptical airfoils with zero or little angle of attack between the airflow and the major axis (Mittal and Balachandran, 1996). In all those cases the drag coefficient evaluation follows from the numerical calculation of the gas flow field. A similar procedure was implemented by Nguyen and Karagozian (1992) and resulted in a constant value of about 1.2-1.4 for high Reynolds number and low subsonic crossflow over an elliptical cylinder. Unfortunately no dependence on the degree of deformation was provided. Wu *et al.* (1997) proposed an integral model based on a strongly simplified momentum balance equation. On the basis of a regression over experimental data collected for different injected liquids, Wu *et al.* assessed C_D as about 1.7. The higher value is justified by the need to compensate the neglected effect of jet slowing down in the transverse direction, deformation and atomization, hypotheses in reasonable agreement with experimental observation in the very weak, low density crossflow studied by Wu *et al.* and far from the operating conditions of gas turbines.

Chapter 3. EXPERIMENTAL FACILITY AND DIAGNOSTICS

3.1. Experimental Facility

The scope of this work is to investigate the behavior of an atomization system, based on crossflow injection, in conditions useful to provide information about the operation of LPP gas turbine. This statement triggered the basic design of the experimental facility described in the following. The other design constrain is the possibility to have full optical access to the very injection zone, in order to explore the characteristics of the liquid jet issuing from the nozzle and interacting with the airflow.

In most cases experimental investigation can be successfully approached by assuming that a complex phenomenon can be studied as a sequential combination of elementary processes. Moving from this point of view, the first problem is the correct assumption about the scheme of interaction of the elementary process, from which follows the sequence of progressively more complex processes to be investigated. In the case studied here, it must be stressed that the focus is placed not on the very beginning stages of the atomization process, since the investigation of the flow features inside the nozzle, and how it affects the jet behavior, is neglected. Another issue that has been ruled out in this study is the investigation of the effect of realistic airflow conditions on the crossflow atomization process. As a consequence in the design of the premixer a simple rectangular channel configuration is adopted, in which velocity profile of the turbulent airflow can be assumed approximately flat, except for the slower boundary layer close to the duct sidewalls. Such configuration allows looking into a physical phenomenon, say the injection of a liquid by means of a plain nozzle into an almost air crossflow, which is suitable for both experimental optical investigation and numerical modeling. The introduction of more realistic airflow conditions is matter of future research.

With the aforementioned restrictions, the experimental facility is designed to reproduce geometry and working conditions comparable to the operation of the premixing channel of a LPP

gas turbine. A simplified sketch of the entire plant is reported in figure 3.1. Realistic conditions include, first of all, the availability of large amount of air at elevated pressure and temperature, like the airflow from the compression stage of a gas turbine. Since in the explored conditions the air mass flow rate roughly ranges between 500 and 2200 kg/h, it is necessary to operate the system in batch mode in order to match the required amount of air. As a consequence the air is compressed, by means of a 4-stages volumetric compressor, up to about 18 MPa and stored in a pressure tank of 1 m³ volume. A regulation valve (indicated in figure as main pressure reducer) attends to the lamination of the air from the storage pressure to the test pressure. The main pressure reducer is able to set the outlet pressure of the airflow at the value of static pressure of an auxiliary line. This auxiliary line, pneumatically connected to the main pressure reducer, is fed with nitrogen and is provided with a Bronkhorst pressure electronic controller, allowing accurate regulation of the static pressure. The Bronkhorst pressure regulator is made of two parts, a measuring device placed on the main streamline and a controller acting on the pressure of auxiliary line until the main pressure reaches the setpoint value. Since the lamination process implies sudden fall of gas temperature, proper working of the main regulation valve is guaranteed by keeping it in a hot water bath, capable to provide the thermal power needed for the lamination.

After the lamination valve is placed the heat-up section, consisting of a cylindrical heater provided with 18 electrical resistors and supplied by 380 V 3-phase voltage. In the adopted configuration the heater is capable to supply power up to 144 KW. A PID controller sets the power of the heater so that air temperature, measured in the test section close to liquid injection, matches the setpoint value.

The scheme in figure 3.1 shows two different inlets to the compressor. As matter of fact in some of the explored conditions kerosene is injected into airflow at temperature and pressure close or above the autoignition conditions. In order to avoid the risk of occurrence of ignition in the premixer, in potentially dangerous conditions air is replaced by a stream of pure nitrogen. Nitrogen is available, at liquid state, in refrigerated Dewar bottle. Liquid nitrogen flows into the first stage of

the compressor through an iron coil dipped in a water bath. The passage in the coil favors the evaporation of nitrogen. The required latent heat is provided by the sensible enthalpy of water. In case of operation with nitrogen, a lambda probe is inserted on the line to monitor the level of oxygen in the gas stream.

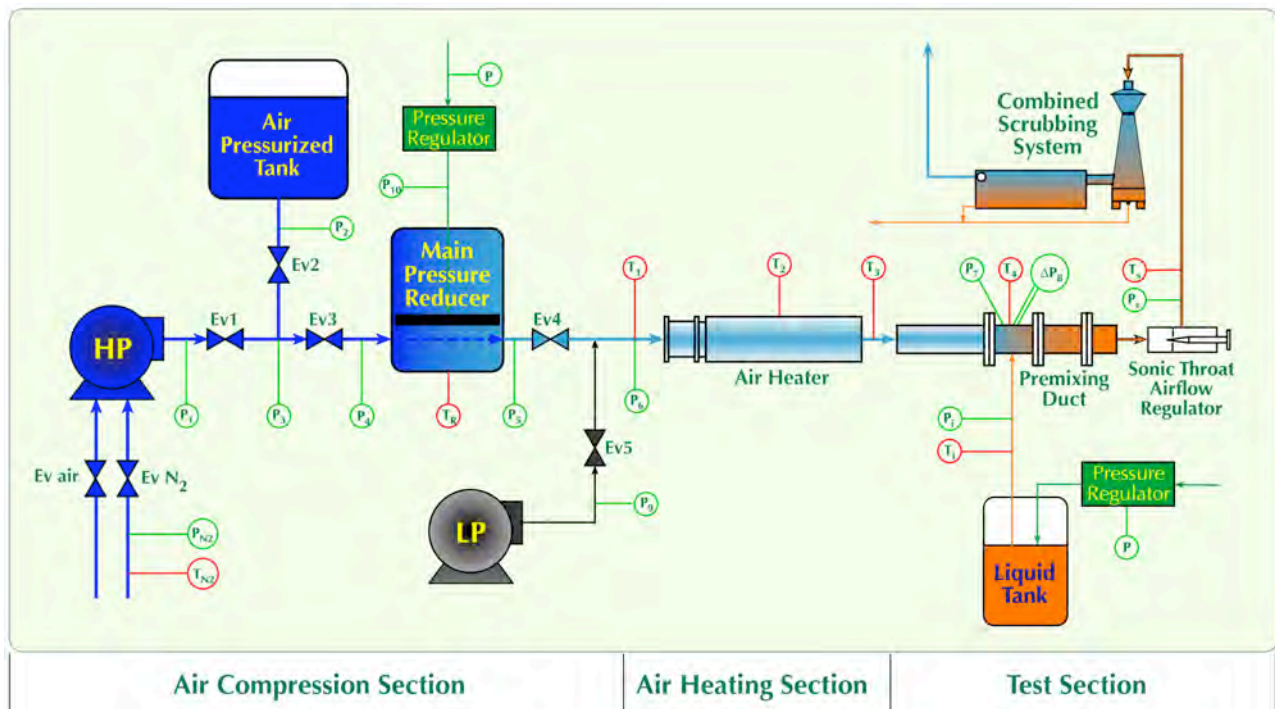


Figure 3.1. Sketch of the experimental facility.

The airflow at the required pressure and temperature finally enters the premixer. A blow-up of the test section is sketched in figure 3.2. The scheme in figure shows four elements connected by flanges. The first element is an AISI-316 stainless steel duct with circular cross-section, shielded for thermal insulation. It collects air from three inlets and is designed long enough to allow flow straightening. The circular outlet of the first element introduces air to the first of the two twin modules with rectangular 25x25 mm² cross section. Each module, in AISI-321 stainless steel, has length of 280 mm; therefore after the abrupt transition from 40 mm circular to 25 mm rectangular cross section the airflow has about 15 diameters to straighten, according to the purpose of the experimental setup to provide very simple and repeatable fluid-dynamical conditions. The velocity profiles at several axial positions in the test section were measured by using a PDA system, in

absence of the liquid jet. The obtained results show a very regular air velocity profile, which is almost flat for more than 90% of the test section.

By using a variable area diaphragm, mounted at the end of the channel and working as a sonic throttle, it was possible to regulate the gas flow rate and, hence, the airflow velocity in the test section. The regulation is actuated by an electric motor controlling the relative position of a movable conical pin and the circular outlet section of the last element of the premixer. A Pitot tube, placed in the first modular element as shown in figure 3.2, was used to monitor the air velocity in the channel midpoint during the tests.

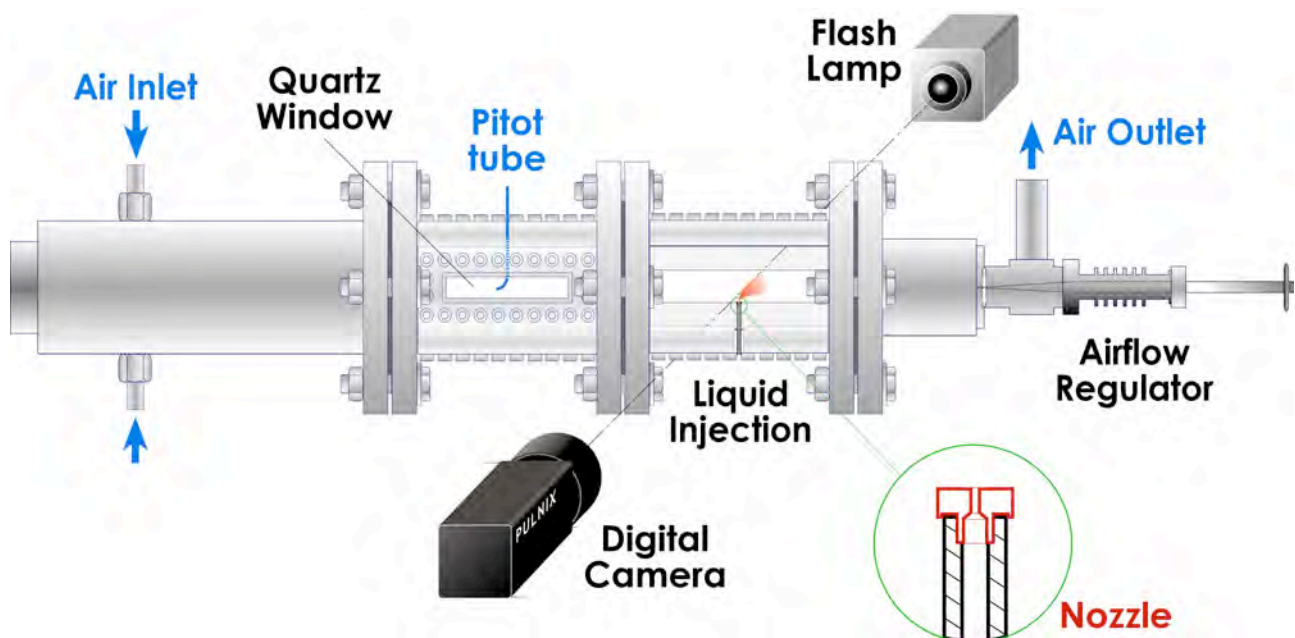


Figure 3.2. Details of the test section.

The atomizing liquid is supplied to the nozzle by means of a nitrogen-pressurized vessel and regulated by a digital pressure control valve. Adjusting the pressure in the nitrogen-pressurized reservoir it was possible to change the liquid flow rate. Nitrogen and liquid pressures are measured and controlled by means of a Bronkhorst digital controller to ensure a stable and repeatable functioning of the system. The level of nitrogen dilution in the liquid fuel, in conditions close to thermodynamic equilibrium at room temperature and 50 bars pressure (upper limit of reservoir pressurization in performed measurements), was experimentally found to be very low (Battino *et*

al., 1984). Further considerations, concerning the characteristics and operation of the pressurization system, shift the estimation of the actual value on nitrogen dilution in the fuel far from the equilibrium value and then encourage neglecting the possible effect of nitrogen dilution on fuel surface tension.

As told before, the test rig consisted of a fully accessible chamber with a square cross section of $25 \times 25 \text{ mm}^2$, capable to resist to high pressures, up to 10 MPa, and high temperatures, up to 1000 K. The test section has been designed so that three of its walls house quartz windows that ensure the observation of the whole channel. On the fourth side a plain nozzle is mounted with the axis normal to the channel streamline. The pipeline for the adduction of the liquid from the nitrogen-pressurized reservoir to the nozzle has diameter of 1.5 mm, terminating in a nozzle-holder with the same inner diameter. The nozzle, plotted in red in the blow-up in figure 3.2, is screwed onto the holder and can be easily replaced. A 45° taper introduces the liquid flow to the terminal straight section of the nozzle having a length-to-diameter aspect ratio equal to 4. Some authors cared about reducing to a minimum liquid turbulence and unsteadiness, by accurately designing a laminar flow in a supercavitating nozzle (Wu et al., 1997, Sallam et al., 2004). That way they expect to have very little instability at the nozzle outlet, mainly due to the relaxation of liquid velocity profile out of the injection tube, so that it should be possible to study the pure crossflow atomization mechanism. In this work liquid is injected in turbulent conditions comparable to the realistic operation of gas turbines.

Finally a 2-stage scrubbing system provides for cooling down and cleaning up the airflow. In the Venturi scrubber the injection of cold water reduces the air temperature and, at the same time, condenses and captures the kerosene dispersed in the airflow. Analogously in the following tank cold water is sprayed from the top, normally to the airflow. The presence of a tortuous path inside the tank improves the separation of liquid drops from the airflow.

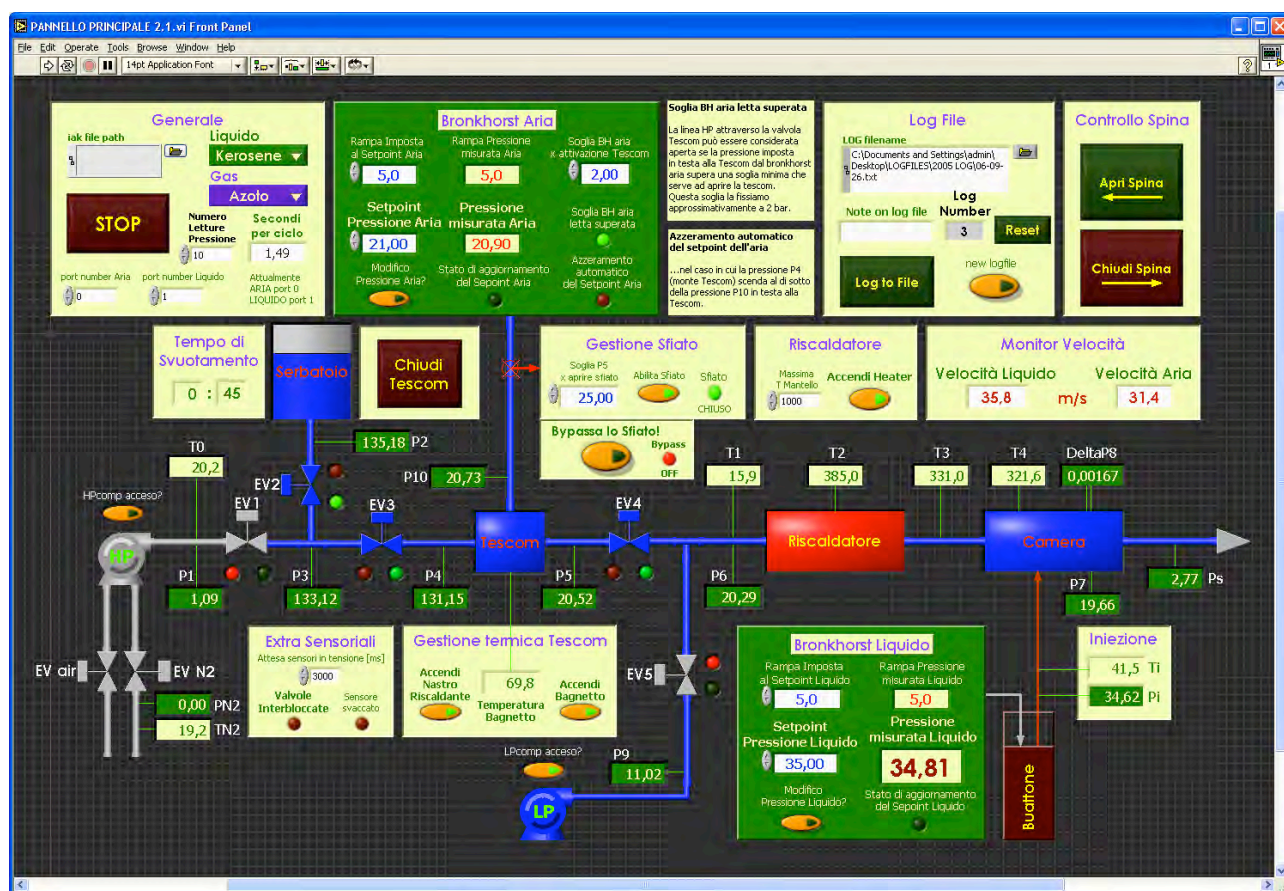


Figure 3.3. Snapshot of the control panel used for the management of the experimental system.

3.2. Monitoring and control of the experimental system

Remote operation of the facility is realized by means of two main items: the Field Point system by National Instruments for distributed signal monitoring and control and the programming environment LabVIEW (version 7.1), again by National Instruments. Field Point consists of a communication module for interfacing with a PC via Ethernet, and an array of dedicated modules for the several tasks. The adopted configuration includes modules for monitoring analog signals from pressure transducers and from K-type thermocouples, digital signals from proximity sensors, and relay modules to open and close electro-mechanic valves placed across the pneumatic line. The proximity sensors check the actual position of the valves. A digital output signal drives the electric motor controlling the movable conical pin for the airflow velocity regulation. The program also monitors a differential pressure transducer connected to the Pitot tube in the test section. A serial connection links the PC to the already mentioned Bronkhorst pressure controllers, the former for the

nitrogen auxiliary line for driving the gas static pressure in the test section, the latter for the liquid injection system, based on the nitrogen-pressurized tank. So far the LabVIEW control panel, reported in figure 3.3, only switches on and off the electrical heater, whereas the temperature regulation is performed by a separate PID control device.

Facility safety is assured by both electro-mechanical and passive-control devices, which prevent overpressure over the line. Furthermore a number of safety procedures are implemented in the control program, in order to avoid overpressure and overheating, also by automatically executing lamination valve shutting down and pressure reset in the main pneumatic line. Safe preheating of the test section, before operation in high temperature conditions, is achieved by means of an auxiliary airline fed by a low-pressure compressor. This auxiliary airflow delivers heat from the electrical heater to the test section in order to warm up the premixer, so increasing the time interval, during tests, in which gas temperature endures at the setpoint value.

Figure 3.3 reproduces the appearance of the control panel during the operation with kerosene jet-A1 injected in air crossflow at 600 K and 2.0 MPa. The high-pressure is off, since nitrogen has been previously stored in the tank at about 18 MPa. Gas flows from the tank to the test section, and the static pressure is kept constantly at the setpoint value by the Tescom lamination valve, driven by the auxiliary line, whose pressure is set at about 2.0 MPa by one of the Bronkhorst controllers. The electrical heater is on and also is the low-pressure compressor, because when the test ends up the system is promptly switched to the low pressure airflow in order to remove heat from the test section and most of all to take away any residual kerosene. The panel also shows both gas and liquid velocity, the former measured by means of the Pitot tube, the latter evaluated from the pressure drop through the injector.

3.3. Diagnostic setup

A satisfying characterization of the liquid spray would require the implementation of several on-line diagnostic systems. This PhD thesis is part of a research project in which the adoption of

multi-diagnostic approach is pursued. First of all the study of the qualitative behavior of the spray is approached by means of a flash shadowgraphic scheme, consisting of a flash lamp for illuminating the region of interest and a digital camera for collecting the light extinction signal. The use of a laser sheet source, already available in the laboratory, instead of the flash lamp will allow collecting tomograms of the spray, and so a more detailed description of liquid phase behavior should be achieved. Quantitative measurement of droplet flow field is possible by means of either a PIV (Particle Image Velocimetry) arrangement, based on a laser sheet double pulse illumination, or a LD-PDA (Laser Doppler – Phase Doppler Anemometry) system. The former system has been already used in preliminary tests and quantitative measurements in conditions of interest for gas turbine are scheduled for the next months. The further adoption of a PDA system will provide also information about drop size distribution. Size data could also be obtained by evaluating the ratio between scattering signals collected at two different polarization planes.

Up to date a shadowgraphic scheme has been set up using a low-pressure xenon flash lamp and a Pulnix 8-bit digital camera with maximum resolution of 640x480 pixels and minimum shutter time equal to 1:32000 s. Timebase generation and synchronization between these devices is managed by a BNC delay generator. An IMAQ PCI-1422 acquisition board from National Instruments was used to store the collected images. The sampling rate was fixed to the camera maximum, i.e. 240 Hz, by reducing the actual camera resolution to 640x200 pixels. The flash lamp pulse duration is equal to 15 μ s, which determines the actual exposure time. In the explored conditions liquid flows from the nozzle at velocity of several tens of meters per second, and so in time interval of 15 μ s a drop of 100 μ m, traveling at 30 m/s, is expected to shift of about 5 diameters. As a consequence collected images are not perfectly frozen, thus preventing the local study of morphological aspects.

The diagnostic technique, based on the principle of flash shadowgraphy, provides images in which a value on a gray level scale is associated to each pixel. This value accounts for the amount of light, emitted by the source and crossing the spray. As a consequence of diffusion and absorption phenomena taking place in correspondence of the liquid-gas interface of the spray droplets, light

attenuation occurs and the digital camera receives a damped signal. Light signal attenuation not only depends on the real and imaginary part of the refraction index of the media, but it gets stronger as droplet size and number along the light path is larger. The overall amount of liquid-gas interface intercepted by the light from the source to the camera contributes to light extinction, therefore it is not possible to get information about individual droplets. Furthermore the phenomenon of multiple scattering should be taken into account. The contribution of those photons, who have been scattered more than once and then reach the digital camera after a tortuous pathway, does not provide useful information about spray and should be considered as a disturbance. All the mentioned problems make it difficult to obtain quantitative information from the shadowgraphic technique. This restriction, along with the limited spatial resolution of the camera, addresses the study into two directions: in conditions where the flow velocity is low enough morphological investigation is feasible to study the structure of the convoluting jet and the mechanisms of liquid disruption; in all the explored conditions only the global morphology of the spray can be investigated, mainly focusing on liquid placement and dispersion in the premixer.

The acquisition rate of the digital camera, 240 Hz, is about two orders of magnitude lower than the estimated characteristic frequencies of the investigated phenomena. As a consequence direct temporal tracking of jet dynamics is not feasible and a statistical approach is to be adopted. For each test condition a 1000 frame sample was collected. The implementation of image statistical analysis techniques allows getting information on both spray morphological aspects, such as jet trajectory, breakdown, and liquid dispersion, and spray instability aspects, as will be shown in the following. The need for a quantitative characterization of jet behavior from the sampled images requires the implementation of a set of acquisition and elaboration procedures, written in LabVIEW programming environment and based on a standard library of image manipulation algorithms (NI-IMAQ). These techniques were firstly introduced and discussed by Ragucci and Cavaliere (2002), but in the present work the larger amount of available images provides a more statistically relevant sample, improving the performance of the analysis tools. Complete description of image statistical

analysis procedures is presented in chapter 5, after introducing, in chapter 4, a survey of the investigated operating conditions.

Chapter 4. TEST CONDITIONS

4.1. Liquid properties

Since the framework is the research on lean premixed gas turbine combustors, the liquid fuel of interest, used in the experiments here presented, is kerosene jet-A1. In addition the behavior of water jets was investigated. The two liquids have density equal to 790 Kg/m^3 for kerosene and about 1000 Kg/m^3 for water, and viscosity of $1.5 \cdot 10^{-3}$ and 10^{-3} Kg/m s , respectively. The wide difference between the two liquids as regards the surface tension, which is about 0.022 N/m for kerosene and 0.073 N/m for water at room temperature, allows covering the range of values usually encountered in atomization problems (except for molten metals). It is important to underscore that the use of such two liquids can provide reliable information on surface tension effects, whereas liquid density and viscosity vary in a quite narrow range, so that pointing out the influence of these properties is out of the scope of this study.

The formulation of correlations between breakdown point coordinates and dimensionless properties requires the estimation of air and liquid properties at the test conditions. As regards liquid properties, at room temperature the density is 1000 and 790 Kg/m^3 for water and Jet A-1, respectively. These values have been held as reference density for high temperature measurements too, since the heat-up time of the liquid jet was assessed to be not lower than the jet lifetime. The surface tension depends on the temperature at the interface between phases, which is not easy to estimate. In isothermal conditions (300 K) water and Jet A-1 have surface tension of 0.0717 N/m and 0.022 N/m (Spadaccini and TeVelde, 1982), respectively. The effect of pressure on surface tension can be neglected due to the low solubility of air in both liquids. For the reported measurements at 600 K and 2.0 MPa , the boiling temperature of water is about 485 K , below the test temperature, while for Jet A-1 it is 670 K , higher than the test temperature. It can be thus assumed that the maximum temperature that can be reached at the interface does not rise above 485 K , for water, and 600 K , for Jet A-1. An estimation of the lowest interfacial temperature can be

obtained by following the classical approach to the vaporization of a single-component drop in quiescent gas (Sirignano, 1999). Under the strong hypotheses of this model, a conservative value of the interface temperature can be assessed as 400 K for water and 450 K for Jet A-1. This estimation should be considered conservative because in the premixing duct the presence of steeper gradients, due to the relative motion between phases, allegedly pushes up the interface temperature. In the range [400,485] K the surface tension of water is comprised between 0.053 and 0.035 N/m, as calculated following the *Release on Surface Tension of Ordinary Water Substance*, issued in 2004 by the International Association for Properties of Water and Steam (IAPWS) and available on the website <http://www.iapws.org>. The same report has been followed for the value of surface tension of water at room temperature, reported above. For Jet A-1 the interval of expected interface temperature is wider, [450,600] K, and so the expected value of surface tension ranges between 0.012 and 0.003 N/m, as calculated with the equation suggested by Spadaccini and TeVelde (1982). The values of surface tension for water and Jet A-1 have been assumed equal to 0.042 and 0.0076 respectively by assuming a surface temperature equal to the average value of the two limits.

		1.0 MPa (10)	1.6 MPa (16)	2.0 MPa (20)	
		300 K (F)	600 K (C)	300 K (F)	600 K (C)
water (W)	nozzle 0.3 (3)	W3F10			W3C20
	nozzle 0.5 (5)	W5F10		W5F20	W5C20
kerosene (K)	nozzle 0.3 (3)	K3F10	K3C16		K3C20
	nozzle 0.5 (5)	K5F10		K5F20	

Table 4.1. Matrix of the investigated experimental conditions. Labels in red will be used in the following to indicate test cases.

4.2. Test cases

The airflow pressure was set at 1 and 2 MPa, while reference air temperatures were 300 and 600

K. Explored velocity ranges were 15-50 m/s for liquid injection and 20-55 m/s for airflow. Two nozzles with outlet diameter of 0.3 and 0.5 mm were used. The discharge coefficients of the nozzles were preliminarily evaluated and found to be respectively 0.75 and 0.69.

In the following *test cases* are defined by four elements: nature of liquid, nozzle outlet diameter, air temperature and pressure. Table 4.1 reports the matrix of the investigated test cases, each case represented by a red label, such as W3F10, which means a test case with water (W) injected through a 0.3 mm nozzle (3) in airflow at room temperature (F) and 1.0 MPa pressure (10). Table 1 also shows that 10 test cases were investigated, among which the case labeled K3C20, say kerosene injected through 0.3 mm nozzle in nitrogen at 600 K and 2.0 MPa, is perhaps the closes to the real gas turbine operating conditions. For each test case several experimental conditions were studied by varying both gas and liquid velocity. A total amount of 298 experimental conditions was investigated. In order to present a complete review of these conditions, table 4.2 presents the definition of the relevant dimensionless parameters, whereas tables 4.3-12 report a summary of the explored test conditions, grouped by test case, along with the values of the dimensionless parameters.

The liquid-to-air momentum ratio q ranges over almost 2 orders of magnitude, from 5 to about 300. It has been considered the main (e.g. Becker and Hassa, 2002), and in some case the only (e.g. Wu et al., 1997), dimensionless parameter affecting the crossflow atomization process. As matter of fact the q number accounts for the interaction between the inertia of the liquid jet, expressed by its dynamic pressure $\rho_L V_L^2$, and the dynamic pressure $\rho_G V_G^2$ of the gas flow, responsible of the bending drag force.

The Weber number too is expected to play a role, also in consideration of the observed similarity between the mechanisms of jet breakup in crossflow with the aerodynamic shattering of drops (Sallam et al., 2004). Dimensional analysis (Adelberg, 1967) suggests that in the present conditions the capillary waves, promoted by the relative velocity at the interface ($\approx V_L$ close to the injection point) dominate the process rather than acceleration waves due to gas dynamic pressure. As a

consequence the dimensionless parameter supposed to influence the process is the aerodynamic Weber number, formulated as reported in table 4.2. In the investigated set of experimental conditions the aerodynamic Weber number We_{aero} varies even more than q , ranging between 7 and about 1200. The values of the gas-phase Reynolds number give an indication of the turbulence intensity in the test section.

liquid-to-air momentum ratio	$q = \frac{\rho_L V_L^2}{\rho_G V_G^2}$
aerodynamic Weber number	$We_{aero} = \frac{\rho_G V_L^2 D}{\sigma}$
liquid-phase Reynolds number	$Re_L = \frac{\rho_L V_L D}{\mu_L}$
gas-phase Reynolds number	$Re_G = \frac{\rho_G V_G D}{\mu_G}$
liquid-phase Ohnesorge number	$Oh_L = \frac{\mu_L}{\sqrt{\rho_L \sigma D}}$

Table 4.2. Dimensionless parameters of interest for the crossflow atomization problem.

Liquid	Nozzle Diameter [mm]	Gas Pressure [Mpa]	Gas Temperature [K]	Gas Velocity [m/s]	Liquid Velocity [m/s]	q number	Aerodynamic Weber number	Liquid Reynolds number	Gas Reynolds number	Liquid Ohnesorge number
kerosene	0.3	0.9	304	29.5	11.7	12	16	1849	4931	0.0188
kerosene	0.3	0.9	304	29.6	14.7	19	25	2323	4948	0.0188
kerosene	0.3	1.0	305	29.5	16.6	22	35	2623	5447	0.0188
kerosene	0.3	1.0	304	29.4	18.8	28	45	2970	5460	0.0188
kerosene	0.3	1.0	305	29.5	20.6	33	54	3255	5447	0.0188
kerosene	0.3	1.0	306	29.5	23.6	44	71	3729	5416	0.0188
kerosene	0.3	0.9	317	29.7	29.3	77	95	4629	4611	0.0188
kerosene	0.3	0.9	315	29.5	31.0	87	107	4898	4632	0.0188
kerosene	0.3	0.9	306	29.5	32.0	90	117	5056	4874	0.0188
kerosene	0.3	1.0	312	29.9	34.3	92	147	5419	5305	0.0188
kerosene	0.3	0.9	314	29.4	33.6	103	126	5309	4642	0.0188
kerosene	0.3	1.0	307	29.6	36.5	105	169	5767	5403	0.0188

Table 4.3. Test conditions for kerosene jets with 0.3 mm nozzle outlet diameter, 1.0 MPa and 300 K air reference conditions (K3F10).

Liquid	Nozzle Diameter [mm]	Gas Pressure [Mpa]	Gas Temperature [K]	Gas Velocity [m/s]	Liquid Velocity [m/s]	q number	Aerodynamic Weber number	Liquid Reynolds number	Gas Reynolds number	Liquid Ohnesorge number
kerosene	0.3	1.5	590	41.5	15.2	12	81	2402	3724	0.0353
kerosene	0.3	1.6	605	33.6	14.5	16	77	2291	3085	0.0353
kerosene	0.3	1.5	592	41.4	19.8	20	138	3128	3694	0.0353
kerosene	0.3	1.5	587	41.3	27.6	39	270	4361	3737	0.0353
kerosene	0.3	1.6	605	33.7	23.0	40	194	3634	3094	0.0353
kerosene	0.3	1.6	605	26.1	18.5	43	125	2923	2396	0.0353
kerosene	0.3	1.6	607	20.2	14.3	43	75	2259	1845	0.0353
kerosene	0.3	1.5	594	41.7	31.4	51	345	4961	3700	0.0353
kerosene	0.3	1.6	605	33.7	29.0	63	308	4582	3094	0.0353
kerosene	0.3	1.5	585	41.1	35.4	65	445	5593	3740	0.0353
kerosene	0.3	1.6	605	26.0	24.2	74	215	3824	2387	0.0353
kerosene	0.3	1.5	596	41.7	38.2	75	509	6036	3680	0.0353
kerosene	0.3	1.6	606	20.3	20.6	88	155	3255	1859	0.0353
kerosene	0.3	1.5	583	41.1	41.6	90	617	6573	3762	0.0353
kerosene	0.3	1.6	608	33.8	34.6	90	436	5467	3078	0.0353
kerosene	0.3	1.4	598	41.8	45.7	115	677	7221	3423	0.0353
kerosene	0.3	1.5	580	40.8	47.0	116	791	7426	3766	0.0353
kerosene	0.3	1.6	605	26.0	31.5	125	363	4977	2387	0.0353
kerosene	0.3	1.5	603	42.2	51.4	134	910	8121	3652	0.0353
kerosene	0.3	1.5	579	40.9	52.0	141	970	8216	3786	0.0353
kerosene	0.3	1.6	606	33.7	44.1	146	711	6968	3086	0.0353
kerosene	0.3	1.5	605	42.0	55.0	156	1039	8690	3615	0.0353
kerosene	0.3	1.6	607	26.1	35.5	158	460	5609	2383	0.0353
kerosene	0.3	1.5	580	40.8	56.9	169	1159	8990	3766	0.0353
kerosene	0.3	1.5	607	33.7	49.5	197	838	7821	2885	0.0353
kerosene	0.3	1.5	604	20.3	30.2	201	314	4772	1752	0.0353
kerosene	0.3	1.6	603	25.8	41.2	216	624	6510	2382	0.0353
kerosene	0.3	1.6	606	20.0	36.3	281	482	5735	1831	0.0353
kerosene	0.3	1.6	607	25.9	47.6	289	827	7521	2365	0.0353

Table 4.4. Test conditions for kerosene jets with 0.3 mm nozzle outlet diameter, 1.6 MPa and 600 K air reference conditions (K3C16).

Liquid	Nozzle Diameter [mm]	Gas Pressure [Mpa]	Gas Temperature [K]	Gas Velocity [m/s]	Liquid Velocity [m/s]	q number	Aerodynamic Weber number	Liquid Reynolds number	Gas Reynolds number	Liquid Ohnesorge number
kerosene	0.3	1.9	564	42.9	12.1	5	68	1912	5255	0.0353
kerosene	0.3	1.9	577	37.0	14.5	11	96	2291	4364	0.0353
kerosene	0.3	1.9	570	43.1	22.8	19	240	3602	5187	0.0353
kerosene	0.3	1.9	606	25.0	14.4	24	90	2275	2718	0.0353
kerosene	0.3	1.9	581	37.2	21.9	24	217	3460	4337	0.0353
kerosene	0.3	1.9	592	31.9	19.2	25	164	3034	3605	0.0353
kerosene	0.3	1.9	576	43.5	32.4	38	480	5119	5145	0.0353
kerosene	0.3	1.9	594	32.0	24.8	42	272	3918	3597	0.0353
kerosene	0.3	1.9	573	36.8	29.1	42	389	4598	4391	0.0353
kerosene	0.3	1.9	596	32.1	28.0	54	346	4424	3588	0.0353
kerosene	0.3	1.9	585	37.4	33.3	55	499	5261	4311	0.0353
kerosene	0.3	1.9	584	43.8	39.6	57	707	6257	5063	0.0353
kerosene	0.3	1.9	606	24.8	24.5	70	261	3871	2697	0.0353
kerosene	0.3	1.9	598	32.1	32.7	74	470	5167	3568	0.0353
kerosene	0.3	1.9	606	24.9	25.5	75	282	4029	2707	0.0353
kerosene	0.3	1.9	590	37.5	39.6	78	699	6257	4262	0.0353
kerosene	0.3	1.9	593	44.1	46.5	78	959	7347	4970	0.0353
kerosene	0.3	1.9	600	32.3	35.0	84	537	5530	3570	0.0353
kerosene	0.3	2.0	595	37.7	45.3	97	955	7157	4448	0.0353
kerosene	0.3	1.8	604	44.6	52.1	103	1120	8232	4620	0.0353
kerosene	0.3	1.9	602	32.2	40.5	113	717	6399	3540	0.0353
kerosene	0.3	1.9	606	24.9	31.8	117	439	5024	2707	0.0353
kerosene	0.3	2.0	600	37.8	50.5	121	1177	7979	4398	0.0353
kerosene	0.3	1.9	603	32.3	45.1	139	888	7126	3541	0.0353
kerosene	0.3	1.9	604	32.2	46.2	147	930	7300	3520	0.0353
kerosene	0.3	1.9	605	32.3	48.0	158	1002	7584	3522	0.0353
kerosene	0.3	1.9	608	24.8	37.6	166	612	5941	2682	0.0353
kerosene	0.3	1.9	608	24.8	42.9	216	796	6778	2682	0.0353

Table 4.5. Test conditions for kerosene jets with 0.3 mm nozzle outlet diameter, 2.0 MPa and 600 K air reference conditions (K3C20).

Liquid	Nozzle Diameter [mm]	Gas Pressure [Mpa]	Gas Temperature [K]	Gas Velocity [m/s]	Liquid Velocity [m/s]	q number	Aerodynamic Weber number	Liquid Reynolds number	Gas Reynolds number	Liquid Ohnesorge number
kerosene	0.5	0.9	300	24.4	8.6	9	14	2265	6959	0.0145
kerosene	0.5	1.0	300	53.0	20.0	10	87	5267	16790	0.0145
kerosene	0.5	1.0	300	53.0	21.0	11	95	5530	16790	0.0145
kerosene	0.5	1.0	300	50.0	21.0	12	95	5530	15840	0.0145
kerosene	0.5	1.1	300	37.0	17.0	13	69	4477	12900	0.0145
kerosene	0.5	0.9	300	50.0	23.0	16	103	6057	14260	0.0145
kerosene	0.5	1.2	300	41.0	22.0	16	126	5793	15590	0.0145
kerosene	0.5	1.1	300	43.0	23.0	18	126	6057	14990	0.0145
kerosene	0.5	1.0	300	50.0	26.0	18	146	6847	15840	0.0145
kerosene	0.5	1.1	300	41.0	24.0	21	137	6320	14290	0.0145
kerosene	0.5	1.0	300	17.3	9.7	21	20	2554	5482	0.0145
kerosene	0.5	1.0	300	50.0	30.0	24	195	7900	15840	0.0145
kerosene	0.5	1.0	300	53.0	32.0	25	222	8427	16790	0.0145
kerosene	0.5	0.9	300	25.3	15.0	26	44	3950	7215	0.0145
kerosene	0.5	0.9	300	25.2	16.0	30	50	4213	7187	0.0145
kerosene	0.5	1.1	300	24.0	17.0	31	69	4477	8366	0.0145
kerosene	0.5	1.1	300	50.0	36.0	32	309	9480	17430	0.0145
kerosene	0.5	1.2	300	31.0	23.5	32	144	6188	11790	0.0145
kerosene	0.5	1.0	300	43.0	30.0	33	195	7900	13630	0.0145
kerosene	0.5	1.0	300	50.0	35.0	33	265	9217	15840	0.0145
kerosene	0.5	1.1	300	41.0	31.0	35	229	8163	14290	0.0145
kerosene	0.5	1.1	300	41.0	33.0	40	259	8690	14290	0.0145
kerosene	0.5	1.0	300	53.0	41.0	40	364	10800	16790	0.0145
kerosene	0.5	1.1	300	43.0	35.0	41	292	9217	14990	0.0145
kerosene	0.5	0.9	300	25.8	19.8	44	76	5214	7358	0.0145
kerosene	0.5	1.2	300	21.0	19.0	46	94	5003	7985	0.0145
kerosene	0.5	1.1	300	43.0	39.0	51	362	10270	14990	0.0145
kerosene	0.5	1.1	300	37.0	34.0	52	275	8953	12900	0.0145
kerosene	0.5	0.9	300	50.0	43.0	56	360	11320	14260	0.0145
kerosene	0.5	1.2	300	24.0	24.0	56	150	6320	9126	0.0145
kerosene	0.5	1.3	300	21.0	22.0	57	136	5793	8651	0.0145
kerosene	0.5	1.1	300	31.0	30.6	60	223	8058	10810	0.0145
kerosene	0.5	1.0	300	17.6	16.7	61	60	4398	5577	0.0145
kerosene	0.5	1.0	300	17.7	17.2	64	64	4529	5609	0.0145
kerosene	0.5	0.9	300	26.1	25.3	71	125	6662	7443	0.0145
kerosene	0.5	1.0	300	43.0	45.0	74	439	11850	13630	0.0145
kerosene	0.5	1.3	300	31.0	38.0	78	407	10010	12770	0.0145
kerosene	0.5	1.1	300	41.0	47.0	81	526	12380	14290	0.0145
kerosene	0.5	0.8	300	53.0	52.0	81	468	13690	13440	0.0145
kerosene	0.5	1.0	300	31.0	35.5	89	273	9348	9823	0.0145
kerosene	0.5	1.1	300	41.0	50.0	91	596	13170	14290	0.0145
kerosene	0.5	0.9	300	25.8	28.5	92	158	7505	7358	0.0145
kerosene	0.5	1.1	300	37.0	48.5	106	560	12770	12900	0.0145
kerosene	0.5	0.9	300	17.7	21.2	108	88	5583	5048	0.0145
kerosene	0.5	1.1	300	24.0	32.0	109	244	8427	8366	0.0145
kerosene	0.5	0.9	300	25.9	32.3	117	203	8506	7386	0.0145
kerosene	0.5	1.1	300	21.0	29.0	117	200	7637	7320	0.0145
kerosene	0.5	1.1	300	31.0	43.0	118	440	11320	10810	0.0145
kerosene	0.5	1.1	300	41.0	60.0	132	858	15800	14290	0.0145
kerosene	0.5	1.1	300	41.0	61.0	136	886	16060	14290	0.0145
kerosene	0.5	1.2	300	24.0	37.5	138	365	9875	9126	0.0145
kerosene	0.5	1.1	300	31.0	48.0	147	549	12640	10810	0.0145
kerosene	0.5	0.9	300	17.3	24.5	151	117	6452	4934	0.0145
kerosene	0.5	1.1	300	37.0	60.0	162	858	15800	12900	0.0145
kerosene	0.5	1.2	300	24.0	41.0	164	437	10800	9126	0.0145
kerosene	0.5	1.1	300	21.0	35.5	176	300	9348	7320	0.0145
kerosene	0.5	1.1	300	41.0	70.0	179	1167	18430	14290	0.0145
kerosene	0.5	1.1	300	31.0	54.0	186	695	14220	10810	0.0145
kerosene	0.5	1.1	300	37.0	67.0	201	1069	17640	12900	0.0145
kerosene	0.5	1.2	300	24.0	47.5	221	586	12510	9126	0.0145
kerosene	0.5	1.1	300	31.0	59.0	223	829	15540	10810	0.0145

Table 4.6. Test conditions for kerosene jets with 0.5 mm nozzle outlet diameter, 1.0 MPa and 300 K air reference conditions (K5F10).

Liquid	Nozzle Diameter [mm]	Gas Pressure [Mpa]	Gas Temperature [K]	Gas Velocity [m/s]	Liquid Velocity [m/s]	q number	Aerodynamic Weber number	Liquid Reynolds number	Gas Reynolds number	Liquid Ohnesorge number
kerosene	0.5	2.0	300	31.0	31.0	34	416	8163	19650	0.0145
kerosene	0.5	2.0	300	21.0	22.5	39	219	5925	13310	0.0145
kerosene	0.5	2.0	300	21.0	30.0	69	390	7900	13310	0.0145
kerosene	0.5	1.9	300	31.0	45.0	75	833	11850	18660	0.0145
kerosene	0.5	1.9	300	31.0	45.5	77	852	11980	18660	0.0145
kerosene	0.5	2.1	300	21.0	35.5	92	573	9348	13970	0.0145
kerosene	0.5	1.9	300	31.0	50.0	93	1029	13170	18660	0.0145
kerosene	0.5	2.0	300	21.0	43.3	144	812	11400	13310	0.0145
kerosene	0.5	2.0	300	21.0	48.7	182	1027	12820	13310	0.0145

Table 4.7. Test conditions for kerosene jets with 0.5 mm nozzle outlet diameter, 2.0 MPa and 300 K air reference conditions (K5F20).

Liquid	Nozzle Diameter [mm]	Gas Pressure [Mpa]	Gas Temperature [K]	Gas Velocity [m/s]	Liquid Velocity [m/s]	q number	Aerodynamic Weber number	Liquid Reynolds number	Gas Reynolds number	Liquid Ohnesorge number
water	0.3	0.9	287	43.1	15.2	11	10	4560	7978	0.0068
water	0.3	0.9	287	43.2	19.4	18	17	5820	7996	0.0068
water	0.3	1.0	300	27.7	14.5	23	10	4350	5267	0.0068
water	0.3	1.0	300	30.9	16.7	25	13	5010	5875	0.0068
water	0.3	0.9	300	31.0	16.5	27	12	4950	5305	0.0068
water	0.3	0.9	288	43.2	23.6	27	25	7080	7947	0.0068
water	0.3	1.0	300	36.2	23.4	36	26	7020	6883	0.0068
water	0.3	0.9	289	43.4	30.6	46	42	9180	7935	0.0068
water	0.3	0.9	300	27.4	19.9	50	17	5970	4689	0.0068
water	0.3	1.0	300	30.8	23.6	50	27	7080	5856	0.0068
water	0.3	0.9	290	43.4	34.9	59	54	10470	7886	0.0068
water	0.3	0.9	300	36.0	29.6	64	38	8880	6160	0.0068
water	0.3	0.9	300	35.9	32.8	79	47	9840	6143	0.0068
water	0.3	0.9	296	43.8	42.7	89	80	12810	7675	0.0068
water	0.3	1.0	295	43.7	45.9	93	103	13770	8560	0.0068
water	0.3	1.0	300	35.9	37.6	94	68	11280	6826	0.0068
water	0.3	0.7	300	23.6	22.5	111	17	6750	3141	0.0068
water	0.3	0.9	294	43.6	48.9	117	106	14670	7732	0.0068
water	0.3	0.9	300	35.9	41.4	126	74	12420	6143	0.0068
water	0.3	0.9	293	43.5	51.8	132	119	15540	7761	0.0068
water	0.3	0.9	291	43.4	53.1	138	126	15930	7838	0.0068
water	0.3	0.9	300	35.5	45.1	153	88	13530	6075	0.0068
water	0.3	0.9	300	35.5	47.9	173	99	14370	6075	0.0068
water	0.3	0.9	300	35.4	49.6	187	106	14880	6057	0.0068
water	0.3	0.9	300	35.3	51.0	198	113	15300	6040	0.0068

Table 4.8. Test conditions for water jets with 0.3 mm nozzle outlet diameter, 1.0 MPa and 300 K air reference conditions (W3F10).

Liquid	Nozzle Diameter [mm]	Gas Pressure [Mpa]	Gas Temperature [K]	Gas Velocity [m/s]	Liquid Velocity [m/s]	q number	Aerodynamic Weber number	Liquid Reynolds number	Gas Reynolds number	Liquid Ohnesorge number
water	0.3	2.0	581	20.9	10.3	20	9	3090	2565	0.0089
water	0.3	1.9	581	28.2	14.7	24	18	4410	3288	0.0089
water	0.3	2.0	579	27.7	15.7	27	21	4710	3419	0.0089
water	0.3	2.0	559	24.4	14.1	27	18	4230	3193	0.0089
water	0.3	2.0	570	24.4	14.0	27	17	4200	3091	0.0089
water	0.3	2.0	585	28.3	19.4	39	32	5820	3434	0.0089
water	0.3	1.9	584	27.9	19.7	44	32	5910	3225	0.0089
water	0.3	2.0	562	24.5	19.4	50	34	5820	3178	0.0089
water	0.3	1.9	570	24.5	19.0	51	30	5700	2949	0.0089
water	0.3	2.0	581	20.8	19.4	72	32	5820	2553	0.0089
water	0.3	1.9	590	28.5	25.9	73	54	7770	3239	0.0089
water	0.3	2.0	590	20.1	19.1	76	31	5730	2405	0.0089
water	0.3	2.0	593	28.5	27.2	77	63	8160	3381	0.0089
water	0.3	1.9	591	28.2	27.1	82	59	8130	3196	0.0089
water	0.3	2.0	564	24.6	25.1	84	56	7530	3172	0.0089
water	0.3	1.9	570	24.5	24.5	86	50	7350	2949	0.0089
water	0.3	2.0	578	24.7	27.5	102	66	8250	3058	0.0089
water	0.3	2.0	579	20.8	23.8	108	49	7140	2567	0.0089
water	0.3	2.0	596	28.2	32.8	115	90	9840	3318	0.0089
water	0.3	1.9	566	24.7	29.0	117	71	8700	3008	0.0089
water	0.3	2.0	570	24.4	30.3	125	81	9090	3091	0.0089
water	0.3	2.0	584	20.0	25.6	136	56	7680	2434	0.0089
water	0.3	1.9	598	28.7	36.0	141	103	10800	3190	0.0089
water	0.3	2.0	581	24.6	33.1	150	95	9930	3019	0.0089
water	0.3	2.0	590	20.0	27.9	164	66	8370	2393	0.0089
water	0.3	2.0	602	28.7	39.7	164	131	11910	3321	0.0089
water	0.3	2.0	581	20.8	29.3	164	74	8790	2553	0.0089
water	0.3	1.9	571	24.8	34.9	170	102	10470	2976	0.0089
water	0.3	2.0	604	28.3	40.1	173	133	12030	3257	0.0089
water	0.3	2.0	569	24.7	37.4	186	123	11220	3138	0.0089
water	0.3	1.9	570	24.4	38.0	207	121	11400	2937	0.0089
water	0.3	2.0	580	20.8	34.6	229	103	10380	2560	0.0089
water	0.3	2.0	586	20.0	36.0	271	111	10800	2420	0.0089
water	0.3	1.9	570	24.4	43.4	271	157	13020	2937	0.0089
water	0.3	1.9	570	24.5	45.3	292	171	13590	2949	0.0089

Table 4.9. Test conditions for water jets with 0.3 mm nozzle outlet diameter, 2.0 MPa and 600 K air reference conditions (W3C20).

Liquid	Nozzle Diameter [mm]	Gas Pressure [Mpa]	Gas Temperature [K]	Gas Velocity [m/s]	Liquid Velocity [m/s]	q number	Aerodynamic Weber number	Liquid Reynolds number	Gas Reynolds number	Liquid Ohnesorge number
water	0.5	0.8	300	40.5	10.5	7	7	5250	10270	0.0052
water	0.5	1.3	300	39.4	13.2	7	18	6600	16230	0.0052
water	0.5	1.0	300	34.9	10.8	8	9	5400	11060	0.0052
water	0.5	0.8	300	53.0	15.2	9	15	7600	13440	0.0052
water	0.5	1.0	300	53.0	19.4	11	30	9700	16790	0.0052
water	0.5	0.9	300	39.5	14.6	13	15	7300	11270	0.0052
water	0.5	0.8	300	35.6	13.5	15	12	6750	9025	0.0052
water	0.5	1.0	300	52.6	23.2	17	43	11600	16670	0.0052
water	0.5	1.0	300	35.5	16.9	19	23	8450	11250	0.0052
water	0.5	1.0	300	52.6	28.1	24	63	14050	16670	0.0052
water	0.5	1.0	300	54.2	33.1	32	88	16550	17170	0.0052
water	0.5	0.8	300	30.7	16.9	32	18	8450	7783	0.0052
water	0.5	1.0	300	38.5	23.7	32	45	11850	12200	0.0052
water	0.5	0.9	300	35.1	20.5	32	30	10250	10010	0.0052
water	0.5	0.9	300	60.4	35.4	33	90	17700	17230	0.0052
water	0.5	1.0	300	29.1	19.3	38	30	9650	9221	0.0052
water	0.5	1.0	300	35.6	24.2	40	47	12100	11280	0.0052
water	0.5	0.9	300	31.0	20.0	40	29	10000	8841	0.0052
water	0.5	1.0	300	39.0	26.6	40	57	13300	12360	0.0052
water	0.5	1.0	300	24.7	17.0	41	23	8500	7827	0.0052
water	0.5	1.0	300	35.1	24.3	41	47	12150	11120	0.0052
water	0.5	0.9	300	53.2	35.1	41	89	17550	15170	0.0052
water	0.5	0.9	300	55.4	40.0	50	115	20000	15800	0.0052
water	0.5	1.0	300	24.3	18.7	51	28	9350	7700	0.0052
water	0.5	0.8	300	62.8	43.9	52	124	21950	15920	0.0052
water	0.5	1.0	300	29.6	23.6	54	45	11800	9380	0.0052
water	0.5	0.9	300	35.1	26.7	55	51	13350	10010	0.0052
water	0.5	1.1	300	35.3	30.4	58	81	15200	12300	0.0052
water	0.5	0.8	300	53.5	39.3	58	99	19650	13560	0.0052
water	0.5	0.9	300	39.8	31.2	58	70	15600	11350	0.0052
water	0.5	0.9	300	36.1	28.5	59	59	14250	10300	0.0052
water	0.5	1.1	300	40.5	35.6	60	112	17800	14120	0.0052
water	0.5	1.0	300	39.7	33.5	61	90	16750	12580	0.0052
water	0.5	1.0	300	35.8	30.5	62	75	15250	11340	0.0052
water	0.5	0.9	300	57.0	46.3	63	155	23150	16260	0.0052
water	0.5	1.0	300	39.9	34.4	64	95	17200	12640	0.0052
water	0.5	0.7	300	63.7	47.5	68	127	23750	14130	0.0052
water	0.5	1.0	300	29.1	26.0	68	54	13000	9221	0.0052
water	0.5	1.0	300	35.6	32.8	73	86	16400	11280	0.0052
water	0.5	0.9	300	40.8	36.1	74	94	18050	11640	0.0052
water	0.5	1.1	300	57.2	56.2	75	278	28100	19940	0.0052
water	0.5	1.0	300	40.2	38.5	78	119	19250	12740	0.0052
water	0.5	1.0	300	35.9	35.2	82	99	17600	11380	0.0052
water	0.5	1.0	300	40.9	40.2	83	129	20100	12960	0.0052
water	0.5	0.9	300	56.8	53.0	83	203	26500	16200	0.0052
water	0.5	1.0	300	25.5	25.3	84	51	12650	8080	0.0052
water	0.5	1.0	300	32.0	33.2	92	88	16600	10140	0.0052
water	0.5	0.9	300	30.1	29.8	93	64	14900	8584	0.0052
water	0.5	0.9	300	24.7	24.7	95	44	12350	7044	0.0052
water	0.5	0.8	300	36.0	35.9	106	83	17950	9126	0.0052
water	0.5	1.0	300	25.5	28.5	107	65	14250	8080	0.0052
water	0.5	0.9	300	39.9	43.0	110	133	21500	11380	0.0052
water	0.5	0.9	300	36.0	39.6	115	113	19800	10270	0.0052
water	0.5	0.9	300	29.9	35.0	130	88	17500	8527	0.0052
water	0.5	1.0	300	25.2	32.4	141	84	16200	7985	0.0052
water	0.5	0.9	300	30.3	38.0	150	104	19000	8641	0.0052
water	0.5	1.0	300	28.8	42.4	185	144	21200	9126	0.0052
water	0.5	1.1	300	24.2	38.3	195	129	19150	8435	0.0052

Table 4.10. Test conditions for water jets with 0.5 mm nozzle outlet diameter, 1.0 MPa and 300 K air reference conditions (W5F10).

Liquid	Nozzle Diameter [mm]	Gas Pressure [Mpa]	Gas Temperature [K]	Gas Velocity [m/s]	Liquid Velocity [m/s]	q number	Aerodynamic Weber number	Liquid Reynolds number	Gas Reynolds number	Liquid Ohnesorge number
water	0.5	1.9	300	39.2	20.8	13	66	10400	23600	0.0052
water	0.5	2.1	300	28.8	17.9	16	54	8950	19160	0.0052
water	0.5	2.0	300	33.6	22.7	20	83	11350	21290	0.0052
water	0.5	1.8	300	39.0	27.3	23	107	13650	22240	0.0052
water	0.5	2.0	300	38.8	30.8	27	152	15400	24590	0.0052
water	0.5	2.0	300	25.5	23.0	35	85	11500	16160	0.0052
water	0.5	1.6	300	39.3	33.1	38	140	16550	19930	0.0052
water	0.5	1.9	300	25.0	23.9	41	87	11950	15050	0.0052
water	0.5	1.9	300	34.0	34.1	45	177	17050	20470	0.0052
water	0.5	2.0	300	39.2	46.6	60	348	23300	24840	0.0052
water	0.5	2.0	300	28.9	34.6	61	192	17300	18320	0.0052
water	0.5	2.1	300	38.9	49.2	65	407	24600	25890	0.0052
water	0.5	1.6	300	39.3	43.8	66	246	21900	19930	0.0052
water	0.5	1.9	300	34.2	41.7	67	265	20850	20590	0.0052
water	0.5	1.9	300	28.8	41.4	93	261	20700	17340	0.0052
water	0.5	1.9	300	33.3	48.4	95	357	24200	20050	0.0052
water	0.5	1.9	300	28.6	47.4	124	342	23700	17220	0.0052

Table 4.11. Test conditions for water jets with 0.5 mm nozzle outlet diameter, 2.0 MPa and 300 K air reference conditions (W5F20).

Liquid	Nozzle Diameter [mm]	Gas Pressure [Mpa]	Gas Temperature [K]	Gas Velocity [m/s]	Liquid Velocity [m/s]	q number	Aerodynamic Weber number	Liquid Reynolds number	Gas Reynolds number	Liquid Ohnesorge number
water	0.5	1.9	547	39.5	15.8	13	36	7900	8486	0.0069
water	0.5	1.9	512	51.2	21.5	14	72	10750	12290	0.0069
water	0.5	1.9	617	28.5	11.5	15	17	5750	5014	0.0069
water	0.5	2.0	625	27.6	12.9	19	22	6450	5003	0.0069
water	0.5	1.9	558	38.4	19.3	21	53	9650	7980	0.0069
water	0.5	1.9	537	39.1	20.9	23	65	10450	8663	0.0069
water	0.5	2.0	615	28.2	14.8	24	30	7400	5250	0.0069
water	0.5	1.9	529	51.4	28.8	25	124	14400	11680	0.0069
water	0.5	1.9	559	40.1	25.7	34	94	12850	8309	0.0069
water	0.5	1.9	578	39.3	25.3	36	88	12650	7703	0.0069
water	0.5	1.9	615	28.4	18.1	37	42	9050	5023	0.0069
water	0.5	1.8	544	52.1	36.2	42	181	18100	10700	0.0069
water	0.5	2.0	614	28.4	19.7	42	53	9850	5301	0.0069
water	0.5	1.9	614	28.5	20.5	48	54	10250	5054	0.0069
water	0.5	1.9	595	40.7	31.5	53	132	15750	7603	0.0069
water	0.5	1.9	581	40.9	32.6	55	145	16300	7948	0.0069
water	0.5	1.9	615	28.5	22.3	56	64	11150	5041	0.0069
water	0.5	1.9	616	28.3	22.3	57	64	11150	4992	0.0069
water	0.5	1.9	531	37.8	32.4	59	157	16200	8533	0.0069
water	0.5	2.0	614	28.6	23.9	61	78	11950	5339	0.0069
water	0.5	1.8	548	52.8	45.0	63	278	22500	10710	0.0069
water	0.5	1.9	617	28.6	25.2	72	82	12600	5031	0.0069
water	0.5	1.9	514	37.2	36.2	73	202	18100	8868	0.0069
water	0.5	1.9	629	27.7	26.0	83	85	13000	4720	0.0069

Table 4.12. Test conditions for water jets with 0.5 mm nozzle outlet diameter, 2.0 MPa and 600 K air reference conditions (W5C20).

Chapter 5. IMAGE STATISTICAL ANALYSIS PROCEDURES

5.1. Jet trajectory and momentum coherence breakdown

Jet breakup location is considered a major concept for the development of physically consistent modeling tools for spray behavior prediction. Nevertheless, this parameter is still enveloped by a definition ambiguity, since in the atomization process the onset of discontinuities in the liquid phase can produce several observable phenomena, as already pointed out in chapter 2. Along with the conceptual ambiguities, the aforementioned inability of diagnostic techniques to capture the actual jet dynamics represents a further problem to the study of jet breakup. The substantial inaccessibility of the liquid jet, mostly in the so called surface breakup regime (Wu et al., 1997) promoted by high air density typical of LPP conditions, makes difficult the task of individuating a column fracture point by means of direct inspection of spray images. Moreover even in the case of weak atomization (column breakup regime) the practice of evaluating the location of breakup by directly observing collected spray pictures appears to be largely unsatisfactory since it suffers from subjectivity and non-repeatability. In addition the available data have been obtained from ensembles of a limited number of pictures so that experimental uncertainty due to the unsteady nature of the process is not overcome by a statistically significant sampling. Additional source of mistakes in the evaluation of breakup is provided by the presence of asymmetric waves along the jet, so that the liquid column is deeply distorted resembling in some points the occurrence of a discontinuity.

The liquid jet momentum coherence breakdown concept was firstly introduced by Ragucci and Cavaliere (2002) as an attempt to overcome both conceptual ambiguities and experimental uncertainties. The non-theoretical definition is based on the implementation of an image statistical analysis procedure, which evaluates the occurrence of a sudden collapse of jet resilience to the unsettling action of propagating interface waves. The present work presents a fully automatic, and then repeatable, routine developed to evaluate the occurrence and location of the coherence breakdown point. A further advantage is the possibility of using a suitably large image sample,

reducing uncertainties due to statistical fluctuations.

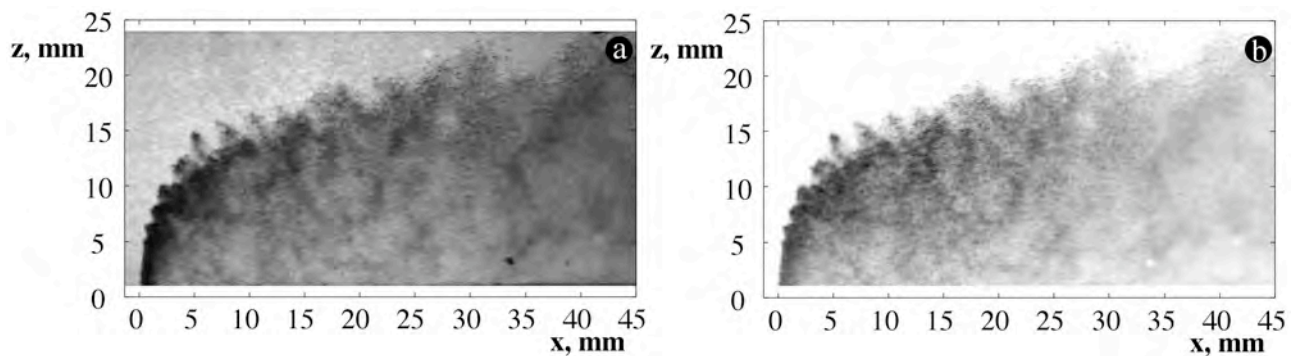


Figure 5.1. Example of the clean-up procedure based on the background image removal. Image a is as collected by the digital camera, while image b results from the subtraction to the background image. The spray is kerosene injected by a 0.3 mm nozzle in airflow at 1.1 MPa pressure and 300 K temperature. Liquid velocity is 22 m/s and air velocity is 21 m/s.

As a first step for image elaboration, for each measurement a background image is collected and then used to clean up the spray images, increasing the signal-to-noise ratio and removing the disturbance due to elements intercepting the light path by not belonging to the spray. Figure 5.1 shows an example of this procedure, which improves the image labeled as 5.1a, by subtracting it pixel by pixel from the background image. The result is reported in figure 5.1b. These pictures also show the loss of few millimeters at both top and bottom part of the image, due to the presence of stray light reflected by the channel sidewalls.

The spray windward profile is extracted by applying a threshold to binarize the single frame. The result is a 1-bit image with only two kinds of pixel: the background pixels, whose extinction signal is lower than the threshold value, and the spray pixels, whose extinction signal is higher. Scanning the image row by row from left to right and collecting for each row the first pixel of the spray provides an approximation of the windward boundary of the spray, even though the collected pixels do not represent a continuous line.

Figures 5.2a and 5.2c show single frames of a kerosene spray as collected by the digital camera for air velocity of 21 m/s and liquid velocity of 36 and 22 m/s, respectively. Both frames are

characterized by a regular development of instabilities along the jet, but it should be noted that for each condition only part of the 1000 frames collected show such regularity, since the presence of unsteady phenomena, probably connected to eddy shedding, causes the jet to flutter. Moreover the camera frame rate results to be too low to capture the dynamics of both jet fluttering and surface wave growth, so that quantitative information cannot be obtained about characteristic frequencies. An attempt to record images with an high speed camera (up to 5000 fps) to determine the characteristic frequencies of jet waving and surface waves displacement demonstrated that they are higher than the camera maximum frame rate.

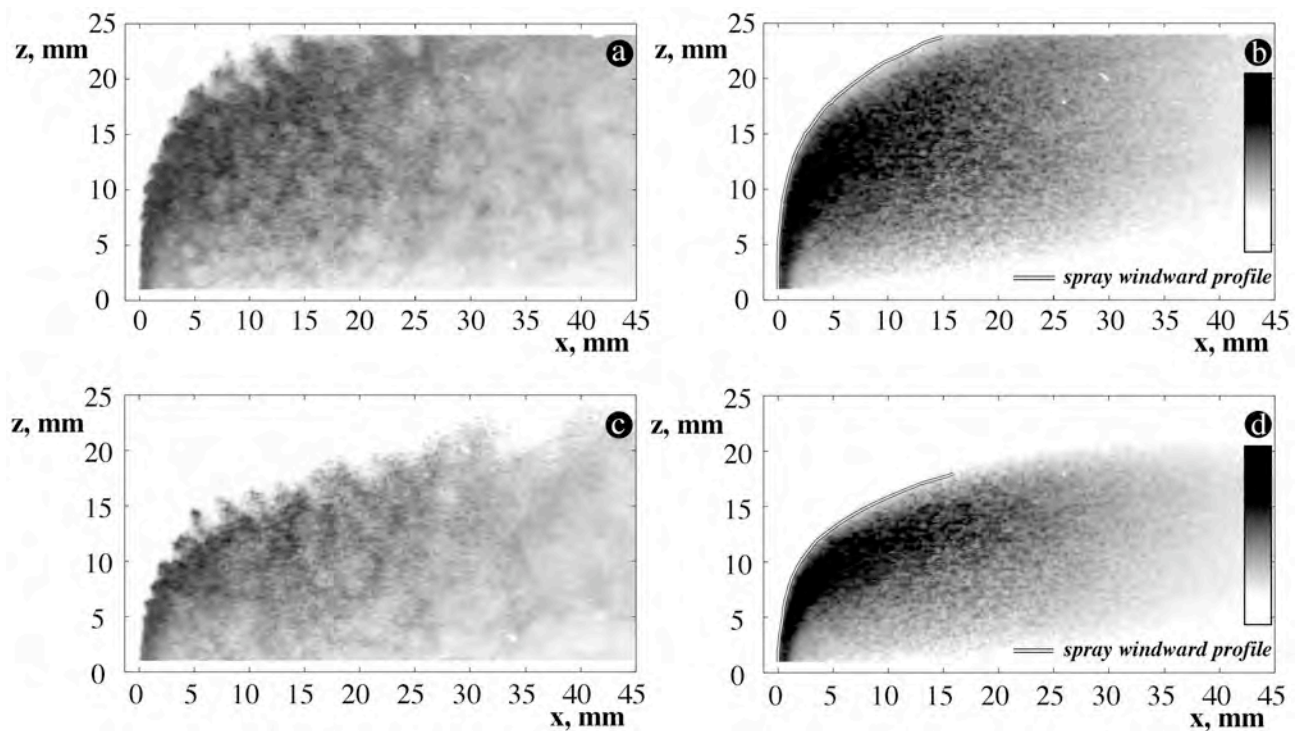


Figure 5.2. *Kerosene spray single frames (left column) and average images (right column) are reported for two conditions: air and liquid velocity respectively 21 and 36 m/s (top row) and 21 and 22 m/s (bottom row), at 1.1 MPa air pressure and 300 K air temperature. Spray windward profiles are overlaid to average images.*

Images in figures 5.2b and 5.2d are achieved by averaging on the 1000 frames ensemble at the same conditions of the single frames reported in the left column. The spray average windward profile, evaluated as the average of the 1000 upper boundaries obtained from single frames, is

superimposed on the average image. That profile is assumed as representative of the trajectory of the liquid jet.

A further statistical procedure that has been exploited consists in calculating the square average shift between single frame and average image trajectories, as a function of the transverse distance z from the nozzle outlet:

$$S(z) = \frac{1}{N} \sqrt{\sum_i [x_i(z) - x_M(z)]^2} \quad (1)$$

In Equation (1) $x_i(z)$ and $x_M(z)$ represent the position, along the axis parallel to the airflow, of the single frame and average image trajectory respectively.

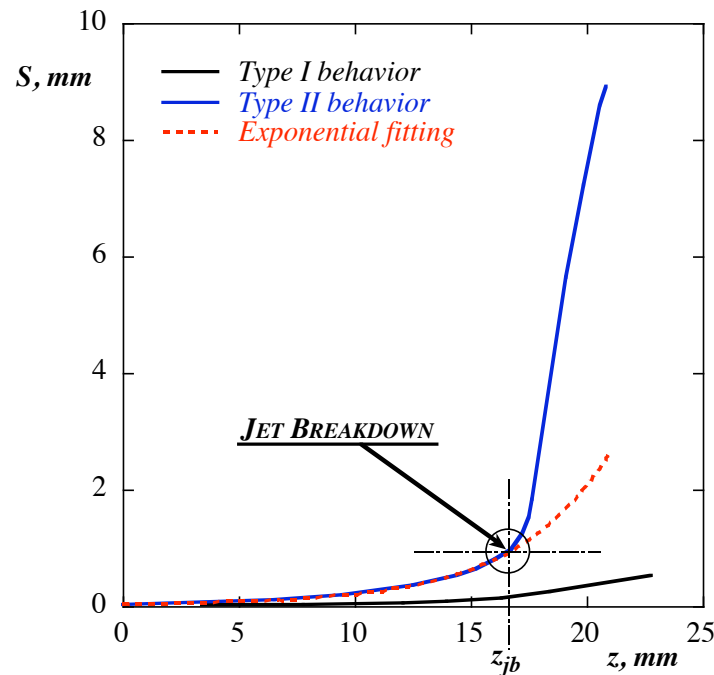


Figure 5.3. Outline of the automatic procedure for the individuation of the jet breakdown point.

As shown in figure 5.3, the S profiles versus the distance from the nozzle, z , can present two different behaviors, depending on test conditions. Initially S grows with a moderate gradual slope, afterwards it can either continue to increase gradually (*type I behavior*) or present at a certain z value a sudden increase up to values one order of magnitude higher than in the previous case (*type II behavior*). The moderate gradual increase, observed in both cases, can be interpreted as the effect

of the small jet fluctuations caused by the turbulent interaction of the two phases. The explanation of the sudden increase in the curves, observed in the second set of profiles, requires a more detailed argumentation. The increase is very steep and occurs in a very limited space interval. Typical profiles register an increase of one order of magnitude in less than 2 mm of the transverse distance z . The position of this profile knee changes with the operating conditions. This peculiar phenomenology is observed only when the kinetic content of the liquid phase is sufficiently low to prevent jet impingement onto the opposite wall of the channel without significant bending. On the basis of an analogous statistical analysis of 200 images collected for each test condition, it has been proposed that the rapid boost of S occurs only when the compact structure of the liquid column collapses in large fragments and a coherent jet no longer sustains the spray (Ragucci and Cavaliere, 2002). This loss of coherence is referred to as *jet coherence breakdown*, and it corresponds to the point after which the jet does not behave as a continuous liquid column. A speculative interpretation of the S profiles relies on the hypothesis that the liquid column underneath the visible plume of drops works such as a skeleton for the spray, governing its overall shape and preventing it from undergoing too large fluctuations due to the aerodynamic turbulence. As long as there is a liquid coherent structure opposing resistance to the drag force exerted by the airflow, the index S registers small fluctuation in the spray windward profile. After the jet breakdown point the jet loses its coherence, probably due to the rupture of the liquid column, and the airflow easily drags residual liquid structures, either liquid ligaments or drops. In the following the position of the point where the sudden increase in the S profiles can be observed, with respect to the nozzle outlet, will be indicated by means of a breakdown transverse and downstream distance, respectively referred to as x_{jb} and z_{jb} . The existence of a *jet coherence breakdown* is relevant also in the modeling of jet behavior, since the mathematical description of a jet bent by a transverse airflow is quite different from the one appropriate to describe the interaction of drops or insulated liquid fragments in the same conditions.

Relying on a more statistically relevant sampling than in a previous study (Ragucci and

Cavaliere, 2002), a fully automated procedure has been developed for the determination of the jet coherence breakdown point. This procedure is based on the experimental observation that for every test condition, up to the occurrence of the sudden increase, the behavior of $S(z)$ is regular and well represented by an exponential curve, as shown in figure 5.3. Even though the parameters of the exponential law depend on the experimental condition, it has been possible to build up an automatic routine for the determination of the best fitting exponential curve for each measurement. The routine starts considering a small initial portion of the experimental $S(z)$ profile and calculating the best fitting exponential curve, thus progressively larger values of z are included by iteration. This way to build up the best fitting exponential curve allows cutting off the points of $S(z)$ beside the breakdown locations, points that would be wrongly accounted for by a simpler overall exponential interpolation. A standard statistical index is used to individuate the point on the jet trajectory after which the gap between exponential curve and $S(z)$ becomes larger than a chosen tolerance. The coordinates x_{jb} and z_{jb} of that point are respectively the downstream and transverse distances of the jet coherence breakdown point from the injection point. The determination of the jet coherence breakdown point can also be made, in a simpler way, by using a threshold criterion applied either on the $S(z)$ curve or on its derivative. The discriminative algorithm used here allows for avoiding both the subjectivity implied in the choice of a threshold value and the possible errors introduced by the presence of noise in the single profiles. This latter problem has been verified to be even more relevant when using procedures based on the computation of numerical derivatives even when a regularization of the data is previously applied.

5.2. Morphological analysis of the spray

As already pointed out in the previous section, the analysis of images generally starts from the definition of a region of interest, to be separated from the residual part of image, referred to as background. In the case of a sprayed jet, the zone on which one would focus attention is the portion of the image where liquid fragments intercept a line of sight between the illuminating source and

the image-capturing device. The interposition of drops causes a local attenuation of the intensity of the collected light signal, essentially due to absorption and scattering phenomena. Operatively the separation between the spray region and the background is performed by assigning a threshold value to the light signal extinction, and thus cutting off all the parts of the image for which the light attenuation is weaker than the level fixed by the threshold value. The choice of the threshold value would be somewhat easier if the distribution of light extinction intensity were bimodal. Unfortunately in the case studied here, the progressive liquid atomization and droplet dispersion result in the presence of slight gradients over the image, preventing a straightforward individuation of a criterion of separation between spray and background. As matter of fact a peculiarity of the images of liquid jets in crossflow is the existence of steep gradients on the windward side of the spray and of much more progressive gradients on the leeward side. As a consequence the choice of the threshold value has little effect on the appearance of the windward spray profile, and then it did not represent a critical point for the reconstruction of the jet trajectory (Ragucci et al., 2007). Aiming to evaluate the morphological and dynamical aspects of the whole spray plume, the chance to achieve a “correct” choice of the threshold level is at the same time relevant and somehow arbitrary. Missing indeed a step transition from the spray to the background, the selection of a cut-off value has to match the requirement of how much of the spray one want to focus on. In the image analysis presented in this study it was decided to set a threshold value equal to the 50% of the maximum value of light extinction detected over a whole set of images, and so a different value was assigned to each set, in order to sweep off any accidental variation in the illumination conditions.

Beside the problem of discriminating between spray and background, another critical point is the unsteadiness of the spray plume. This means that in a set of N images, captured in sequence by keeping unchanged the operating conditions, some general aspects of the spray are common to the N events, being they different from each other. A statistical approach is interested in evaluating both the common features, which define the average behavior of the spray, and the elements that differentiate each individual occurrence of the spray from the average. In other words, chosen a

non-deterministic property detectable from each image of a statistic sample, object of this study are the mean value and the standard deviation of the property over the sample.

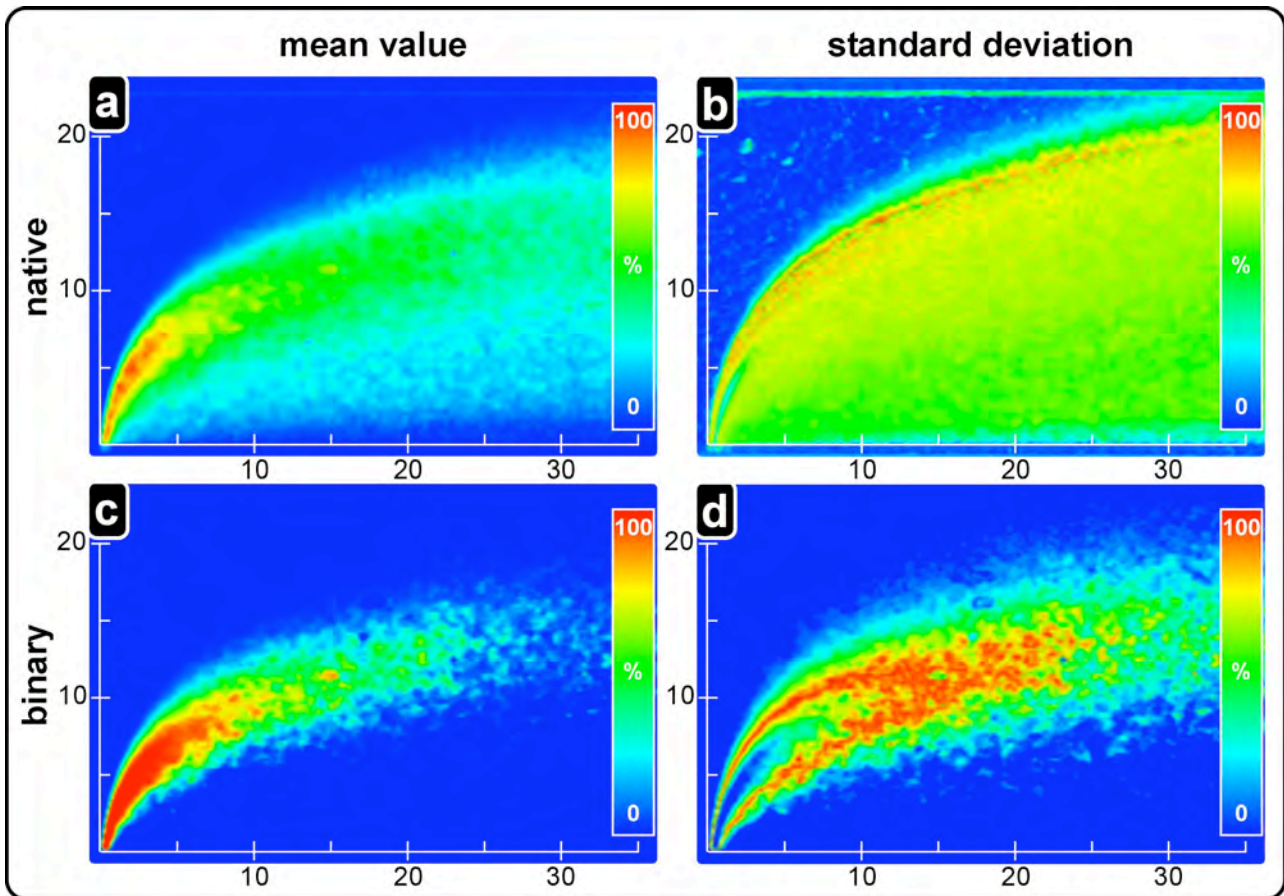


Figure 5.4. Four images representing, pixel by pixel, the mean and the standard deviation of light extinction intensity (native images) and spray occurrence (binary images). Distances are in mm. (Test case: W5F20, $V_L = 23$ m/s, $V_G = 26$ m/s)

The simplest property to be evaluated over a set of digital images is whether the spray “occupies” a certain pixel or not. This can be easily obtained by replacing the extinction signal of a pixel by a “1” if the value in that pixel overcomes the threshold value, and by a “0” if it does not. This simple non-linear operation allows creating a “binary” image starting from a “native” image; the inverse operation is obviously unfeasible. Native images are what the digital camera actually collects, and so they represent the field of intensity of light signal extinction. As a consequence for each experimental condition a set of N native images and a set of N corresponding binary images is available. Comparative analysis of the N images aims to point out features common to the whole set

and elements not systematically occurring in all the frames. This analysis passes through the evaluation of the average and standard deviation of a set of images.

Figure 5.4 reports four different images that can be generated by evaluating, pixel by pixel, the mean and the standard deviation of light extinction intensity (native images) and occurrence (binary images) of the spray. The intensity scale is normalized to the maximum. The reference case for this and all the following images is water injected at 23 m/s from a 0.5 mm plain nozzle in 2.0 MPa and 600 K air crossflow at 26 m/s. In all the investigated experimental conditions the number N of the sampling is set to 1000.

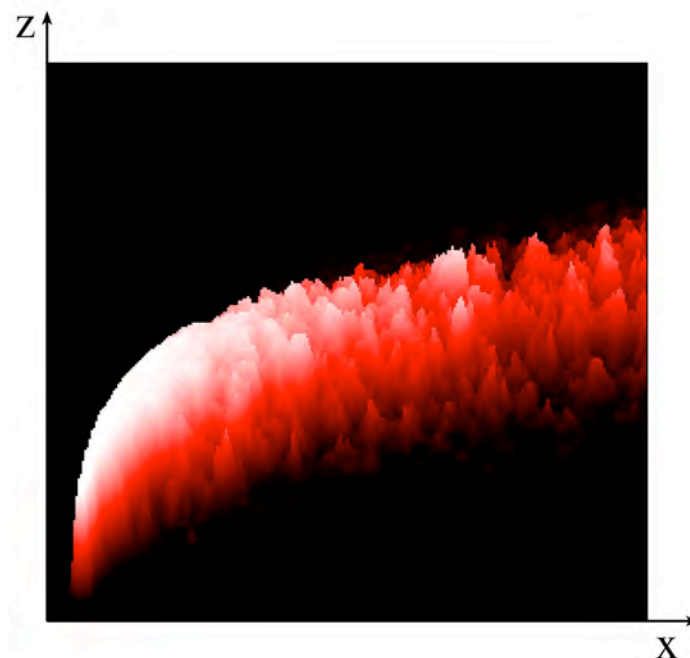


Figure 5.5. Average binary image (the same as in figure 5.4c), plotted in 3D view.

5.3. The centerline of the spray

The average native image (figure 5.4a) appears quite different from the average binary image (figure 5.4c). As point of fact each individual binary image is made up of pixel with value equal to 1, say the pixels in correspondence of which some portions of the spray interpose between the light source and the camera, and pixels with value equal to zero. In the latter case either the light path is not intercepted by the spray or light undergoes attenuation lower than the assigned minimum

threshold. As a consequence of the overlapping of the 1000 frames of a sample, each pixel will be given a value in the range between zero, in the case of light pathways never intercepted by liquid fragments, and 1000, as for those pixels systematically occupied by the spray. Since the spraying process is intrinsically unsteady, in the average binary image is a number of pixels with a value intermediate between zero and 1000. This in-between value can be thought of as the probability that the spray intercepts the line-of-sight of a certain pixel. From this point of view the average binary image can be seen as a probability map of the occurrence of the spray.

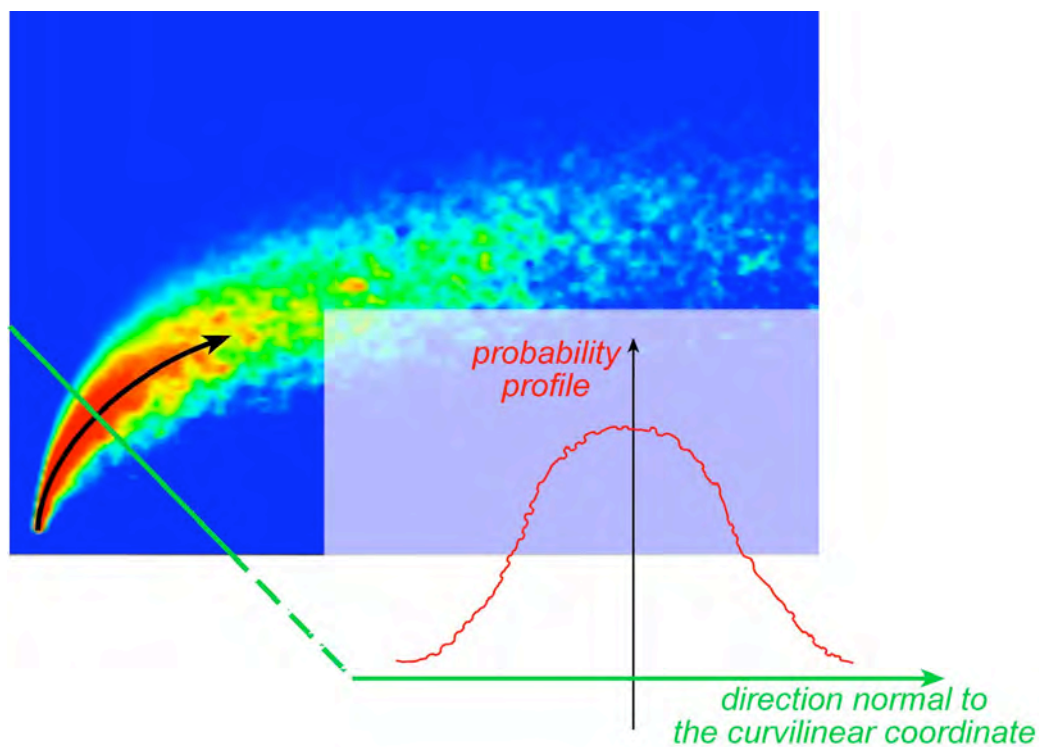


Figure 5.6. Example of probability profile at a value of curvilinear coordinate.

The typical average binary image, reported in figure 5.4c, is characterized by the zero-probability of the whole background, whereas in the spray zone the probability grows as one moves from the boundary to the centerline of the spray (see the same image as in figure 5.4c, reported in 3D view in figure 5.5). In other words it can be stated that, supposing to move along a curvilinear coordinate following the spray propagation streamline, the plane normal to each point of the coordinate identifies a probability distribution, as showed in figure 5.6. The 3D plot in figure 5.5

reveals that, despite the resort to 1000 sampled images, the probability map is even so characterized by the presence of irregularities due to residual noise. Anyway the disturbance appears less intense in the near field, where the distributions clearly show a peak close to the central zone of the spray and reduce to zero towards the boundary of the spray.

Given such a curvilinear coordinate following the spray stream, the whole average binary image can be reconstructed as a succession of probability profiles, and each of them can be replaced by a normal distribution to reduce the effect of noise. In figure 5.7 some examples of the normal distributions are plotted. The successfulness of such interpolation, mostly in the near field, is connected to the symmetry of the probability distributions. The choice of a cut-off threshold of 50% is actually meant to discard enough of the leeward spray plume, so that a good level of symmetry is achieved.

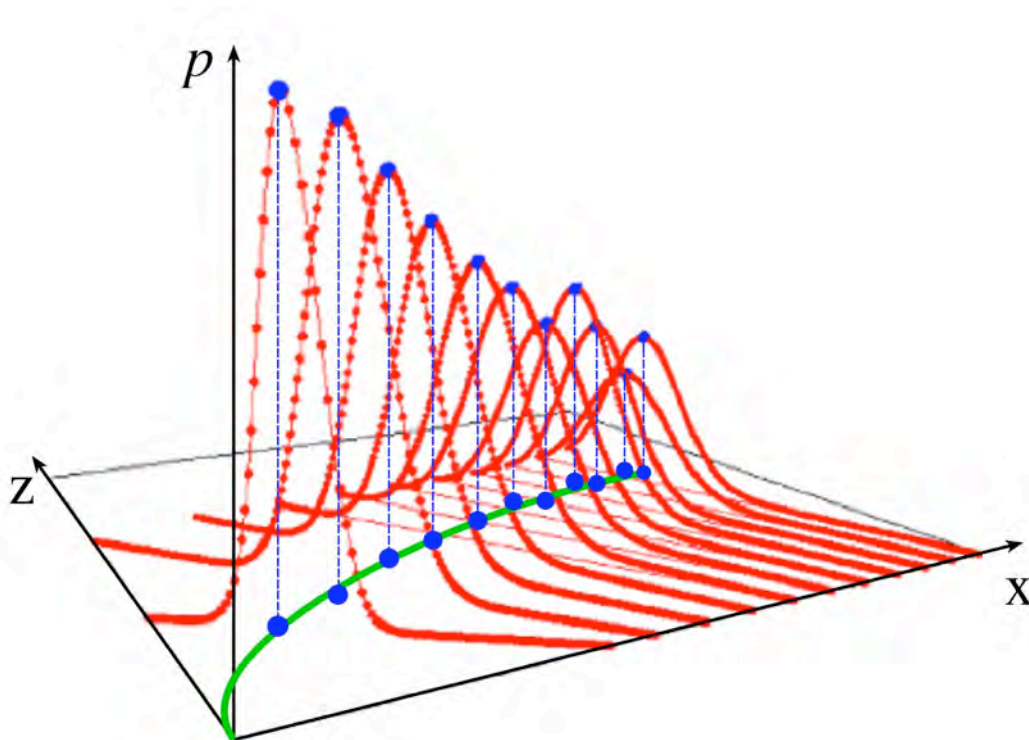


Figure 5.7. Normal distributions replacing the probability profiles for a reduced number of centerline points.

Once the experimental distributions have been replaced by interpolating normal distribution, it seems interesting to investigate the behavior of these Gaussian curves. In general the probability

profiles appear narrower close to the injection point, whereas a higher spread is clearly visible as one moves along the centerline. This fact is connected to the progressive increase of the whipping of the liquid spray, and is discussed later in this chapter. As regards the morphological aspects, figure 5.7 points out (in blue dots) the peaks of the distributions, along with their projections on the xz plane, representing the medians of the normal distributions. Quite remarkable is the fact that the medians follow a curve whose behavior recalls the already discussed jet trajectory.

The locus of the medians of all the interpolating normal distributions along the curvilinear coordinate is defined as the *centerline* of the spray. Figure 5.7 also shows that the point of the medians can be interpolated to achieve a regular, even analytical, curve. The issue of either interpolation or analytical description of the spray centerline is discussed in the chapter of the experimental results.

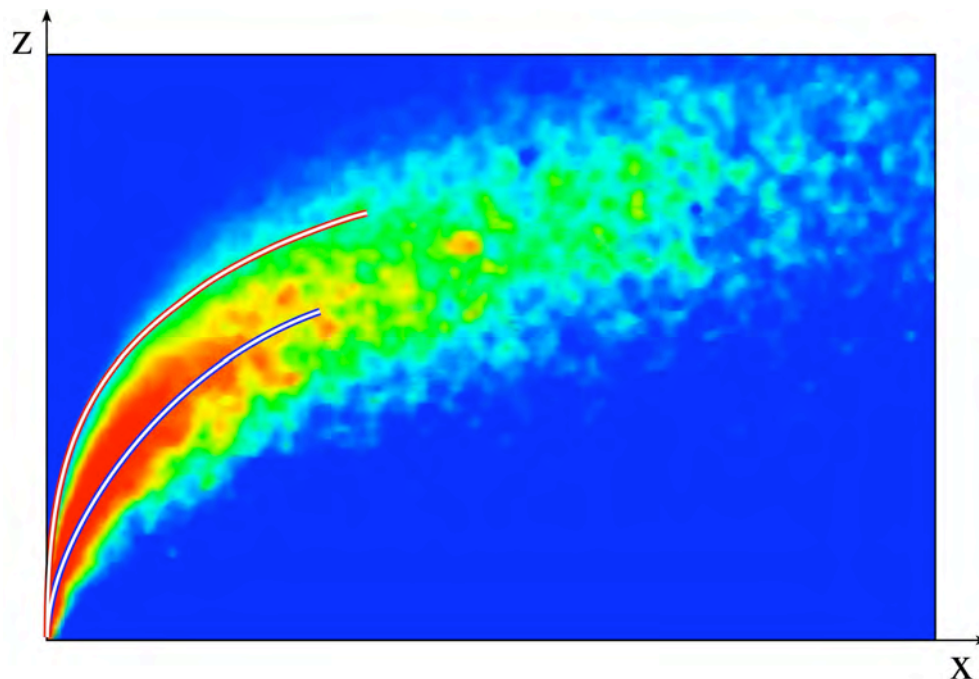


Figure 5.8. Typical average binary image. The overlapped curves are the jet trajectory (blue line) and the spray centerline (red line).

Figure 5.8 plots again a typical average binary image and overlays the spray windward profile (blue line) and the locus of the medians of the interpolating normal distributions (red line). Since the airflow drags the stripped fragments downstream and so a thin shield of droplets envelops the

liquid column, the spray windward profile corresponds to the trajectory of the liquid jet, as pointed out before. On the contrary the spray centerline provides information of placement and evolution of the core of the liquid plume.

5.4. Determination of the spray centerline

The definition of spray centerline stems from the investigation of morphological features of the plume of droplets. So far this investigation has identified the characteristic behavior of the probability map and moreover has defined a convenient approach for the analysis of the spray, based on the reconstruction of the three-dimensional probability map as a collection of two-dimensional profiles on the planes normal to the line of propagation of the spray. It is important to stress that the choice of the line of propagation, or curvilinear coordinate, affects the appearance of the probability distributions, as an effect of the modified angles at which the normal planes cut the probability map. From a conceptual point of view, the most natural choice for the curvilinear coordinate seems to be the centerline itself, suitable to describe how morphological and statistical parameters behave as the spray evolves from the injection point up to the ultimate disintegration. The operative implementation of such choice introduces some problems, since it is obvious that the determination of the centerline requires that the centerline itself is preliminary known, as the propagation line required to identify the normal planes. The stalemate can be broken by setting up an iterative procedure, which starts from an approximation of the centerline to reconstruct the probability profiles, interpolate them with normal distributions, evaluate their medians, interpolate the locus of the medians and finally achieve an improved approximation of the centerline. It has been observed that the curvilinear coordinate strongly influences the appearance of the normal distribution, but it less affects the overall look of the resulting centerline, and the discrepancies further decrease after the interpolation. Therefore the implemented iterative procedure is actually little sensitive to the tentative value, and so the liquid jet trajectory is chosen as first-step estimation of the centerline. Due to the little sensibility of the procedure, the iterative calculation rapidly

converges to the correct solution. As matter of fact it has been verified that the third-step centerline does not significantly differ from the second step.

5.5. Instability and intermittency of the spray

The evaluation of the average behavior of both native and binary images allowed for investigating the morphological features of the spray. The intrinsic unsteadiness of the spraying process has been already mentioned and is a matter of interest, since spatial and temporal non-uniformities of the air/fuel mixture are considered potentially responsible of the onset of undesired instability phenomena in the combustion process. The statistical analysis of spray fluctuations is based on the evaluation of the standard deviation of both native and binary images. An example of the resulting images is reported in figures 5.4c and 5.4d, respectively.

The variance of the native image (figure 5.4c) can be seen as a plot of the instability field of the spray, being the value associated to each pixel representative of the level of local unsteadiness of the light signal attenuation due to the interposition of liquid fragments and drops. In other words the atomization process produces a plume of traveling fragments and droplets, whose density and size are distributed, in space and time, with a highly irregular pattern. As a consequence the line-of-sight of a pixel in the spray region is occupied by a temporally variable amount of droplets, resulting in fluctuations of the light extinction signal. The intensity field plotted by the standard deviation of the native images is mainly attributable to this phenomenon, and so this image is assumed to represent the *instability* map of the spray. This image typically shows a rather uniform instability throughout the wall region covered by the spray, with a little and gradual increase of the light attenuation flickering as one moves towards the upper edge of the spray. This behavior is probably due to the presence, near to the wall housing the injector, of a fine spray (stripped from the liquid jet by the airflow), whose granulometry and spatial distribution result in a low level of fluctuation of the detected light signal. By rising up to the top edge of the spray, the presence of larger fragments, still to be further atomized, is supposed to be responsible of a worse dispersion in the gas phase, as

testified by the slightly higher flickering of the signal.

The variance of the binary image (figure 5.4d) must be attributed to a different oscillatory phenomenon, since the binarization process nearly neutralizes the fluctuations due to the irregular distribution of droplets in the channel. Unsteadiness of the binary images mainly stems from global whipping of the spray and only marginally depends on the stochastic flickering due to the local, even small, fluctuations of the light extinction signal. As a consequence it can be stated that the standard deviation of binary images depicts the whipping field, *intermittency* map, of the spray. In this map, the pixels with higher values are characterized by a higher uncertainty to find there the spray, and typically the maximum uncertainty is localized in the surroundings of the spray boundary, as reported in figure 5.4d.

Incidentally, it must be noted that figures 5.4c and 5.4d are not independent from each other. As matter of fact, due to the circumstance that each pixel can assume value either 0 or 1, the mean value μ (probability) and the standard deviation σ (uncertainty) are correlated as:

$$\sigma = \sqrt{\mu(1-\mu)} \quad (4)$$

Chapter 6. EXPERIMENTAL RESULTS

The keywords of the experimental work performed in this PhD thesis are:

- investigation of the behavior of a liquid jet sprayed in air crossflow;
- exploration of a wide range of experimental conditions, by varying nearly all the operating parameters;
- collection of shadowgraphic images of the spray, with a sampling of 1000 frames for each test condition;
- classification of the measurements in a database of 298 experimental conditions, grouped in 10 test cases;
- development of image statistical analysis procedures for elaborating raw data.

In section 6.1 the qualitative study of the spray, based on a separate set of experimental data collected in controlled conditions and with a different diagnostic configuration, is presented.

The developed statistical analysis procedures focused on the quantitative study of morphological and dynamical features of the liquid jet, whose results are presented in section 6.2, and of the whole spray plume, whose results are accounted in section 6.3.

6.1. Qualitative study of spray morphology

6.1.1. *Modified diagnostic configuration*

A qualitative description of the main phenomenological features of the spray has been already provided in chapter 2 on the basis of experimental evidence and theoretical inference collected so far in the open literature. In the experimental work performed for this PhD thesis phenomenological investigation has been carried on in parallel and separately from statistical analysis. The latter required a massive sampling and so the configuration of the digital camera with the highest acquisition rate was selected. Results presented later on statistical analysis are based on images with spatial resolution of 640x200 pixels and acquisition rate of 240 Hz. Aiming to a qualitative study of

the morphology of the spray, as it is observed by the camera, a different configuration was chosen in order to enhance the image quality. As a consequence the camera was arranged to collect 640x480 pixel images. Doubling the spatial resolution resulted in a lower acquisition rate, about 100 Hz. Moreover it was decided to further improve the magnification, by zooming on a smaller portion of the premixer, close to the injection point. The camera was also rotated by 90°, so that the observed region is 13.5x16 mm wide. The length of 13.5 mm, in the airflow direction, corresponds to about 20% of the length observed in the baseline configuration used for statistical analysis, while in the other direction the 60% of the original length was retained, thus allowing for observing about half of the width of the premixing channel. Figure 6.1 shows a typical image collected with the configuration just described, along with a magnification of the near field, where the mechanisms of inception of the atomization process are observable.

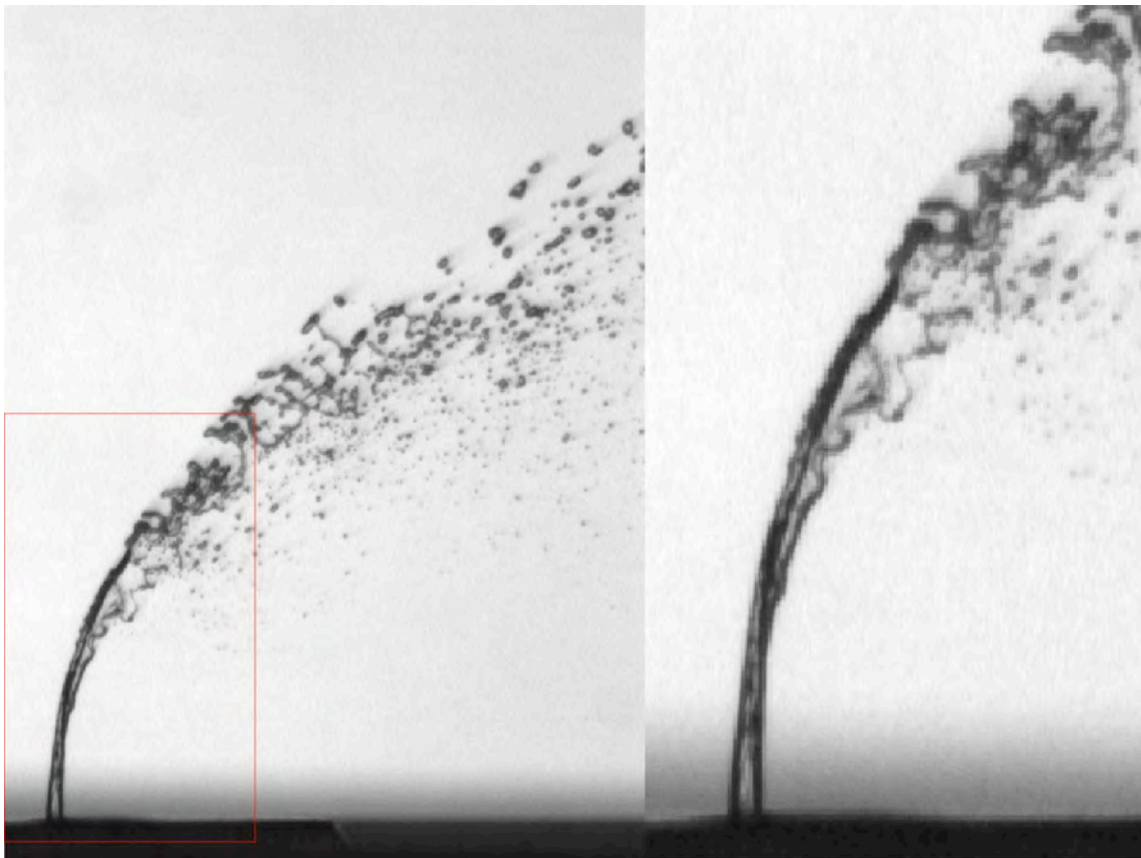


Figure 6.1. Instantaneous image of a water jet injected in a 1.0 MPa, 300 K air crossflow. ($We_{aero} = 6$; $q = 20$). The image on the right is a 2x zoom of the zone included in the red box.

Gas temperature (K)	Gas pressure (bar)	Gas density [kg/m ³]	Liquid velocity [m/s]	Gas velocity [m/s]	We_L	We_G	We_{aero}	q
300	10	11.7	29.1	23.1	3487	26	41	134
300	10	11.7	24.5	23.1	2459	26	29	95
300	10	11.7	23.1	23.1	2183	26	26	84
300	10	11.7	22.7	23.1	2121	26	25	82
300	10	11.7	21.6	23.1	1916	26	23	74
300	10	11.7	19.8	23.1	1616	26	19	62
300	10	11.7	18.4	23.1	1390	26	16	53
300	10	11.7	17.2	23.1	1219	26	14	47
300	10	11.7	15.6	23.1	995	26	12	38
300	10	11.7	14.3	23.1	844	26	10	32
300	10	11.7	12.3	23.1	618	26	7	24
300	10	11.7	11.1	23.1	505	26	6	19
300	10	11.7	9.0	23.1	333	26	4	13
300	10	11.7	5.9	23.1	145	26	2	6
300	10	11.7	3.0	23.1	37	26	1	1
300	10	11.7	24.5	30.0	2465	43	29	56
300	10	11.7	24.0	30.0	2363	43	28	54
300	10	11.7	22.6	30.0	2106	43	25	48
300	10	11.7	20.5	30.0	1727	43	20	39
300	10	11.7	19.7	30.0	1590	43	19	36
300	10	11.7	18.7	30.0	1436	43	17	33
300	10	11.7	18.3	30.0	1378	43	16	32
300	10	11.7	16.1	30.0	1068	43	13	24
300	10	11.7	15.7	30.0	1018	43	12	23
300	10	11.7	14.0	30.0	801	43	10	18
300	10	11.7	12.9	30.0	679	43	8	16
450	20	15.6	35.9	35.7	6732	103	108	63
450	20	15.6	22.0	34.5	2514	97	40	25
450	20	15.6	20.5	34.5	2195	97	35	22
450	20	15.6	11.9	34.5	733	97	12	7
450	20	15.6	8.2	34.5	349	97	6	4
450	20	15.6	10.3	33.6	558	92	9	6
600	20	11.7	35.3	29.5	8911	73	104	123
600	20	11.7	27.1	29.5	5254	73	61	72
600	20	11.7	21.0	28.6	3138	68	37	46
600	20	11.7	2.7	28.5	51	68	1	1
600	20	11.7	16.1	28.0	1847	65	22	28
600	20	11.7	12.8	28.0	1167	65	14	18
600	20	11.7	24.2	26.8	4187	60	49	70
300	20	23.4	35.7	30.0	5235	86	125	59
300	20	23.4	29.6	30.0	3606	86	86	41
300	20	23.4	23.6	30.0	2297	86	55	26
300	20	23.4	18.5	29.5	1405	84	33	16
300	20	23.4	12.9	29.5	682	84	16	8
300	16	18.7	18.6	29.5	1428	67	27	21
300	10	11.7	9.1	29.0	341	40	4	8
300	10	11.7	6.2	29.0	155	40	2	4
300	10	11.7	3.8	28.5	60	39	1	2

Table 6.1. The set of experimental conditions investigated only in the phenomenological study with a suitable diagnostic configuration.

6.1.2. Experimental conditions for phenomenological analysis

The study of qualitative morphology required the collection of a separate set of experimental

data. Aiming to improve the possibility to observe the behavior of the liquid column as it issues from the nozzle and then interacts with the crosscurrent airstream, the choice of conditions to be investigated resulted biased towards a range where weaker interplay with the airflow produces a poorer atomization. As a consequence measurements with relatively low gas and liquid velocity were collected, also in order to contain the jet penetration within the limits of the adopted diagnostic configuration. Figure 6.1 shows that, if the velocity of both phases is low, the liquid jet survives for a while without evident drop shedding.

These 49 experimental conditions are listed in table 6.1, in which air reference temperature and pressure, liquid and air velocity and dimensionless parameters are reported. It must be emphasized that these measurements were used only for qualitative phenomenological investigation, and so they miss in both statistical analysis and numerical model validation presented later on.

For this particular purpose distilled water was injected in airflow at various conditions in order to study the effect of operating parameters on jet behavior and atomization mechanisms. At gas temperature equal to 300 K data were collected mostly at gas pressure of 1.0 MPa, with only few measurements at 2.0 MPa. Two further gas temperature were investigated, 450 and 600 K, and in both cases gas pressure was kept at 2.0 MPa. Velocity range is between 5 and 35 m/s for the liquid and between 20 and 35 m/s for the gas phase.

6.1.3. *Mechanisms of atomization*

A typical instantaneous frame of the spray collected in moderate injection conditions is reproduced in figure 6.2. Here it can be observed that the liquid jet issuing from the injector initially undergoes some surface distortions due to the high level of turbulence generated inside the nozzle. It seems that at the very outlet section the cross-section of the jet is only roughly circular. After few millimeters small waves become obvious on the windward profile of the jet. Presumably below this height they are under the resolution limit of the camera. These waves clearly develop along the jet and therefore their amplitude grows. The elongated waves on the windward profile are

progressively deflected by the air drag. In the meanwhile the visible width of the cross-section of the jet shrinks to less than 50% of the initial thickness. Since no mass removal is observable at this stage, it is probable that this width reduction is connected with a flattening of the jet cross-section, although it is impossible, from this view, to understand the actual shape of the flattened jet. This shape should be however more complicated than the expected elliptical or lenticular shapes, as it can be inferred by the fact that the air is able to blow into the liquid column forming a bag. In these operating conditions liquid disruption seems to be mostly attributable to bag explosion, whose further effect seems to be an enhancement of column distortion. After a minimum width reached just before the formation of the bag, progressive loss of continuity and coherence of the liquid jet occurs, as can be observed by applying to the image some simple image elaboration tools available in Adobe Photoshop™ 7.0. The image is firstly sharpened in order to aid edge detection, and then the spray contour is traced. These two steps are reported as the first two frames of figure 6.3.

The frame *a* of figure 6.3 is obtained by masking the spray image with a sharpening operator (amount: 500%; radius: 4.0 pixels; no threshold). It shows better defined contours, which can be extracted by “trace contour” routine (threshold: 50%), as reported in figure 6.3*b*. The low level of atomization allows detecting most of the individual droplets removed from the jet. In addition the large fragments resulting from the final breakup of the liquid jet are clearly visible in the upper region of the image. Figure 6.3*c* is obtained from the previous frame by filling up (in black color) the area delimited by the single continuous boundary connected to the injection point. Even if the jet undergoes severe distortion, air entrainment and mass removal, in the reported instantaneous picture it holds continuous for a while after the point of minimum width. The inset of figure 6.3*c* shows a magnified portion of the jet, from first bag onset up to the interruption of the detected continuity of the liquid column. It emphasizes the progressive increase of the level of air entrainment, the growth of surface waves on the windward profile (deformed until some small vortexes appear), and the presence of ligaments on the leeward side of the jet, generate by bag burst.

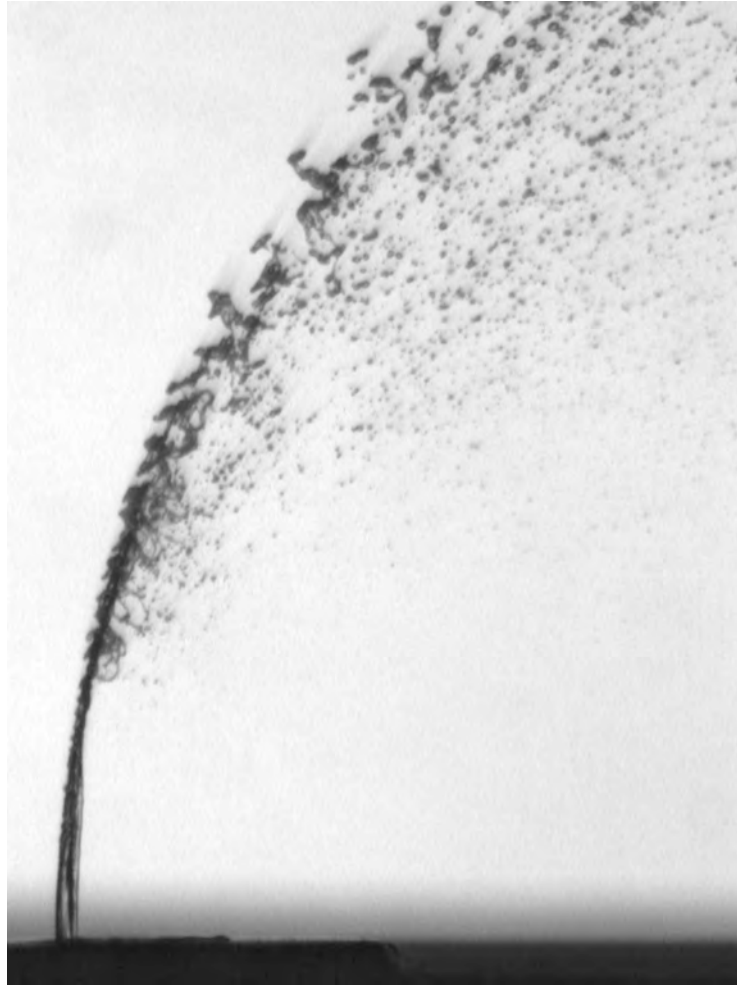


Figure 6.2. Instantaneous image of a water jet injected in a 1.0 MPa, 300 K air crossflow. ($We_{aero} = 16$; $q = 54$).

The individuation of a continuously connected surface, as pointed out in figure 6.3c, could suggest a heuristic method to evaluate the intact length of the jet. Several procedures similar to the suggested one have been found in literature, but in this study it was observed that this method could give reasonable results only when the level of atomization is low. A more intense cloud of drop envelops the jet and makes it hard, where not impossible, to detect the actual contour of the underlying jet. In the following section results on a rigorous statistical procedure for jet breakdown detection will be presented.

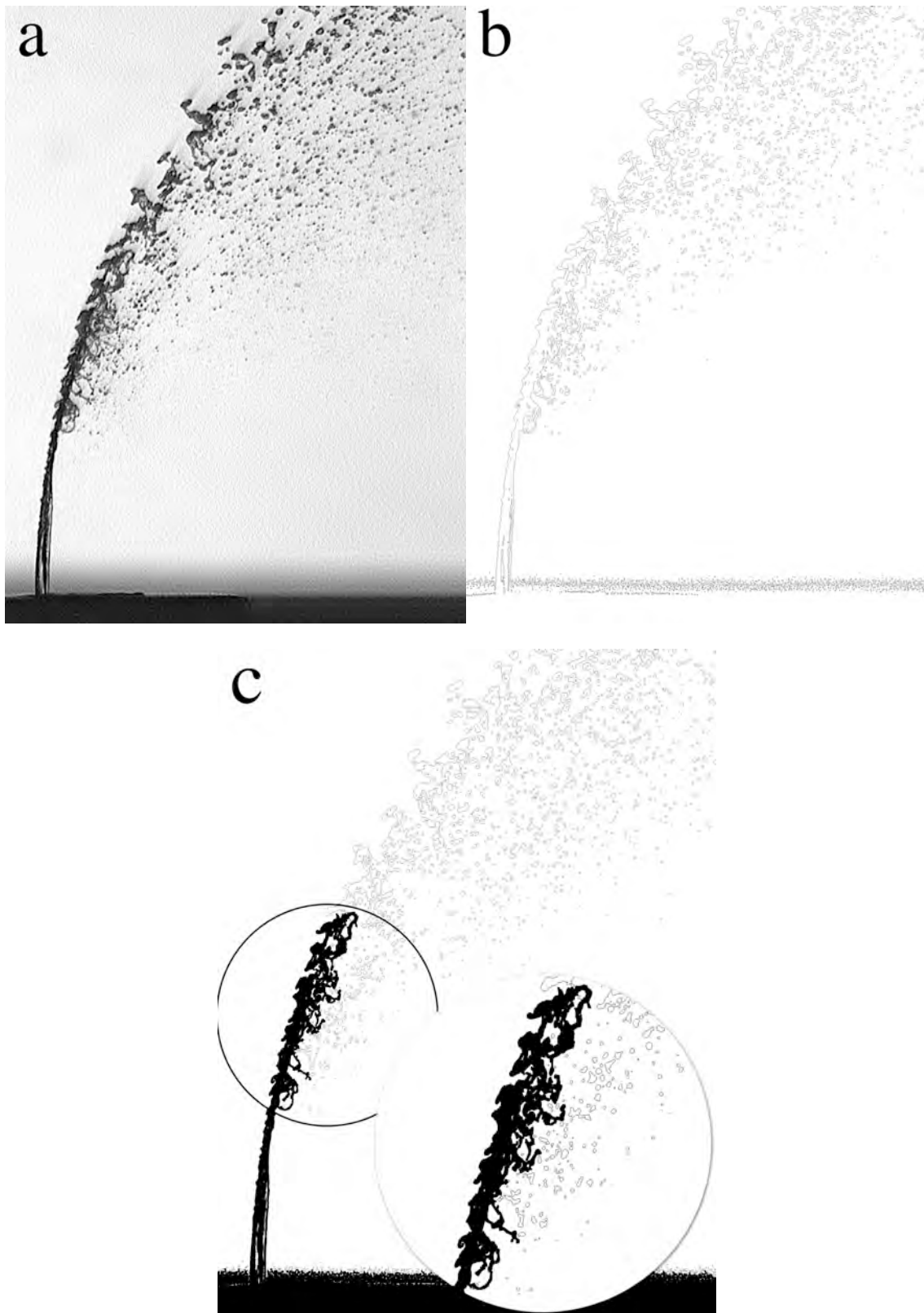


Figure 6.3. Manipulation of the image in figure 6.2. Frame a is the outcome of the operator “sharpen unmask”, while frame b results from “trace contour”. Frame c is obtained from frame b by filling the single contour connected to the injection point. The inset is a zoom of the primary breakup region.

6.1.4. Dependence on dimensionless parameters

Figure 6.4 presents instantaneous images of four experimental conditions characterized by increasing value of aerodynamic Weber number.

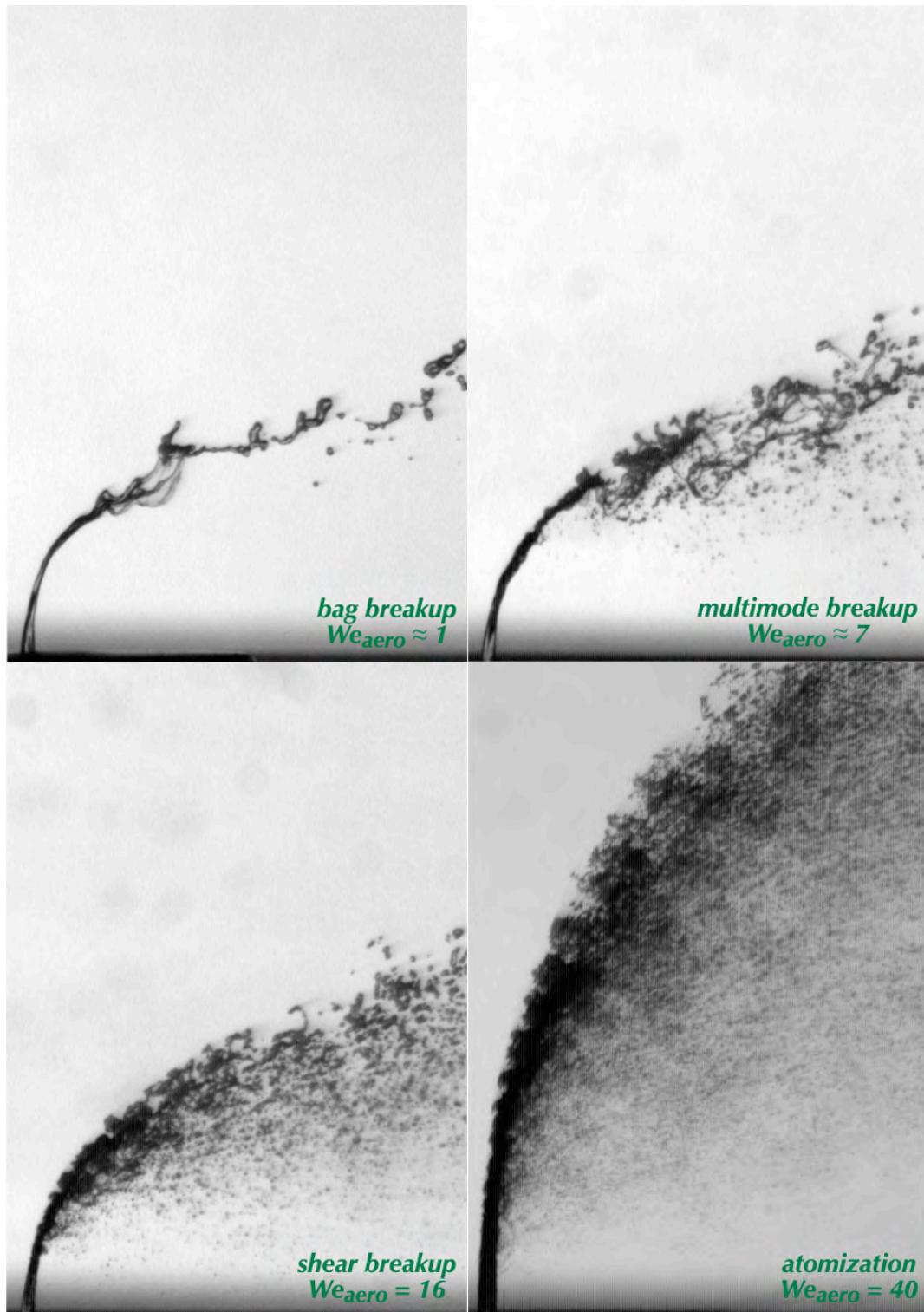


Figure 6.4. Synopsis of the atomization mechanisms. Increasing the aerodynamic Weber number pushes the jet from bag breakup towards shear breakup and atomization regime.

The top-left image in figure 6.4 refers to a spraying condition with $We_{aero} = 1$. In this regime the development of surface instabilities is quite slow, therefore there is time for the formation of a large bag, as clearly observable in the image. Capillary pressure plays a relevant role, and so the breakup produces big fragments and few satellite droplets. The second frame in figure 6.4 reports the injection of water at $We_{aero} = 7$. This condition has been selected since it presents similar penetration with respect to the previous frame, and also analogous bag formation. The difference is the higher irregularity of the liquid surface, showing more waves with more elongated shape, and the subsequent presence of a larger number of smaller droplet removed from the liquid jet. This regime is characterized by the coexistence of both bag and shear breakup mode, and so it is referred to as multimode breakup. In the following frame, at bottom-left of figure 6.4, the formation of bags no longer occurs, and so the jet disrupts by only shear breakup mechanism, characterized by the stripping of drops from the corrugated surface of the jet. At higher Weber numbers, roughly above 30, full atomization regime is observed. In these conditions the development of small amplitude waves produces a fine aerosol of droplets enveloping the liquid column and promptly stripped away in the wake of the jet.

6.2. Momentum breakdown and trajectory of the liquid jet

6.2.1. Tests on cold sprays

In chapter 5 the definition of the jet momentum coherence breakdown has been introduced, along with an automatic procedure for the operative determination of occurrence and location of the breakdown point. In a first stage of this investigation statistical analysis was preliminarily performed on sprays injected in airflow at room temperature. The statistical analysis tools presented in the previous chapter were applied to a set of 83 measurements at room temperature. The results are reported in figures 6.5a and 6.5b for the transverse and the downstream coordinate, respectively. The former graph, in log-log scale, shows that if data concerning z_{jb} are plotted as a function of the liquid-to-air momentum ratio q , experimental points align quite well and so in the explored field of

operating conditions the liquid-streamwise penetration of the liquid jet can be predicted by the following empirical correlation:

$$\frac{z_{jb}}{D} = 5.068 q^{0.476} \quad (1)$$

The agreement of this equation with experimental data was evaluated by means of the Pearson's correlation coefficient R , which resulted in a value of 0.943, indicating a good capability of prediction. As regards the gas-streamwise coordinate, it can be observed from figure 6.5b that if the values of x_{jb} for kerosene and water jets, normalized to the nozzle outlet size D , are plotted against the aerodynamic Weber number We_{aero} , the points lay along a straight line. The following expression for this line was determined by using a best fitting algorithm:

$$\frac{x_{jb}}{D} = 3.745 We_{aero}^{0.366} \quad (2)$$

Equation 2 well fits experimental data, being the Pearson's correlation coefficient R equal to 0.951.

Wu et al. (1997) suggested that z_{jb} is a function of the square root of the q number. A similar dependence is here proposed, but on the basis of the present data it is not possible to account for the effect of the densities of the two phases, since air pressure and temperature were kept constant and the two used liquids do not differ much in density. Since in most empirical correlations proposed in the literature the air-to-liquid density ratio is accounted for without exploring extensive ranges of these properties, further measurements seem to be necessary to clarify the influence air and liquid density have on jet behavior and breakdown.

As regards the dimensionless downstream distance x_{jb}/D , Wu et al. (1997) supposed a constant value of 8.06. Measurements collected in the present work show a dependence on the dynamic-to-capillary pressure ratio. Differently from the breakdown transverse distance, the value of x_{jb} is then sensitive to the atomization process. Changing the injected liquid does not affect the cross-stream

penetration of the jet, but the higher the surface tension the weaker is the expected bending. The divergences from the Wu et al. seem to be attributable to the different atomization level. At the air pressure used in the experiments reported by Wu et al. (1997) (0.14 MPa) even liquids with surface tension as low as kerosene seemingly do not have intense mass removal, so that it is possible to suppose that both the influence of surface tension on jet dynamics and the variability of x_{jb} become evident only by increasing the gas density level and thus the atomization intensity. Finally, even though the basic definition of column fracture point is analogous, criteria adopted by Wu et al. to individuate that point are not the same as criteria proposed in this study to define the automatic procedure for the search of jet coherence breakdown point.

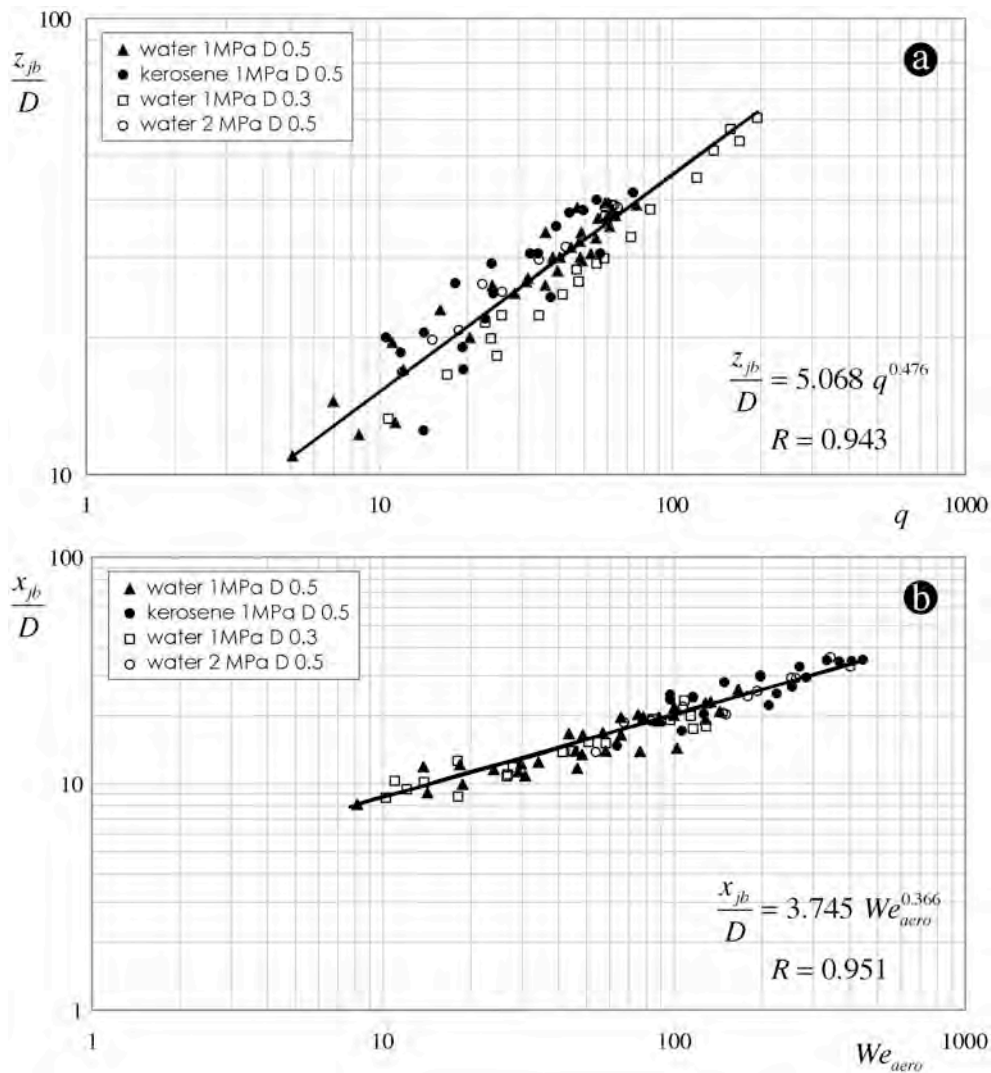


Figure 6.5. Jet breakdown transverse (a) and downstream (b) distance.

Both equations. 1 and 2 clearly give no finite value as the crossflow velocity decreases to zero. It is then obvious that this correlation is useful only for injection in crossflow, and moreover it has not been validated for airflow velocity values outside the range 20-55 m/s, since this is roughly the field of interest in the framework of LPP gas turbines. To propose a correlation valid for injection in both crossflowing and still gas has not been attempted before and is out of the scope of this thesis.

6.2.2. Test on sprays injected in hot airflow

This subsection presents the results obtained from about 82 test conditions, explored by varying liquid and air velocity from 10 up to 60 m/s approximately, using two liquids, Jet A-1 fuel and distilled water, at a reference pressure of 2.0 MPa and temperature of 600 K. These conditions closely resemble typical conditions of real gas turbine operation. The two atomizers used for injecting liquid only differ by outlet diameter (300 and 500 μm), being the same both the aspect ratio L/D of the injection section, equal to 4, and the 45° taper connecting the adduction and injection sections.

The statistical procedure, illustrated in the previous section, for determining the coordinates of breakdown position has been applied to the 82 image sets. In 7 cases it was not possible to detect a reliable value of the breakdown coordinates because the jet impinges on the opposed wall with an almost rectilinear trajectory and the fluctuations of the trajectories, in the test section, do not reveal any evidence of a jet breakdown. The average trajectories for each one of the remaining 75 cases have been normalized to the relative x_{jb} and z_{jb} values. The resulting trajectories are reported in figure 6.6a. It is evident from the figure that all normalized trajectory are very similar. As matter of fact the maximum standard deviation from the average trajectory (reported as a thick line in figure) is 3.77%. A best fitting procedure allowed verifying that the average trajectory can be very well interpolated by a power law curve with an exponent of 0.367. The comparison between the average trajectory and the power law curve is reported in figure 6.6b, along with the estimates of standard deviations of single trajectories from the average one.

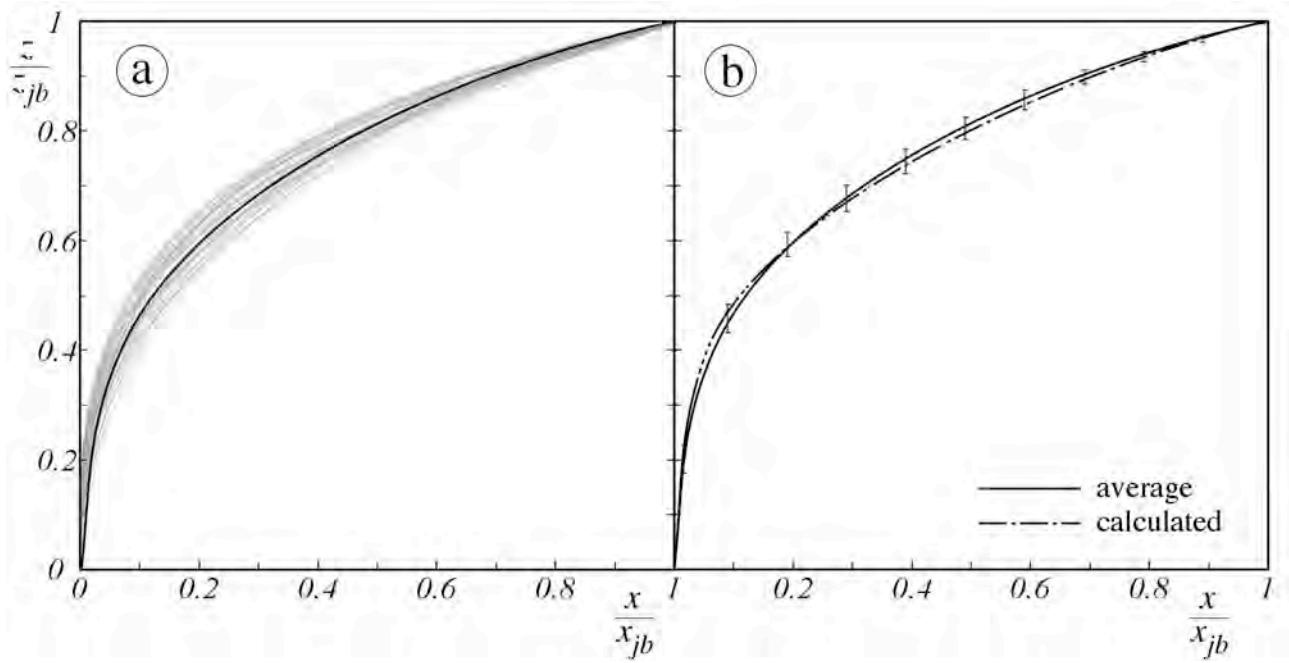


Figure 6.6 a) Normalized jet trajectories for the test cases relative to the whole set of test conditions.
 b) Comparison between average and calculated trajectory. Error bars account for the root mean square error of the average normalized trajectory.

The exponent of the power law found for the present cases is the same value found, following an analogous procedure, for the tests made at ambient temperature and reported in previous section.

The equation of the normalized trajectory takes the form:

$$\frac{z}{z_{jb}} = \left(\frac{x}{x_{jb}} \right)^{0.367} \quad (3)$$

It is thus possible to state that the equation (3) holds true in high temperature conditions.

The second step was the determination of a correlation between the jet breakdown coordinates and the test conditions to which they refer. The correlations found in this case are:

$$\frac{x_{jb}}{D} = 5.30 q^{-0.096} We_{aero}^{0.383} \quad (4)$$

$$\frac{z_{jb}}{D} = 4.12 q^{0.404} We_{aero}^{0.129} \quad (5)$$

This empirical model is similar to the one presented in previous section for sprays in cold crossflow. Again the gas-streamwise coordinate x_{jb} mostly depends on We_{aero} even though a minor influence on the liquid-to-air momentum ratio q was found. The dependence on q of z_{jb} is a little weaker than in equation (1), with an additional effect of the aerodynamic Weber number.

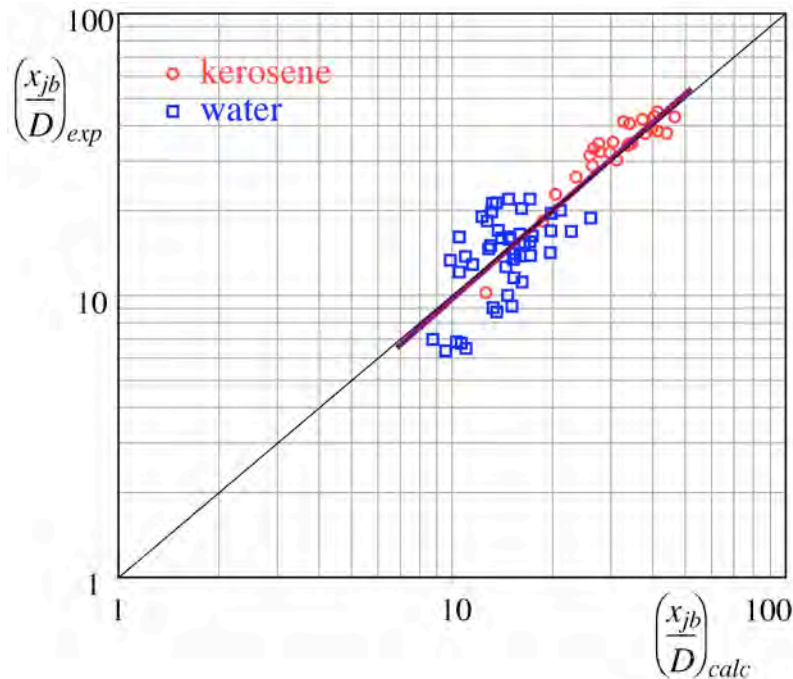


Figure 6.7. Comparison of experimentally evaluated and calculated values of x_{jb} for injection in hot air crossflow.

Figures 6.7 and 6.8 report the comparisons of the experimentally determined values of the breakdown point coordinates x_{jb} and z_{jb} with those computed by using equations (4) and (5). The data are normalized with respect to the nozzle outlet diameter, as it is quite common in the literature. In both cases the interpolating straight line, evaluated by means of least square method, is considerably close to the bisecting line. This fact couples with the relatively high values of the Pearson's correlation coefficient, which is 0.934 for equation (4) and 0.950 for equation (5), resulting in a satisfying agreement of the proposed correlations with experiments. In particular the correlation coefficient for x_{jb} is slightly worse, even though the wider scattering for water points in figure 6.8 is only apparent, due to the logarithmic scale. Relying on the substantial symmetry of

experimental data around the bisecting line, it can be said that the less accurate prediction of x_{jb} is probably attributable to the fact that the breakdown usually occurs when the slope of the jet trajectory is small, and so the experimental evaluation of x_{jb} is more sensitive than z_{jb} to possible experimental noise.

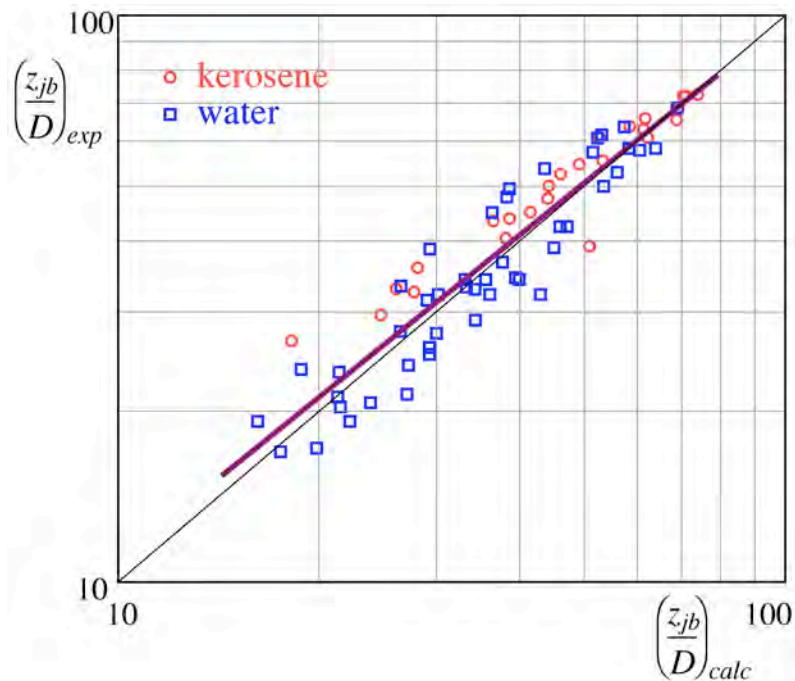


Figure 6.8. Comparison of experimentally evaluated and calculated values of z_{jb} for injection in hot air crossflow.

6.2.3. Empirical model for liquid jets in crossflow

The proposed correlations (4) and (5) do not significantly differ from equations (1) and (2) previously obtained from measurements in isothermal conditions. This suggests the chance to validate equations (4) and (5) against the whole available database of experimental conditions. This database consists of the data presented in the two previous subsections, plus a number of conditions not included in the measurements presented so far. The overall amount of 189 experimental points was compared with the calculations obtained using equations (4) and (5), as reported in figures 6.9 and 6.10 for x_{jb} and z_{jb} , respectively.

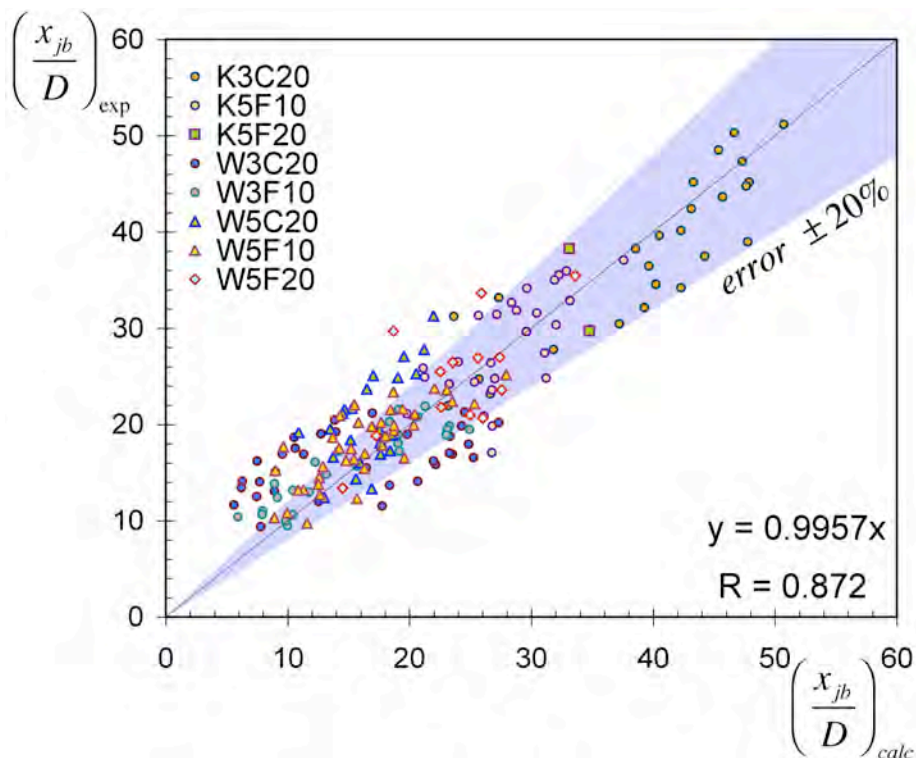


Figure 6.9. Comparison of experimentally evaluated and calculated values of x_{jb} for all the 189 available conditions. Points falling into the blue zone have less than 20% error.

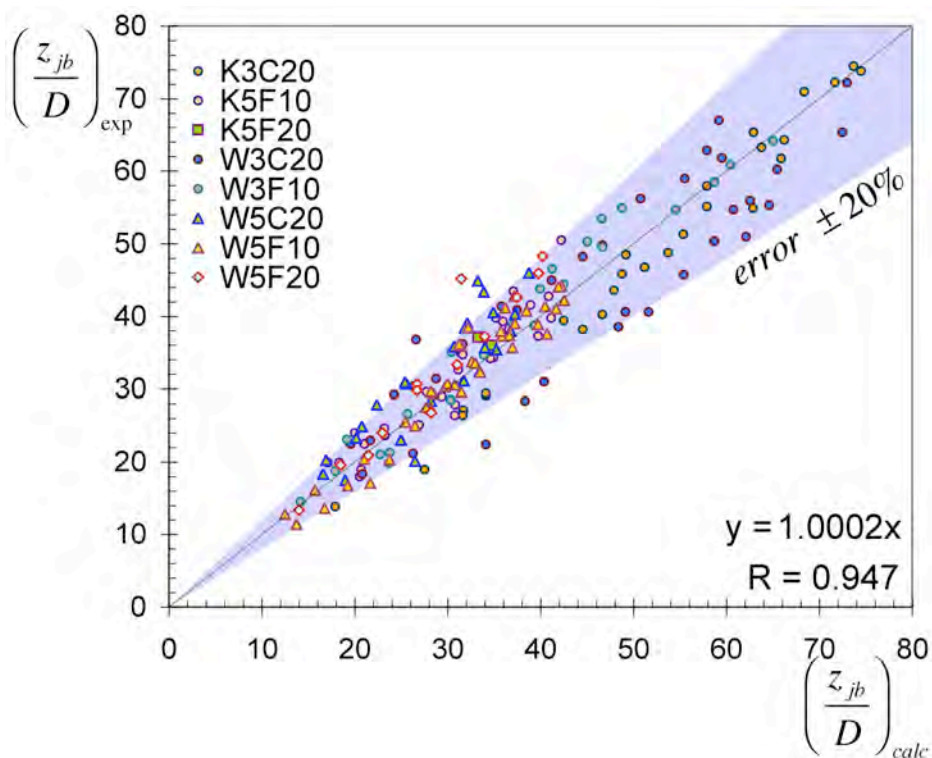


Figure 6.10. Comparison of experimentally evaluated and calculated values of z_{jb} for all the 189 available conditions. Points falling into the blue zone have less than 20% error.

In figures 6.9 and 6.10 the linear correlation coefficient R is reported together with the equation $y(x)$ of the interpolating straight-line. Both the straight-lines are close to the bisecting line, indicating a good distribution of the error around the expected value. The correlation coefficient is excellent ($R = 0.947$) for the liquid-streamwise coordinate z_{jb} , giving an idea of the maximum penetration of the jet in the premixing channel, whereas worse agreement with experimental data results from the model for x_{jb} ($R = 0.872$). The plot in figure 6.9 shows that the largest error is in the zone of little x_{jb} , where the empirical model underestimates the displacement of the jet breakdown point in the gas-streamwise direction.

By substituting Equations (4) and (5) in the normalized trajectory equation (3), the dependence of the jet trajectory can be expressed as a function of the operating parameters:

$$\frac{z}{D} = 2.23 q^{0.44} We_{aero}^{-0.012} \left(\frac{x}{D} \right)^{0.367} \quad (6)$$

In a second stage it was also taken in account the possible effect of the increase of air viscosity, that nearly doubles passing from 300 K to 600 K. It could be hypothesized that an higher air viscosity increases the drag forces and intensifies the jet bending. The correlations for the jet breakdown coordinates found by taking into account the air viscosity variation are:

$$\frac{x_{jb}}{D} = 4.25 q^{-0.095} We_{aero}^{0.382} \left(\frac{\mu}{\mu_{air, 300K}} \right)^{0.008} \quad (7)$$

$$\frac{z_{jb}}{D} = 4.186 q^{0.387} We_{aero}^{0.126} \left(\frac{\mu}{\mu_{air, 300K}} \right)^{0.036} \quad (8)$$

These correlations were derived using the whole data set of measurements taken both at low and high temperature to put in evidence the change in the viscosity. Pearson coefficient for these two correlation resulted to be nearly equal to those obtained for Equations (4) and (5). It has to be noticed that the effect of the variation of the air viscosity on the breakdown coordinate in windward

direction (x_{jb}) are quite negligible. On the other hand a more sensitive effect on the axial coordinate (z_{jb}) can be observed. By substituting equations (7) and (8) in the normalized trajectory equation (1), the dependence of the jet trajectory can be expressed as:

$$\frac{z}{D} = 2.46 q^{0.421} We_{aero}^{-0.015} \left(\frac{\mu}{\mu_{air, 300K}} \right)^{0.033} \left(\frac{x}{D} \right)^{0.367} \quad (9)$$

6.3. Morphology and fluctuations of the spray

6.3.1. Angle of spray

The concept of angle of spray was introduced in the framework of liquid injected in quiescent or co-flowing air. It is meant as a measure of the dispersion of the liquid in the gas phase. In the case of liquid injected in crossflowing airstream, the bending of the spray due to the airflow makes it hard to define a parameter analogous to the spray angle. The definition proposed in this study is based on the above-introduced concept of centerline. By assuming the centerline as corresponding to the injection axis of a jet in still air, the profile of the distance of the jet trajectory from the centerline is calculated and the average value of the slope of this profile is defined as spray angle. Obviously the same result is achieved by evaluating, for each point P of the centerline, the average difference between the angle α_c of the centerline, with respect to the x-axis parallel to the airflow, and the angle α_T of the jet trajectory at the point Q intercepted by the normal to the centerline in P (see figure 6.11).

The spray trajectory can be well described by a power law curve, as already pointed out in previous section. Analogously it has been seen that also the spray centerline can be replaced by a curve $z = k \cdot x^\beta$, being the parameters k and β evaluated by best-fit criterion. The availability of analytical expressions for trajectory and centerline simplifies the spray angle calculation.

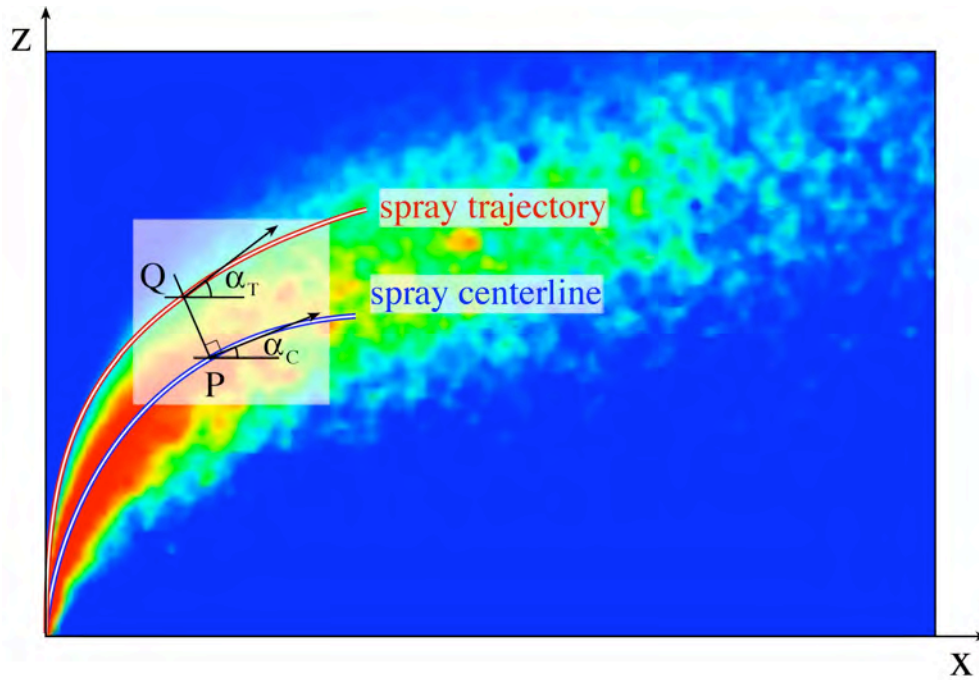


Figure 6.11. Definition of the spray angle.

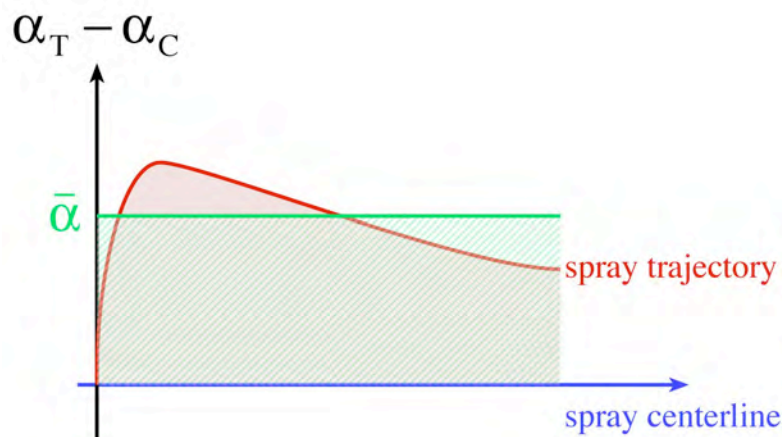


Figure 6.12. Typical profile of the spray angle along the curvilinear coordinate.

The behavior depicted by the red line in figure 6.12 appeared to be common to all cases. Actually both the mean and the maximum value of the spray angle were evaluated. As regards the maximum of the red curve, it resulted to be quite sensitive to the experimental noise, while the data obtained for the average spray angles are presented in figure 6.13, plotted against the liquid Weber number, defined as $We_L = \rho_L V_L^2 D / \sigma$, which in the performed experiments was varied between about 10^3 and 10^5 . The values of spray angle range roughly from 5° and 50° . Although the points

are quite scattered, the average spray angle shows an unmistakable trend to grow up as We_L increases. This seems to indicate that the achievement of a good level of dispersion of the liquid, at least as concerns the z axis, mainly depends on the capacity to provide enough kinetic energy to the liquid, whereas the gas kinetic energy should be suitable to assure correct placing of the dispersed phase within the premixing duct.

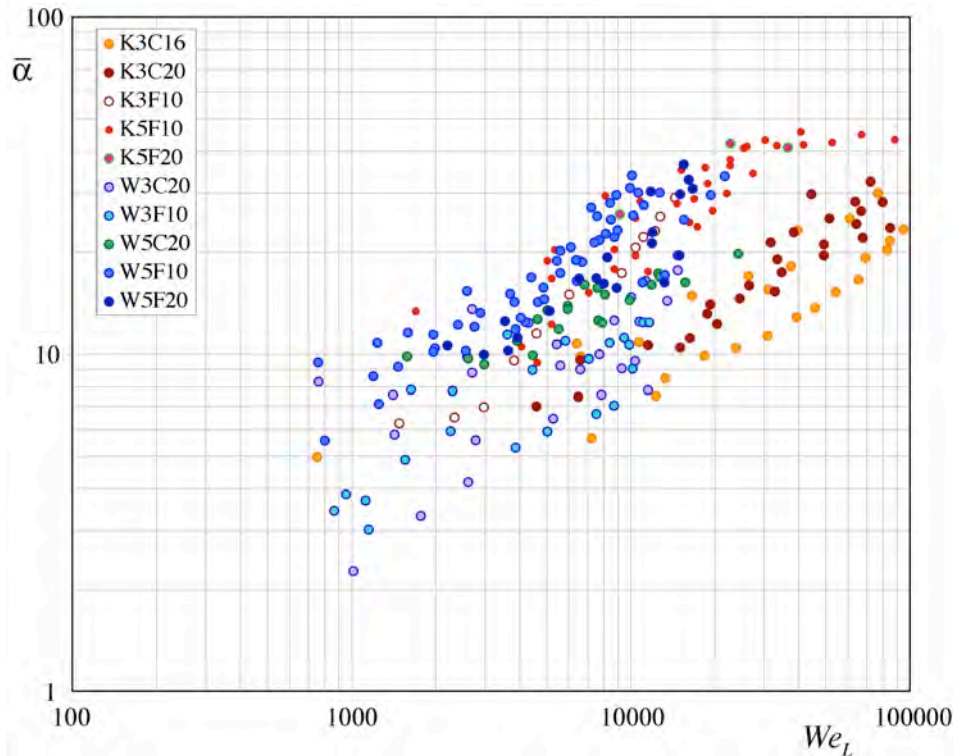


Figure 6.13. Dependence of the spray angle, in degrees, on We_L .

Both the wide dispersion of points on the plot and the behavior of the single groups of data plotted in figure 6.13 induced to hypothesize that the spray angle also depends on other parameters. An attempt to infer a multiple correlation is not easy, due to the data scattering indeed, anyway it has been observed that the data well scale with the orifice diameter. As a consequence the liquid Weber number and the orifice diameter (divided by a reference value $D_0 = 0.5$ mm to keep it dimensionless) have been chosen as independent variables to perform a non-linear regression of the spray angle data. The resulting best fitting correlation is:

$$\bar{\alpha} = 0.538 \left(\frac{D}{D_0} \right)^{1.358} We_L^{0.405} \quad (10)$$

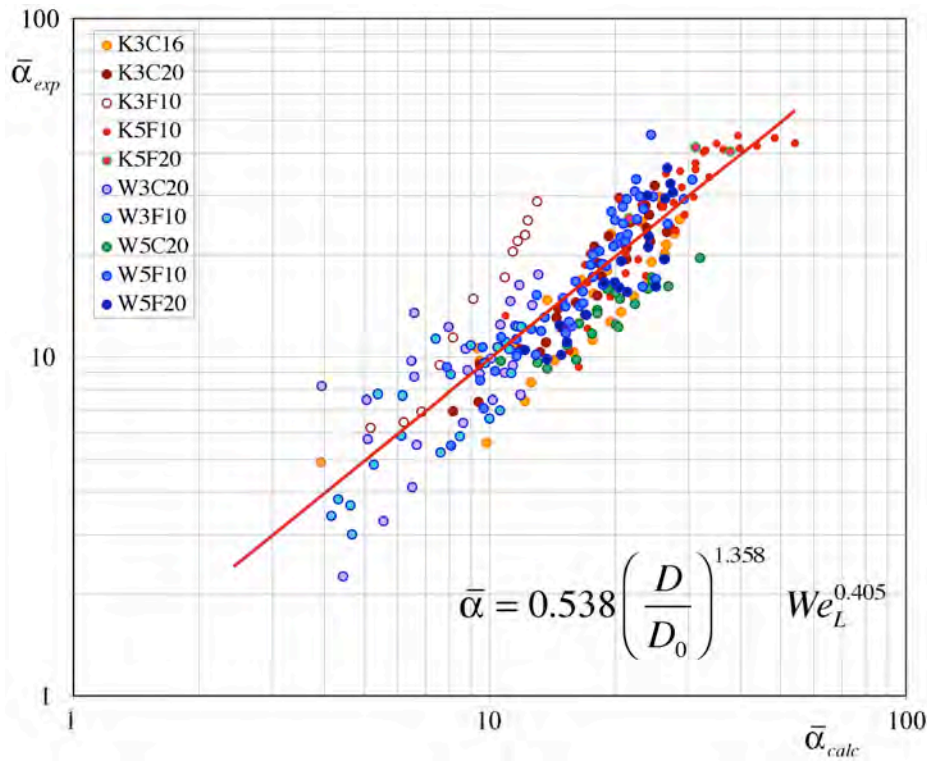


Figure 6.14. Dependence of the spray angle on liquid Weber number and dimensionless orifice diameter.

Figure 6.14 compares experimental (in ordinate) and calculated values (in abscissa) of the spray angle. The closer the points are to the red bisecting line, the better is the prediction. The correlation coefficient for equation (10) was assessed as 0.861. Equation (10) does not provide any effect of the gas kinetic energy on the spray angle. This hypothesis was tested by introducing a third independent variable, the gas Weber number $We_G = \rho_G V_G^2 D / \sigma$. The dependence on We_L and the orifice diameter being kept frozen, a further non-linear regression was performed and the resulting best fitting correlation

$$\bar{\alpha} = 1.05 \left(\frac{D}{D_0} \right)^{1.358} We_L^{0.405} We_G^{-0.123} \quad (11)$$

showed an improvement in the prediction ability, since the correlation coefficient rose to 0.882.

Anyway the effect of gas Weber number appears to be less relevant than We_L and injection diameter, and this consideration holds even if the non-linear regression is performed on the three parameters simultaneously:

$$\bar{\alpha} = 0.433 \left(\frac{D}{D_0} \right)^{1.358} We_L^{0.588} We_G^{-0.289} \quad (12)$$

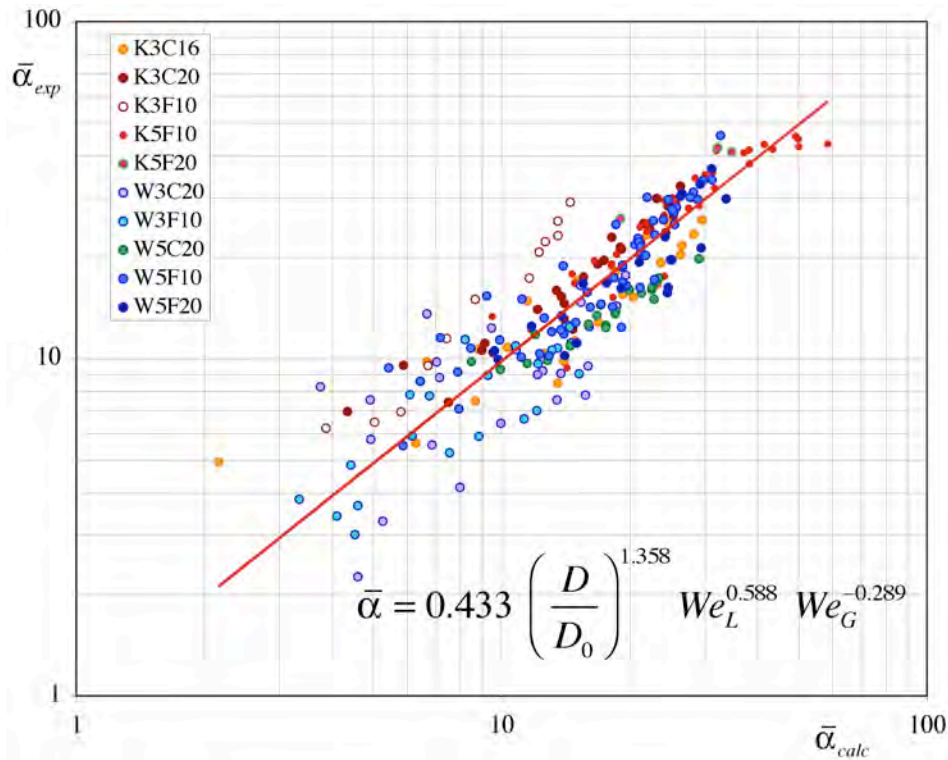


Figure 6.15. Dependence of the spray angle on both liquid and gas Weber number and dimensionless orifice diameter.

In this last case a little increase of the We_G exponent was observed, indicating that equation (11) probably underestimated the effect of gas momentum. On the other hand the parallel increase of the exponent of liquid Weber number indicates that equation (11) well predicts the dependence on the capillary pressure σ/D , being in both equations (11) and (12) expressed by an exponent of about 0.3. The modification of the orifice diameter dependence was very little, and so the exponent in equation (12) was kept the same as equation (11). Equation (12) resulted to be the best of the proposed correlations, with correlation coefficient equal to 0.901. The corresponding plot is

reported in figure 6.15.

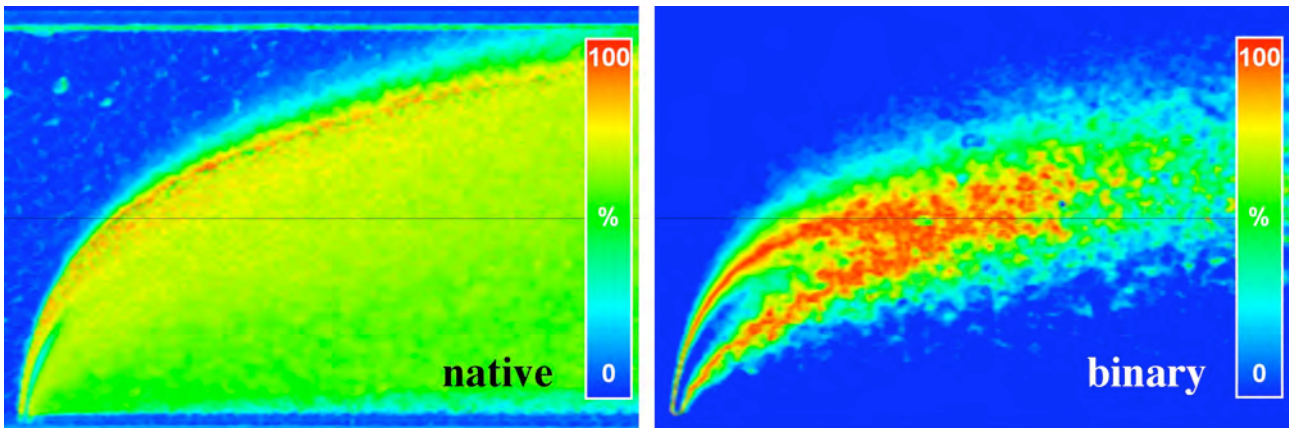


Figure 6.16. Standard deviation of native (a) and binary images (b).

6.3.2. Normalized intermittency index

Figures. 6.16a and 6.16b plot the standard deviation of native and binary images, respectively. It can be observed that in both images there is a region, near the injection point, characterized by values noticeably lower than the surrounding pixels. This fact can be quite plainly understood in the case of binary images, since it is expectable that a number of pixels have value constantly equal to 1 for all the 1000 sampled images, thus for those pixels the standard deviation is zero. Differently for the native image (figure 6.16a) there is a smaller group of pixels, whose values of light extinction intensity have low but non-zero variance. The region so individuated has not only no intermittency, which is reasonable since the proximity to the injection point prevents significant whipping, but it is also extremely stable, which seems to indicate that the attenuation of the light signal is attributable not only to the interposition of traveling droplets and fragments, but mainly to the presence of a more stable object, supposedly the liquid jet itself. The presence of this “virtual” liquid core was systematically observed for all test conditions, but a quantitative characterization has not been performed yet.

The standard deviation of the binary images can be further exploited to define a synthetic parameter accounting for the overall level of intermittency of the spray. This parameter is obtained simply by summing the intermittency over all the pixels of the image in figure 6.16b. The

availability of such parameter allows investigating the possible dependence of spray intermittency on the operating conditions. Aiming to avoid the biasing effect of the amount of injected liquid on the calculated value, the intermittency index was normalized by the average area of the sampled binary images. The resulting index was successfully plotted as a function of the liquid-to-air momentum ratio q , as reported in figure 6.17. The intermittency of the spray is high for low q values, therefore rapidly drops as q increases, and above $q \approx 50$ is nearly constant.

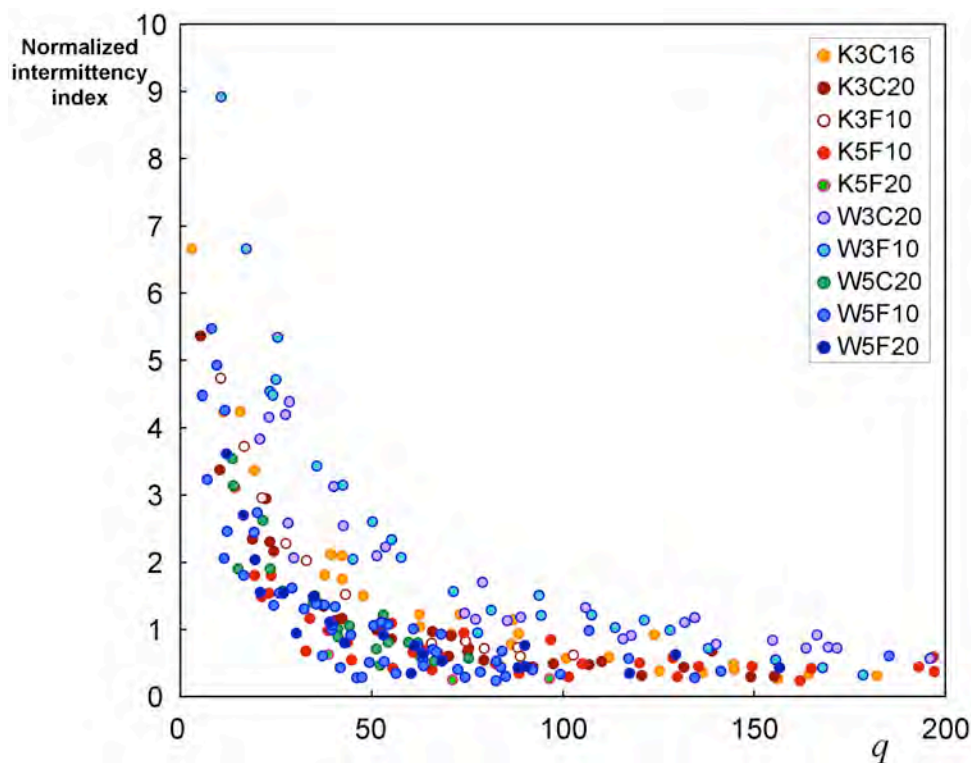


Figure 6.17. Normalized intermittency index as a function of liquid-to-air momentum ratio q .

It was observed that the spread of the data points could be reduced by introducing a further dependence on the dimensionless orifice diameter. Quite surprisingly, the exponent to be assigned to the dimensionless diameter to best reduce the data spread is very close to the value found before for the spray angle, as results in figure 6.18. The last figure also points out that kerosene points (in orange) place slightly below the water points (in blue). It is possible to suppose that the larger tendency to atomize of kerosene is responsible of a little lower level of whipping, although this effect has never been observed before.

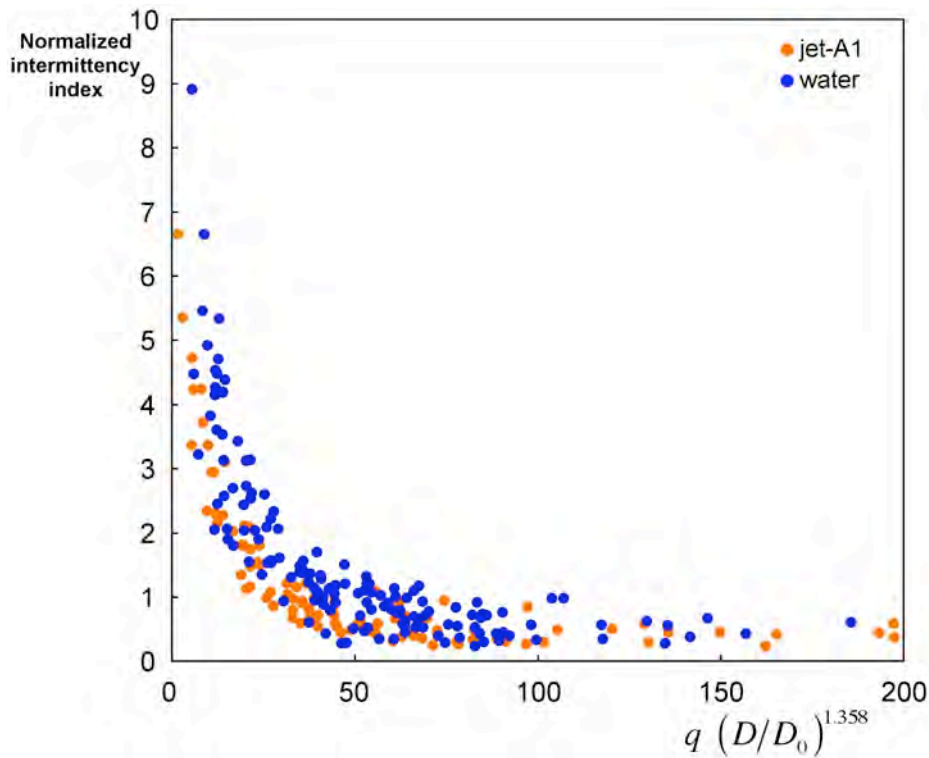


Figure 6.18. Effect of the orifice diameter on the intermittency index. Data points are grouped only by test liquid.

6.4. Relevance of the evaporation process

As regards the spray plume ensemble features, two further statistical indexes were evaluated, i.e. the overall surface of the pixels where light extinction is above the noise threshold, named spray extent and measured in mm^2 , and the normalized plume width in the liquid streamwise direction. The data used for these calculations are a subset including the same used for breakdown point computations reported in section 6.2, and other measurements for kerosene at 1 and 2 MPa. The choice of a limited subset is motivated need of high quality images of the spray, collected in illumination conditions as homogeneous as possible. Figure 6.19 presents the normalized plume width, plotted against the aerodynamic Weber number corrected by the square root of the density ratio. Although points appear relatively scattered, it is possible to deduce that the filling of the premixing duct gets better as the corrected Weber number increases. It is evident that a higher liquid velocity means larger penetration in the channel, but the dependence on Weber number also accounts for the effect of the atomization promoting the removal of larger amounts of drop and so

letting the spray cover the zone near the injection wall too. The growth of the plume width stops when the channel width is fully filled. The saturation of the channel, evident in figure 6.19 above a value of the abscissa of about 1500, sets an upper limit to the liquid flow rate, over which there are no further benefits on liquid dispersion in the channel. Data at either higher air pressure or temperature do not seem to differ from the other data sets, showing that the modification of these parameters only affects the spray dispersion through the variation of the air density. The presence of ρ_L in the abscissa essentially aims to let the parameter remain dimensionless. The scattering of points prevents inferring any dependence on a parameter such ρ_L , which ranges in a too narrow interval.

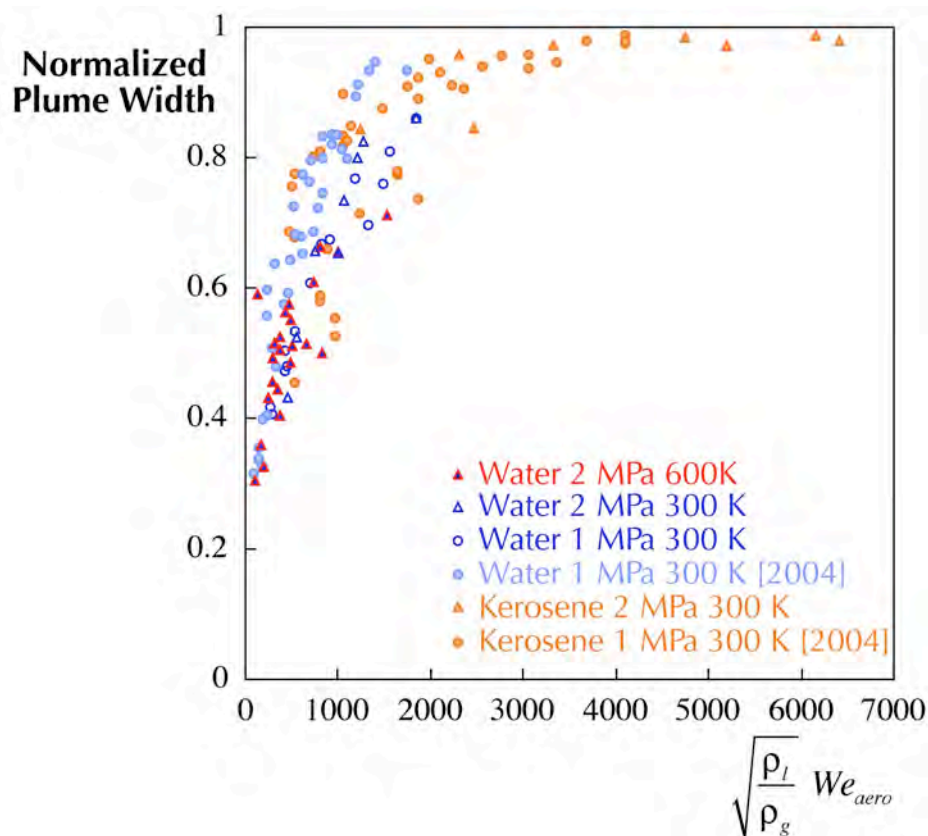


Figure 6.19. Normalized plume width as a function of the aerodynamic Weber number corrected by the square root of the density ratio.

Figure 6.20 reports the behavior of the spray extent, again plotted as a function of the aerodynamic Weber number corrected by the square root of the density ratio. As it could be

expected this parameter has a behavior similar to the plume width, even though in this case the experimental points are less scattered and show a lower level of saturation, due to the fact that the spray extent accounts for both plume width and downstream displacement of the spray. Anyway also in this case there is a reduction in the slope of the line suggested by the points in correspondence of the abscissa value where the plume width reaches its top and stops growing. The dependence on the corrected Weber number is not easy to explain. Probably the presence of a squared liquid velocity is attributable to the double effect of this parameter on both liquid flow rate, increasing the amount of liquid instantaneously interposing between the flash lamp and the digital camera, and atomization intensity, as already observed for x_{jb} .

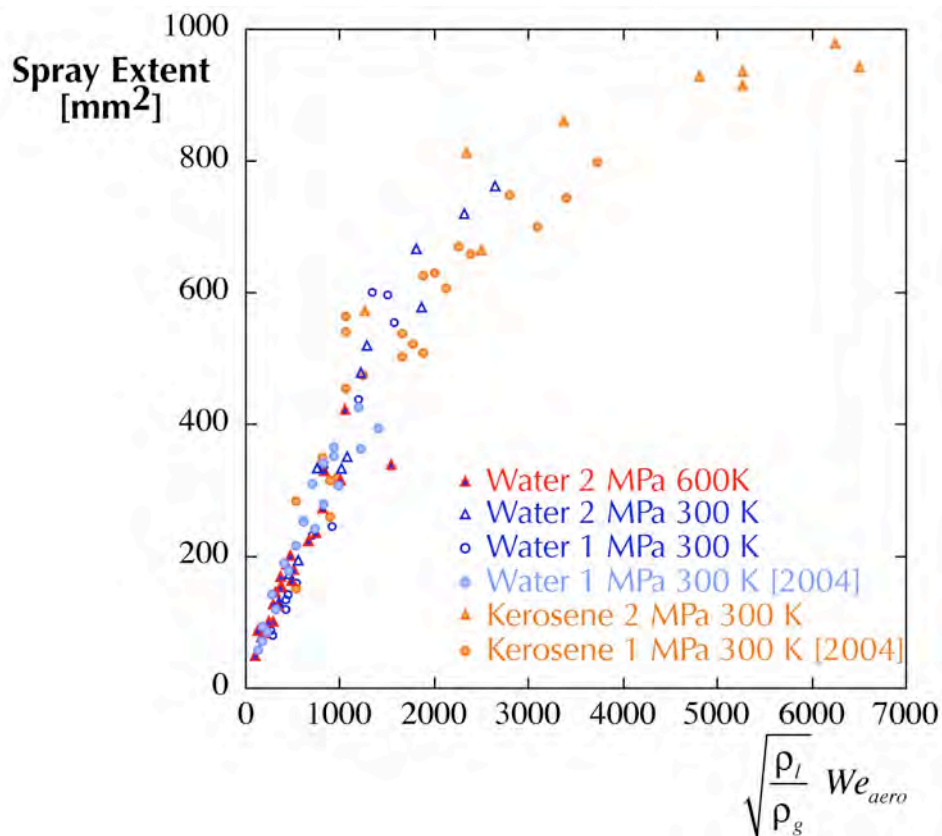


Figure 6.20. Spray extent as a function of the aerodynamic Weber number corrected by the square root of the density ratio.

Also in this case a higher temperature does not apparently have any other effect than reducing air density. One could expect that calculations on spray extent would point out an additional influence

of air temperature connected to the higher level of evaporation. Along with the evaluation of the spray extent, a possible effect of evaporation on the spray features has been further investigated by comparing images of water jets at the same liquid and gas velocity and the same air density but different temperature. The comparison of both single and average frames did not point out any substantial difference attributable to a more intense evaporation, and so was for the histograms of the distribution of light extinction intensity. From a theoretical point of view, the potential relevance of evaporation can be assessed by comparing the time characteristic of evaporation with the time characteristic of the fluid-dynamic transport. Starting from the point where they detach from the liquid jet, drops travel with a velocity that can be roughly assumed equal to the undisturbed air velocity. Another hypothesis is that the visible path they follow is about as long as a straight line linking the plane $x = 0$ corresponding to the liquid injection section with the downstream boundary of the collected image, that is no more than 50 mm. As a consequence each drop is visible by the camera for an order-of-magnitude time of about 1 ms. In order to estimate the evaporation time the steady state evaporation model is assumed. As well known this model predicts that the drop shrinks with a constant rate (Lefebvre, 1989), which has been assessed for water, in air at 20 bar and 600 K, as about $0.23 \text{ mm}^2/\text{s}$. With this value a water drop with an initial diameter of $10 \text{ }\mu\text{m}$ completely disappears in 0.43 ms, while a drop of $100 \text{ }\mu\text{m}$ lasts 43 ms. Since liquid is injected cold, this estimation of the evaporation time does not account of the heat up time, and so is lower than the actual time required by the drop to disappear. The agreement between experimental evidence and theoretical estimation seems to justify the hypothesis that, in the case of water injected in airflow at temperature up to 600 K, drops travel too fast to significantly evaporate within 100 diameters downstream the injection point, i.e. before leaving the region of interest of the adopted diagnostic setup.

Chapter 7. DESCRIPTION OF THE ABCD MODEL

7.1. Mathematical Formulation

This chapter introduces the elaboration and implementation of a numerical model for describing the behavior of a liquid jet, as it issues from a plain nozzle into a square channel (channel axis, x , is normal to the nozzle axis, z) and is suddenly exposed to an orthogonal airflow. The mathematical description of the process is formulated by assuming a two-dimensional system, therefore neglecting the direction normal to the plane xz defined by the axes of channel and nozzle. The model takes into account the Atomization and Bending of a Continuous Deformable jet in crossflow (ABCD model).

7.1.1. Momentum balance

A brief sketch of the physical model adopted to describe the crossflow atomization process is presented in figure 7.1.

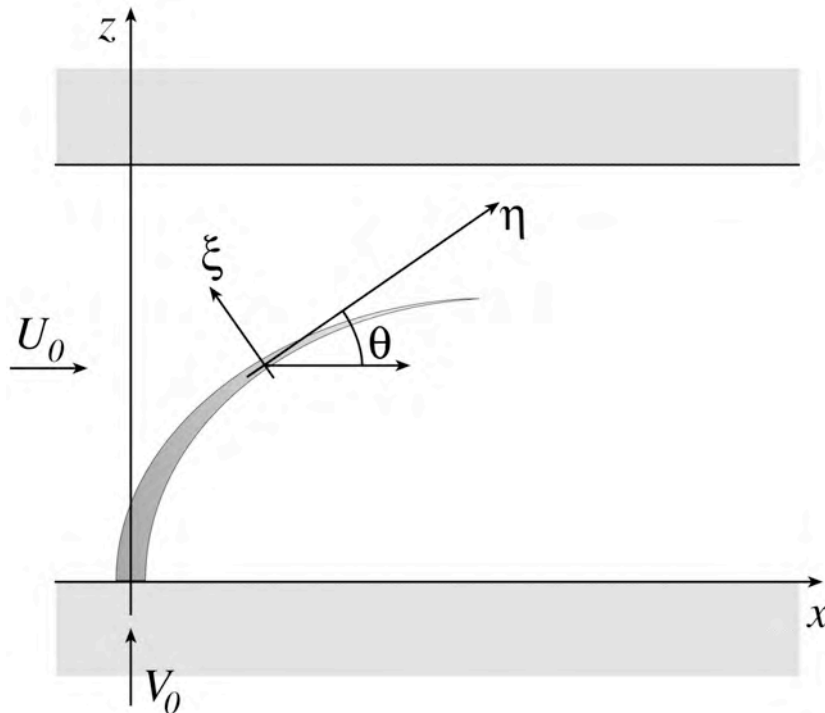


Figure 7.1. Sketch of the physical model and coordinate system.

In order to describe the jet trajectory, the momentum balance equations can be formulated in an eulerian frame of reference. The adoption of a curvilinear coordinate system $\xi\eta\zeta$ allows a better description of the physical problem. Keeping η everywhere tangent and equiverse to the jet trajectory, the problem is one-dimensional if liquid velocity components U and V , diameter D and deformation k are assumed to be uniform in directions normal to the jet trajectory. For a generic variable ϕ , the transport equation over the curvilinear coordinate η can be written as by Peyret (2000):

$$\frac{\partial}{\partial \eta}(\rho_L V \phi) = \frac{\partial}{\partial \eta} \left(\frac{\Gamma}{J} q \frac{\partial \phi}{\partial \eta} \right) + J \cdot S(\eta) \quad (1)$$

where V is the so-called contravariant velocity along η direction, Γ is the transport property of ϕ , J is the jacobian of the coordinate transformation from cartesian to curvilinear, q is a geometric coefficient. This equation can be integrated over a finite control volume and so transformed into a difference equation by applying the Gauss theorem. Being N and S the north and south face of the control volume:

$$(\rho_L V \phi)_N - (\rho_L V \phi)_S = \left(\frac{\Gamma}{J} q_{22} \frac{\partial \phi}{\partial \eta} \right)_N - \left(\frac{\Gamma}{J} q_{22} \frac{\partial \phi}{\partial \eta} \right)_S + S_\phi \quad (2)$$

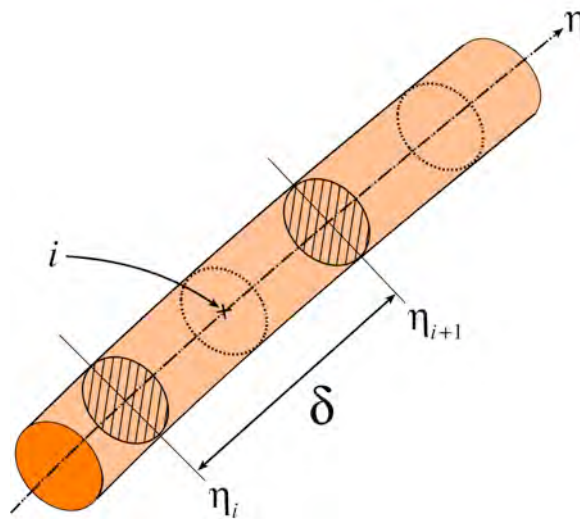


Figure 7.2. Scheme of the discretization of the eulerian flux tube representing the liquid jet.

In this case the chosen control volume is the finite portion of liquid jet lying between η and $\eta + \delta$. The spatial discretization δ , sketched in figure 7.2, is kept constant over the whole trajectory. Convective terms can be managed by means of a first-order upwind scheme.

7.1.2. Jet cross-section deformation and drag forces

The source term S in equation (2) includes the drag force acting on the jet, as usual taken proportional to the dynamic pressure $1/2 \cdot \rho_G V_G^2$ and the effective area normal to the undisturbed airflow. This effective area can be calculated once the jet cross-section deformation has been evaluated. To this aim a further sub-model was set up to perform a lagrangian tracking of the variable k , defined as the ratio between the major axis of the flattened ellipse and the local value of the un-deformed jet diameter. Figure 7.3 plots an outline of the cross-section of the deformed liquid jet. The classic TAB model by O'Rourke and Amsden (1987) was purposefully adopted and the following profile was obtained for k :

$$k = 1 + We \frac{c_F}{c_k c_b} \left[1 - \exp\left(-\frac{t}{t_D}\right) \left(\cos \omega t + \frac{1}{\omega t_D} \sin \omega t \right) \right] \quad (3)$$

where the parameters We , ω and t_D are defined as

$$We = \frac{\rho_G U_\infty^2 D}{2\sigma} \quad (4)$$

$$\frac{1}{t_D} = \frac{C_m}{2} \frac{\mu_L}{\rho_L (D/2)^2} \quad (5)$$

$$\omega = C_k \frac{\sigma}{\rho_L (D/2)^3} - \frac{1}{t_D} \quad (6)$$

and the constants C_i are assumed as

$$\begin{aligned}
 C_F &= \frac{1}{3} & C_k &= 8 \\
 C_m &= 5 & C_b &= \frac{1}{2}
 \end{aligned}
 \tag{7}$$

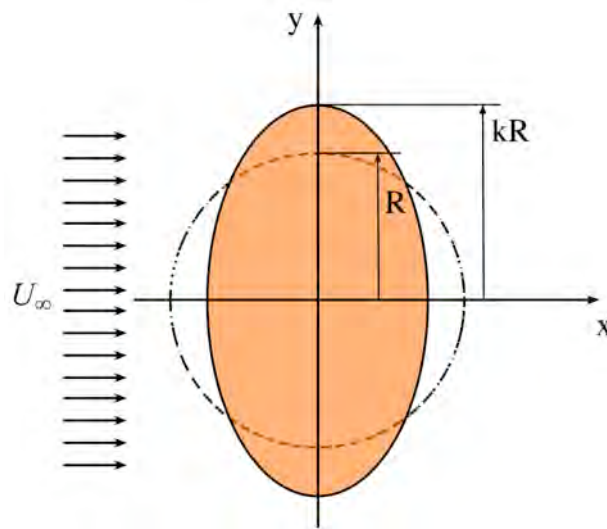


Figure 7.3. Scheme of the elliptical deformation of the liquid jet cross-section, as described by the TAB model.

With the aforementioned assumptions the drag force in the momentum balance equations, for the liquid velocity components U and V respectively, takes the following expressions:

$$F_U = C_D \cdot \frac{1}{2} \rho_G (U - U_\infty)^2 \cos \theta \cdot 2kD\delta \tag{8}$$

$$F_V = -C_D \cdot \frac{1}{2} \rho_G V^2 \sin \theta \cdot 2kD\delta \tag{9}$$

The value of the drag coefficient was calculated at each point of the discretized trajectory as a function of the Reynolds number, referring to a flow over a solid circular cylinder of infinite length.

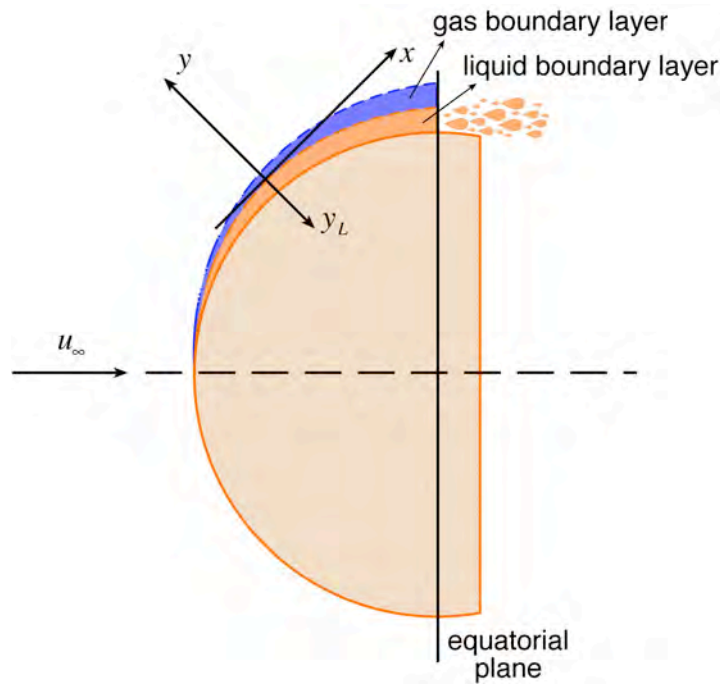


Figure 7.4. The double boundary layer on liquid jet boundary, and a sketch of the mechanism of liquid stripping.

7.1.3. Mass balance and atomization model

The continuity equation can be obtained from equation (1) or (2) by setting $\phi = 1$. In this case the source term accounts for the mass removal from the jet due to atomization. The Boundary Layer Stripping (BLS) model (Ranger and Nicholls, 1969) states that a double boundary layer forms at the liquid-gas interface, and that the amount of liquid stripped away coincides with the liquid flow rate in the boundary layer at the equatorial plane, normal to the airflow and defined as outlined in figure 7.4. Extreme ease of implementation and absence of parameters to be experimentally tuned are the major benefits of this model. On the other hand the BLS model shows some unrealistic features, as it is based on the hypothesis of circular cross-section and moreover it does not account for the influence of surface tension on the atomization process. By integrating over the finite control volume the Boundary Layer Stripping model provides the following expression for the mass shedding rate (Bellofiore et al., 2004):

$$\dot{m} = \delta \sqrt{6\pi D \rho_L \mu_L \left(\frac{\rho_G}{\rho_L} \right)^{1/3} \left(\frac{\mu_G}{\mu_L} \right)^{1/3} U_\infty} \quad (10)$$

7.2. Boundary conditions

7.2.1. Determination of air velocity profile

Computations presented in this study have been made considering two different conditions for the velocity of airflow, U :

1. A uniform profile without considering the effect of the boundary layer.
2. A variable velocity profile taking in account the existence of turbulent boundary layers on the walls of the duct, developing from the inlet section to the section of the liquid jet.

In this second case the air mass flow rate in the section is given by:

$$w = 4\rho \int_0^{h/2} \int_0^{h/2} U \, dydz \quad (11)$$

If we consider a velocity profile inside the boundary layer that follows the exponential law 1/7, typical for turbulent flows, we obtain a relation between the average and maximum velocity in the cross section of the duct:

$$\bar{U} = U_{Max} \left[\frac{1}{64} \left(\frac{\delta}{h/2} \right)^2 - \frac{1}{4} \left(\frac{\delta}{h/2} \right) + 1 \right] \quad (12)$$

Where U_{Max} is the maximum air velocity on the axis of the duct, h is the size of the section side and δ is the boundary layer thickness at a distance x from the entrance section, where a flat profile is assumed, given by:

$$\delta = \frac{0.37x}{(\rho_G U_{Max} x / \mu_G)^{0.2}} \quad (13)$$

In the experimental setup, used to build up the validation database, the air velocity was measured at the centre of the channel at a distance of 140 mm from the inlet section. From equation (12) it was derived the average air velocity assuming that the measured velocity corresponds to the maximum velocity. The injection section was at 420 mm from the inlet section and the velocity

profile at this position was computed using the expression:

$$U(y) = U_{Max} \left(\frac{y}{\delta} \right)^{\frac{1}{7}} \quad (14)$$

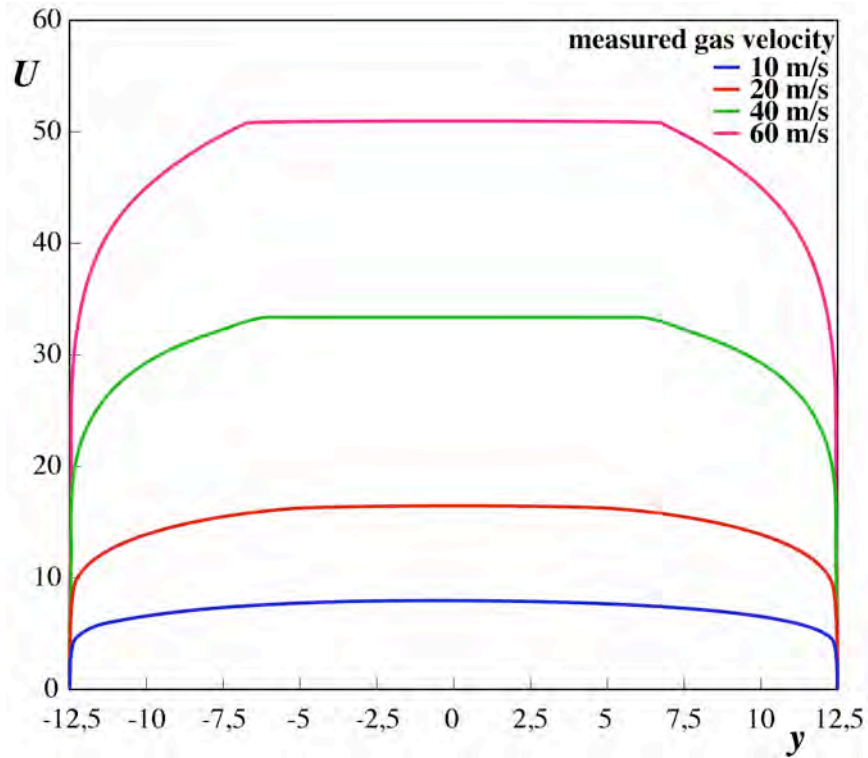


Figure 7.5 Velocity profiles as evaluated using the procedure described in the study and used in the computation of the jet trajectory.

The determination of $U(y)$ at the injection section required an iterative computation since U_{Max} and δ are related through the equations (12) and (13). To this aim the value of U_{Max} was assumed as a first guess equal to the average velocity. The value of the boundary layer thickness, δ , was then computed using this value from equation (13) and used to evaluate the next iterative value of U_{Max} using equation (12). The procedure converged rapidly to a stable value of the U_{Max} to be used in the determination of the air velocity profile according to the equation (14).

Examples of the velocity profiles computed using the above reported procedure are reported in figure 7.5 for values of the measured velocity from 10 to 60 m/s.

7.3. Model validation

The simultaneous integration of momentum and continuity equations along with the deformation equation provided predictions of jet trajectory to be compared with experimental measurements obtained from flash shadowgraphy images collected by injecting kerosene and water in a high-density air crossflow.

The model has been validated against the whole experimental database, relative to about 300 conditions, described in chapter 4. A synthetic view of the experimental conditions used in the plane $q - We_{aero}$ is reported in figure 7.6. Starting from a set of 1000 images for each condition a fully automated statistical procedure allowed obtaining a set of jet upwind trajectories. This set has been used to evaluate the model effectiveness in describing the jet profile.

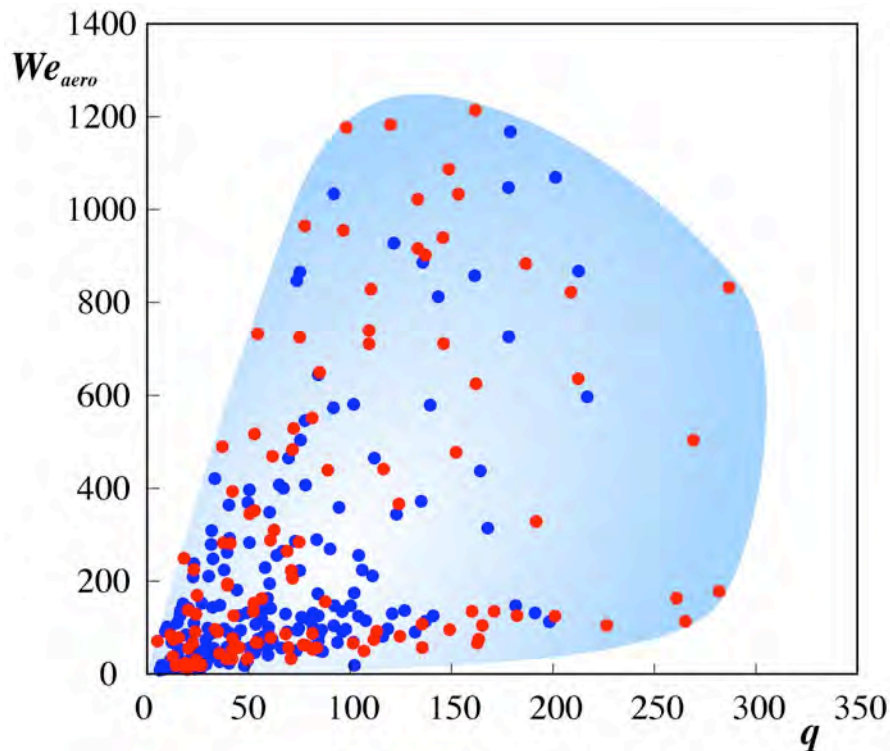


Figure 7.6 Envelope of the experimental conditions in the $q - We_{aero}$ plane. Blue and red dots are relative to low (300 K) and high (600 K) temperature airflow conditions, respectively.

Chapter 8. RESULTS OF THE NUMERICAL MODEL

A general overview of the model performance in reproducing the experimental results is reported in Table 8.1 and Table 8.2. The two tables refer to simulations performed by assuming either a uniform velocity profile or a variable velocity profile elaborated following the procedure outlined in the previous section. In these tables the RMS error, normalized to the average value of the experimental profile, along with the correlation coefficient R have been reported for the different datasets collected in the experimental database. A smaller value of the RMS indicates a lower overall deviation of the computed profile with respect to the experimental one. A value of R closer to 1 indicates that the form of the numerical profile reproduces better the form of the experimental one.

The agreement between the model results and the experimental data is generally satisfying. The global RMS error for the uniform velocity profile case was 0.109 with an R equal to 0.865. Results were even better when the variable velocity profile was assumed. In this latter case the RMS was equal to 0.096 and the R was equal to 0.897. For the same experimental conditions the values obtained using the correlation

$$\frac{z}{z_{jb}} = \left(\frac{x}{x_{jb}} \right)^{0.367} \quad (1)$$

were 0.047 and 0.980 respectively. As a comparison using the correlation suggested by Becker and Hassa (2002) the RMS error and the correlation coefficient were 0.104 and 0.791 respectively. The RMS error was, for this correlation quite similar to the one obtained by using the numerical model but the R was significantly lower indicating that the correlation missed to reconstruct the profile behavior. The performance of the correlation suggested by Wu *et al.* (1997) were quite poor being the RMS error = 0.186 and the R = 0.345.

Uniform velocity profile		1.0 MPa	1.6 MPa	2.0 MPa	
		300 K	600 K	300 K	600 K
water	nozzle 0.3	0.144 0.721			0.160 0.731
	nozzle 0.5	0.099 0.893		0.105 0.871	0.087 0.933
Jet A1	nozzle 0.3	0.098 0.921	0.085 0.931		0.102 0.880
	nozzle 0.5	0.102 0.898		0.079 0.928	

Table 8.1. RMS errors (in red) and correlation coefficients R for the different datasets used in validating the model for the uniform velocity profile case.

Variable velocity profile		1.0 MPa	1.6 MPa	2.0 MPa	
		300 K	600 K	300 K	600 K
water	nozzle 0.3	0.142 0.760			0.137 0.785
	nozzle 0.5	0.082 0.922		0.103 0.882	0.089 0.941
Jet A1	nozzle 0.3	0.059 0.974	0.059 0.972		0.074 0.939
	nozzle 0.5	0.098 0.910		0.078 0.937	

Table 8.2. RMS errors (in red) and correlation coefficients R for the different datasets used in validating the model for the variable velocity profile case.

The proposed numerical model does not perform equally well in all the conditions and there are some cases (in particular those relative to water injections in cold conditions with the 0.3 mm nozzle) that would deserve further consideration in order to clarify the reason for the model relatively poor performance.

To this aim it is interesting to analyze in detail the error behavior in dependence of the particular condition. For each case reported in Tables 8.1 and 8.2 the RMS errors and correlation coefficients reported are the average over a set of about 30 conditions of airflow and injection velocities each. In figures 8.3 and 8.4 the values of RMS error and of the quantity $1 - R$, for injections of Jet-A1 in

airflows at 600 K under a pressure of 1.6 MPa, are graphically represented in the plane $V-U$ as circles of radius proportional to their values for both the velocity profile types used in the computation.

A larger circle in figure 8.3 indicates a higher RMS error. It can be easily seen from the figure that the maximum discrepancy between the experimental data and the computed ones occur at low liquid injection velocities. In these cases there is a significant improvement in the results if a non-uniform velocity profile is assumed. This is a general trend apart from the conditions at higher airflow and liquid velocities (upper right region of the plot) where the model performance is very good for both assumptions.

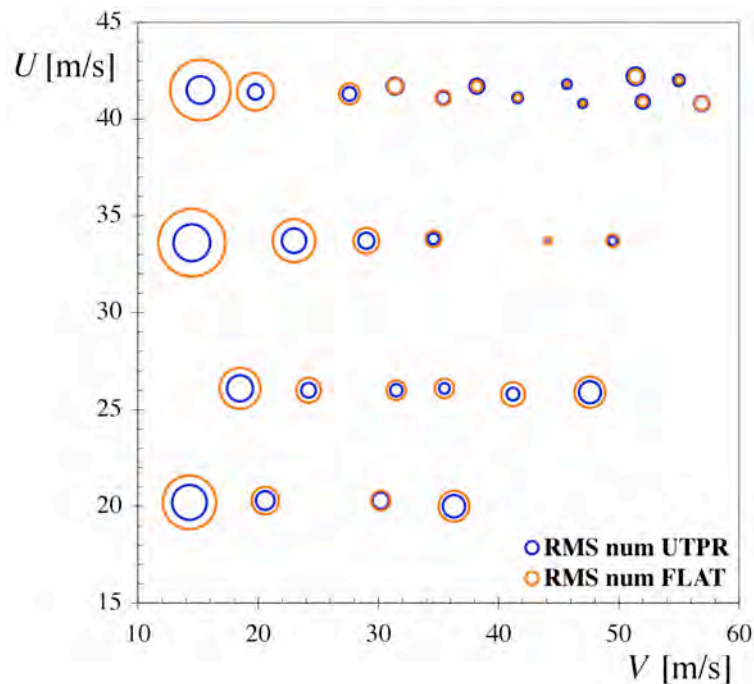


Figure 8.3. Graphical representation of the RMS errors for the test cases relative to Kerosene injections in 1.6 MPa and 600 K airflows for both velocity profiles assumptions.

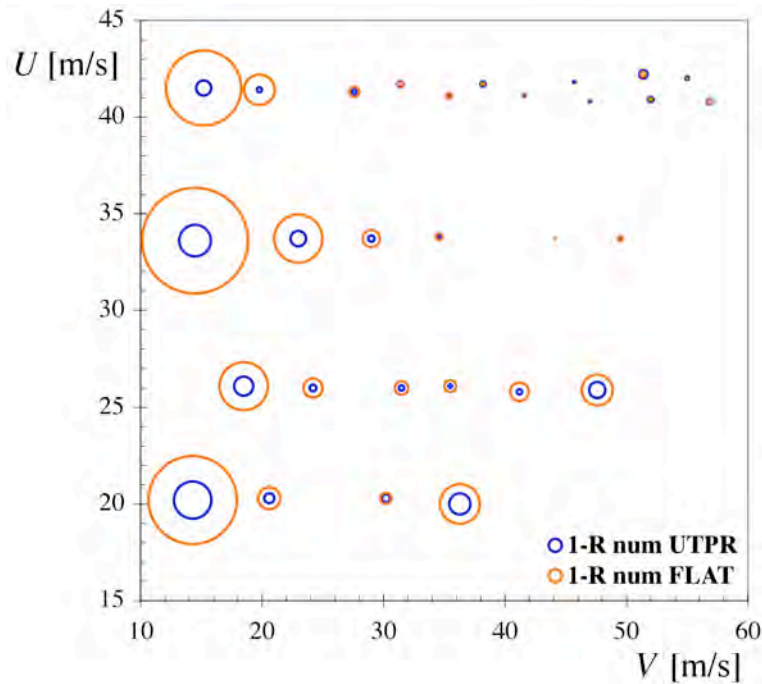


Figure 8.4. Graphical representation of the quantity $1-R$ for the test cases relative to Kerosene injections in 1.6 MPa and 600 K airflows for both velocity profiles assumptions.

In figure 8.4 the values of $1-R$ have been reported to evidence the deviation of the computed jet trajectories from the experimental ones. In this case too a greater circle indicates a greater deviation. Results are quite similar to the ones reported in figure 8.3 but the greater difference between the two velocity profile assumption indicates that the improvement obtained by considering a non uniform velocity profile is more connected to a better reconstruction of the jet profile shape than to the reduction of the distance between the experimental and computed profiles.

In figure 8.5 the jet trajectories computed using the model are compared with the experimental data and with those obtained using the generalized jet trajectory formulation reported in equation (1) for four different cases among those reported in figures 8.3 and 8.4. Model results are also compared to the results obtained by using the correlations proposed by Wu et al. (1997) and Becker and Hassa (2002). This comparison is significant since in the literature these formulations (and particularly the first one) are often used to describe the jet trajectory in the implementation of jet atomization models. It has to be stressed here that the use of a semi empirical or fully empirical correlations to describe the jet trajectory in a CFD simulation of a premixing duct of a gas turbine

combustor may seem very convenient due to their very simple formulation. On the other hand it has to be noticed that these formulations, as well as the several correlations reported in literature, have been obtained in very peculiar conditions of a uniform or almost uniform velocity profile with an incidence of the airflow perpendicular to the injector axis. These pose severe limitations to their use in modeling the jet behavior in a very complex fluid-dynamic situation like the one commonly occurring in a real device. The approach proposed in the present study is much more effective in describing correctly the jet trajectory due to its more general nature. In fact, even if the validation presented here is limited to the canonical orthogonal intersection between the airflow and the injector axis, there is no limitation to its use with a different intersection angle and with an arbitrary air flow-field.

For the cases in figures 8.5a and 8.5d the agreement is very good for both the models and correlation of equation (1). In these cases the correlations proposed by Wu et al. (1997) and Becker et al. (2002) overestimate or underestimate the jet penetration respectively. In the case in figure 8.5c both the numerical model and the correlations failed to describe the jet trajectory by underestimating the penetration at low x values and overestimating it at higher x . In the case in figure 8.5b the situation is even worse.

Reasons for the poor performance of the model in these latter conditions can be the inadequacy of the atomization sub-model to describe the liquid removal from the jet or an incorrect modeling of jet deformation at low airflow velocities.

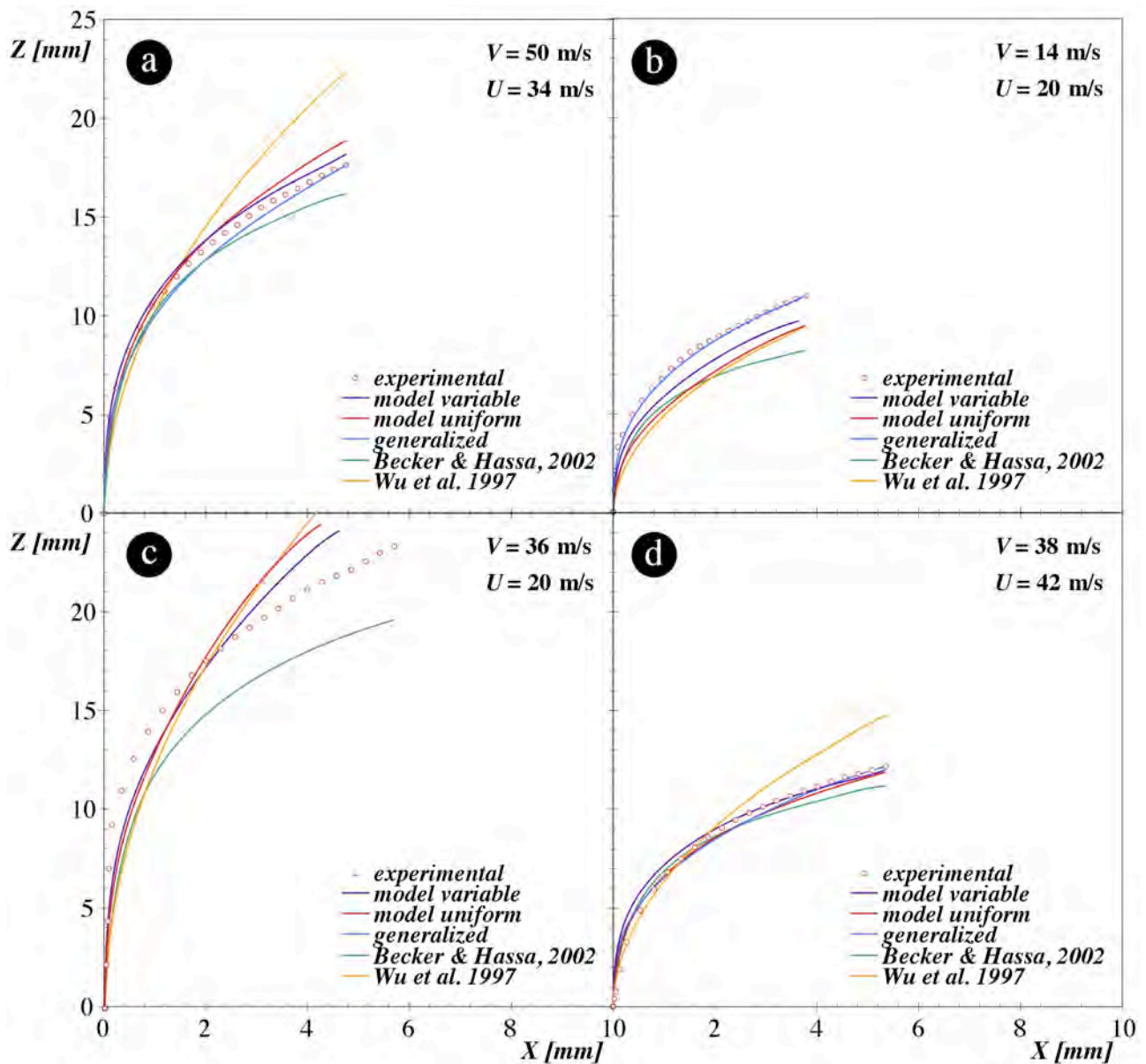


Figure 8.5. Comparison of the computed jet profiles with those determined experimentally or by using the correlations presented by Wu et al. (1997), Becker and Hassa (2002) and in chapter 6 of this thesis (generalized model).

Chapter 9. DISCUSSION

The achievement of more efficient and less polluting gas turbines relies on the development of new combustion systems, as the model combustors presented in chapter 1. Among them, the LPP technology, the possibility to get, in the very next future, a breakthrough in the field of low pollutant combustion, with a dramatic drop of nitrogen oxides emissions. The implementation of lean premixed combustion concept seems to be at hand, but several issues are still to be faced, issues polarizing around two major concerns. The first problem stems from the difficulty to confine and stabilize the reaction in a defined zone of the combustion chamber, thus preventing flashback and premature ignition. The second problem is the lack of stability typical of premixed combustion systems operating close to the lean blow-off limit. In recent years experimental investigation pointed out the boosting effect of operating pressure on both the problems. On the other hand it was observed that the an important relief has to be searched in the development of improved premixing systems, since fast and effective achievement of homogeneous uniform air-fuel mixture produces:

- reduction of residence time in the premixer, thus contrasting the occurrence of premature ignition;
- possibility to increase flow velocity at the combustor inlet, so reducing the risk of flashback;
- decrease of the occurrence of non-uniformities in the mixture fed to the combustor, probable source of combustion instability;
- global lowering of primary temperature, along with suppression of temperature peaks, allowing a massive reduction of NO_x emissions.

The adoption of a crossflow atomization scheme appears a feasible way to design a compact premixer, equipped with a simple and robust injector and able to match the requirement of fast and virtually complete mixing and vaporization of the liquid fuel in the gas phase. The experimental and numerical study so far presented aimed to investigate the effectiveness of such spraying system in

conditions close to the operation of real engines, and to achieve, by means of a deeper comprehension of the interaction between injected liquid and air crossflow, suggestions useful for designers about the dependence of the atomization and dispersion characteristics on operating parameters.

The investigation of the behavior of a liquid jet in crossflow is object of increasing interest in last years, and so a number of studies, both experimental and numerical, is being issued. Chapter 2 accounts for the several approaches, even though it seems that the research is unable to move beyond a limited cluster of ideas, which have been maybe discussed enough for the last ten years. The first constrain is the range of operating conditions. Although the purpose of address the investigation to the employment of crossflow atomization in combustion systems is frequently claimed, nonetheless only few studies deal with combustion-oriented operating conditions. This Ph.D. thesis is part of research project pivoted on the investigation of conditions of interest for LPP gas turbines. One basic target was therefore to validate and extend the knowledge on crossflow injection to a poorly explored field. In addition the present thesis introduced three novel elements: the individuation, by means of literature experience and phenomenological investigation, of the ruling mechanisms of the process, resulting in the development of a numerical model able to predict the jet penetration with remarkable accuracy; the operative definition of two parameters, the breakdown point coordinates, resulting to be the scaling factors of jet penetration; finally the implementation of an original statistical approach for the study of spray evolution. These aspects are discussed in the following of this chapter.

9.1. Ruling mechanisms in the crossflow atomization process

The study focused on injection conditions characterized by an intense level of atomization, which is the most probable situation in gas turbine practical operation. Nevertheless some interest was also devoted to the study of phenomenological aspects in moderate conditions. This qualitative analysis corroborated the idea that a variety of processes concur in the distortion and atomization of

the liquid jet. First of all the interaction of the jet with the transverse airflow promotes the development of several modes of instability. Very slow liquid jets mainly undergo large amplitude distortion, with wavelength comparable more with the length of the jet than with its diameter. This kind of instability does not produce atomization, but only distorts the jet until it fractures in few pieces. In a number of collected frames it was possible to observe fully developed bags, blown by the airflow, indicating that in this conditions the process is quite slow to allow this phenomenon. This large-scale distortion survives also at stronger aerodynamic conditions. This seems to be partly responsible of the results from quantitative measurement of jet whipping, presented in subsection 6.3. At low q number the normalized intermittency index increase, also because in this zone the lower atomization intensity allows for the subsistence of columns distortions causing the jet to whip.

Another concurrent phenomenon can be hypothesized to explain the intermittency growth at moderate atomization regimes, and it is also connected with the interplay between the different instability modes. When the aerodynamic pressure is weaker and then the spectrum of excited frequencies shifts towards lower values, the atomization mode based on stripping mechanism affects a reduced amount of liquid mass. As a consequence more liquid undergoes final column fracture in large fragments, whose detachment is intermittent and more traumatic than continuous stripping from jet surface and so its inertial feedback onto the jet can be considered accountable for whipping. The characteristics of fragment clipping, such as size and detachment delay, depend on surface tension, and this should justify the higher level of whipping observed for water jets, in which the higher surface tension would produce slightly delayed separation and then higher intermittency.

Phenomenological investigation also demonstrated the progressively growing relevance of small-scale instabilities, as the aerodynamic pressure increases. The classification of bag, multimode, shear and atomization regimes was presented, as usual, by sorting the collected image by Weber number. It is interesting to point out that all the collected images of the main database,

used in subsection 6.2 for quantitative statistical analysis, can be plainly classified as atomization regime, since high-frequency short waves and stripping mechanism dominate the atomization process. It means that all the quantitatively investigated conditions fall in a range of Weber number in which, as already pointed out by Clark (1964), the interplay between aerodynamic and capillary forces does not play a dominant role on the process. This fact is of utmost importance, in order to understand the experimental evidence that all the main features of the spray show a major dependence on a dimensionless parameter, the liquid-to-air momentum ratio q , which does not embed surface tension. The capillary forces play a role when aerodynamic forces are less preponderant, and in those conditions surface tension determines which is the dominant regime. When the Weber number is so large, as in conditions of interest for gas turbine operation, capillary forces cannot be expected to be able to influence the behavior of the jet so much. The liquid-to-air momentum ratio resulted to strongly influence penetration, dispersion and even the level of intermittency of the jet, with only a minor influence of Weber number, except for the results on jet displacement in the gas-streamwise direction.

Results obtained from numerical investigation seem to corroborate the statement that the capillary pressure is not dominant even for the atomization process. As point of fact the atomization sub-model is based on the Boundary Layer Stripping scheme, which completely neglects the effect of surface tension of the mass removal rate. In spite of this allegedly strong drawback, the numerical model demonstrated an excellent prediction capability in most of the about 300 experimental conditions used for validation. This evidence suggests that in all the conditions of interest for gas turbines the full atomization regime suppresses most of the influence of capillary pressure detected in other conditions.

A partial amendment of this statement is necessary to account another evidence from numerical simulation. It was observed that a preliminary version of the model, implemented without taking into account the process of deformation of the jet cross-section, used to give significantly worse prediction. In particular this version seemed to fail to describe the actual bending of the jet,

therefore calculated jets used to be less deflected in the airstream direction than experimental evidence. The occurrence of jet flattening is experimentally suggested by the observed jet width reduction in the x-direction, as detected from the digital camera. The introduction of a deformation sub-model accounting for jet flattening by means of an adapted form of the TAB model allowed for a more accurate prediction of jet trajectory. What is important to stress is that the TAB model is based on the interplay between aerodynamic and capillary forces, therefore it introduces into the ABCD model the effect of surface tension. In the proposed model, the trajectory (or penetration) of the jet, apart from the dominant role of the momentum exchange between phases, is affected by both jet *flattening*, due to deformation, and *shrinking*, due to atomization, but only the former mechanism embeds the influence of the Weber number.

The deductions so far inferred from experimental and numerical evidence on the ruling mechanisms in crossflow atomization process are in fairly good agreement with the theoretical assumptions of Clark (1964) and experimental observations found in literature (Nejad and Schetz, 1984). Other authors (Wu *et al.*, 1997, Becker and Hassa, 2002) proposed a classification of the investigated conditions by introducing two jet atomization mechanisms: *column breakup* and *surface breakup*, the latter being dominated by the stripping of small droplets from liquid surface. The general trend found by those authors is that the jet undergoes surface breakup when simultaneously the liquid dynamic pressure overcomes gas dynamic pressure (large q) and the latter dominates over capillary pressure (large gas Weber number). Wu *et al.* (1997) state that the borderline between the existence of either the two regimes roughly corresponds to the condition

$$q \propto We_G^{-0.81} \quad (1)$$

and this results seems to be confirmed by Becker and Hassa (2002). Being it based on approximate qualitative observation, equation (1) can be promptly simplified by the formula $q \cdot We_G = \text{constant}$, that is to say $We_L = \text{constant}$. In other word it is probable that the map of regimes can be replaced, with good approximation, by the assumption of a threshold level of liquid

Weber number separating column and surface breakup regimes.

As regards the investigation of jet penetration and breakdown, the correlations shown in subsection 6.2 have been obtained after several attempts aimed to find other parameters, which could scale the jet bending topology. Great number of these were based on the identification of breakup characteristics which are expected to influence the jet deceleration, but they were far to be suitable for any type of scaling when objective automatic procedure were used. The lack of space and the positivistic approach of scientific communication prevent from a documentation of these aspects. Nevertheless it is noteworthy to report that these approaches mainly failed because jet breakup and contact length were not the significant parameters. In other words no correlation could be based on contact length detection even if in crossflow injection conditions this was easier to be determined in respect to the case of high velocity jet used in the diesel engine. As matter of fact for transverse injection the obscuration from high-density small-droplet cloud is not so high due to the crossflow entrainment, which sweeps and “cleans up” the upstream edge profile of the jet. In spite of this jet breakup detection is not straightforward, also under moderate conditions, where the whole breakup process could be characterized, and therefore results are not consistent. For high Weber number the problem of jet envelopment by a cloud of droplets is more relevant, whereas at lower values liquid column instability have been observed to enhance a three-dimensional evolution of the jet, which allows superimposition of its convoluted parts, undermining the reliability of direct visualization.

In synthesis the measurements based on breakdown of momentum coherence are objectively feasible, whereas parameters based on breakup process are not easy to be detected and they are not representative in scaling the jet bending. The statistical elaboration performed in this thesis demonstrated that the evaluation of an event, the breakdown, which represent not a physical fracture but a statistical loss of coherence, is of higher usefulness since it individuates two lengths, the breakdown point coordinates x_{jb} and z_{jb} , able to work as normalizing factors for jet penetration. An

important consequence is the statement of the self-similarity of the jet trajectory. The shape of the windward profile from the injection up to the breakdown event is known *a priori* for every test condition within the investigated range. All the possible jets differ from each other only as regards the scaling factors x_{jb} and z_{jb} . This is quite surprising, and seems to point to the existence of an underlying shared behavior, connected to the atomization regime common to all the explored conditions. In other words in the regime of full atomization, typical of gas turbine conditions, the history of deflection, distortion, and allegedly also shrinking, is already written, the only missing piece of information being the time extent over which it develops.

It is quite striking and of great technological interest that the equations reported in chapter 6, which describe the jet trajectory, are virtually not dependent on Weber number. On the opposite both coordinates of the jet breakdown point are sensitive to this type of dependence, although We_{aero} more strongly affects x_{jb} . These results are implementations of previous literature work (Wu *et al.*, 1997, Becker and Hassa, 2002) where the surface tension effects were not taken into account. The results are quite robust because the change of surface tension, passing from water jet injected in air at room temperature to Jet A-1 injected in a high-temperature environment, implies a change of aerodynamic Weber number higher than one order of magnitude. Anyway the only significant inaccuracy, which an approximated evaluation of the surface tension could imply, is on x_{jb} and not on z_{jb} since the dependence on the Weber number of the second is very low. Furthermore it is noteworthy that the value of z_{jb} fixes the region where a possible confinement wall should be located, because downstream of this coordinate the spray undergoes large fluctuation characteristics which are not compatible with a stable prevaporization, and consequently with a stable combustion.

The different influence of surface tension variation on the two jet breakdown point coordinates can only be explained by processes of deformation of blob, ligaments and droplets, and not by the atomization process. In fact, some deformation characteristics can be aligned preferentially along one direction, with consequent preferential entrainment, due to shape peculiarity and surface

increase, along the same direction. On the opposite liquid fragmentation entails a reduction of average size and increase of total specific liquid-gas interface, which should affect, in turn, both deceleration along z-coordinate and acceleration along the x-coordinate.

9.2. Penetration and dispersion of the liquid jet

The statistical analysis applied to the whole spray allowed for introducing the definition of centerline, resulting from the evaluation of the locus of highest recurrence of the spray core. It is to further stress the statistical nature of this line, in contrast with the previously defined trajectory line, which individuates the observable upper boundary of the spray by means of a repeatable statistical procedure. The centerline does not describe any observable item on the spray images, nor it points out a region characterized by some physical features, such as maximum liquid density. The threshold operator is based on the analysis of gray levels of the image, connected to the amount of liquid interposing between light source and camera, but the binarization itself cuts off any further information on light extinction intensity. The result is a set of 1000 flat areas, which are representative of the spray core location and differ from each other due to the unsteadiness of the process, in particular due to *intermittency*. As a consequence the overlapping of such areas is incomplete and the zone with the maximum overlapping rate is represented by the centerline, which can be therefore considered the pivot of spray whipping.

The centerline, better than the jet trajectory placed on the periphery of the spray, can be elected as representative of the line over which the spray evolves from the injection up to eventual breakdown. The very operative procedure for the determination of the centerline is based on the use of the centerline as curvilinear coordinate of the spray propagation direction. This approach promises to be powerful in the study of evolving features of the spray, as testified by the example reported in this thesis, concerning the spray angle.

The availability of reference lines for both the boundary and the center of the spray suggested the chance to use them to investigate the characteristics of initial dispersion of the spray in the

premixer. The subsequent introduction of spray angle in the study of crossflow injection was presented in subsection 6.3.1. It is meant to achieve a quantitative evaluation of the ability, in certain operating conditions, to spray the liquid over the whole width of the premixer. In chapter 6 a procedure for measuring the spray angle was introduced. This procedure operates on the trajectory and centerline as arrays of points, as they were assessed by the statistical analysis routine. That way it was possible to evaluate, for each condition, the average value of the angle between the two curves. A non-linear regression of the experimental data for the spray angle pointed out a dependence on liquid Weber number and injection diameter, along with a minor influence of gas dynamic pressure. An analytical approach to this problem requires the assessment of jet trajectory and spray centerline in form of equations. Empirical model for jet penetration was already proposed in chapter 6. Aiming to derive an analytical formulation of the spray angle dependence from dimensionless parameters, here a simplified form of the equation for jet trajectory is adopted:

$$\frac{z}{D} = 2.75 q^{0.44} \left(\frac{x}{D} \right)^{\frac{1}{3}} \quad (2)$$

This equation differs from the previous one, since the weak dependence on aerodynamic Weber number has been neglected and the simplified exponent 1/3 replaces 0.367. The error of this equation, with respect to the original form, is less than 10%. A non-linear regression of the data collected for spray centerline allowed for calculating an analytical equation for its prediction. By imposing a similar functional dependence it was found the equation

$$\frac{z}{D} = 0.6 q^{0.25} \left(\frac{x}{D} \right)^{\frac{2}{3}} \quad (3)$$

showing that in general the centerline presents a less bent shape than trajectory and lower dependence on the liquid-to-air momentum ratio. Figure 9.1 shows the behavior of jet trajectory and spray centerline as q increases, the injection diameter being kept constant. Since the red line, representing the centerline, is less sensitive to the liquid-to-air momentum ratio, the growth of q

promotes both a higher penetration of the jet and a better dispersion.

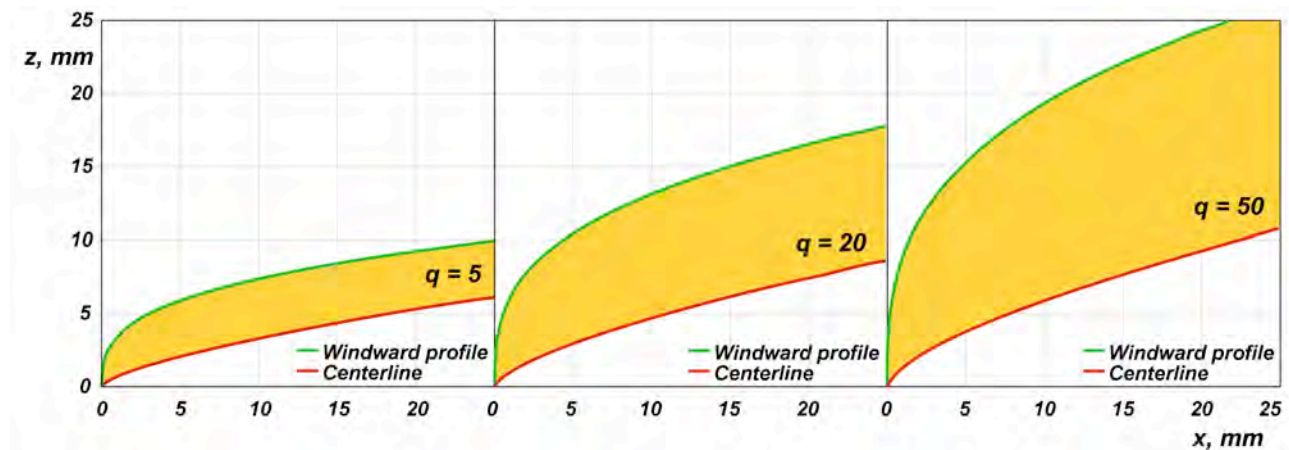


Figure 9.1. Behavior of jet trajectory (green line) and spray centerline (red line) for several values of the liquid-to-air momentum ratio q . The area in yellow represents a measure of the level of dispersion of the liquid in the gas phase.

Following a procedure analogous to the one reported in chapter 6, the point where the normal to the centerline intercepts the trajectory line was determined in analytical way. As a consequence of the simplified functional form of equations (2) and (3), the calculus passes through the solution of a cubic equation, which can be accomplished analytically by resorting to the Tartaglia's formula. The final result is an analytical expression of the difference between the angles α_T and α_C of trajectory and centerline with respect to the x axis, both being function of the momentum ratio and of the injection diameter. The behavior of the spray angle, as the spray progresses, is qualitatively the same as already observed for the point-to-point procedure used in chapter 6. The analytical expressions of either maximum or average value of the spray angle can be plotted as a function of q for a certain injection angle. The maximum value of the spray angle resulted to be practically constant with q . Calculations for nozzle diameter of 0.3 and 0.5 mm produced approximately the same maximum angle for every value of q , thus explaining why the point-to-point analysis did not show significant trend for this parameter. As regards the average value of the spray angle, the results of the analytical investigation produced the plot reported in figure 9.2, which plots the behavior of the average spray angle as a function of the momentum ratio. The blue and red lines

refer to 0.3 and 0.5 mm nozzle diameter data, respectively. Points represent experimental data detected by the point-to-point procedure introduced in chapter 6. Although the data are quite scattered, nevertheless the derived analytical formulation reproduce reasonably well the trend of the spray angle, which increases with q and is larger for higher nozzle diameter.

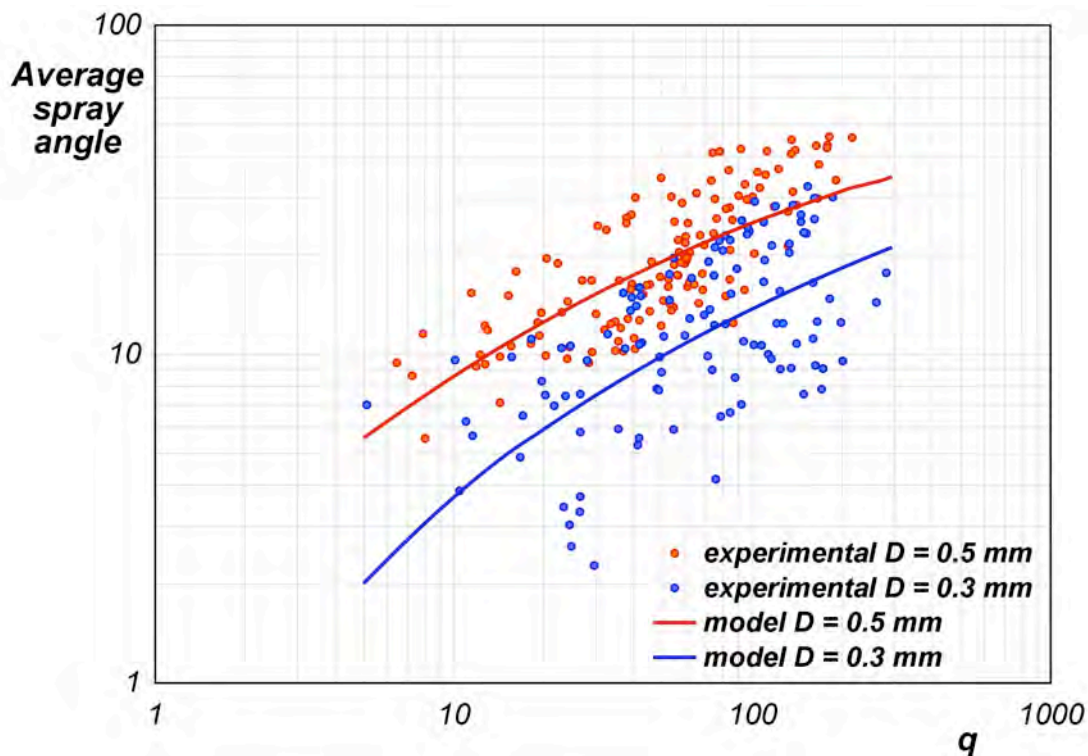


Figure 9.2. Plot of the calculated average spray angle as a function of the momentum ratio q and for two values of the injection diameter: 0.3 and 0.5 mm.

The study pointed out that the design of premixer must take care of achieving a good distribution of the liquid fuel in the channel. This goal can be accomplished by simultaneously optimizing the penetration and the spreading of the liquid spray. Both these two features of the spray largely depend on the momentum ratio and on the nozzle diameter. In particular by increasing the momentum ratio it is possible to improve the dispersion of the liquid phase, at the same time reducing the level of jet whipping, as pointed out by the study on the normalized intermittency index. On the other hand high values of the momentum ratio imply higher penetration, with increasing risk of impingement on the opposite wall of the premixer. The optimization process can take advantage from the chance to use the injection diameter as secondary tuner of the spray

characteristics. In particular this is possible since the design of actual premixer for gas turbines involves the resort to multiple orifices in a usually annular duct. Therefore a careful design can exploit these degrees of freedom to achieve optimal distribution of the fuel in the premixer, being matched the constraints on overall flow rate and air-fuel mass ratio.

9.3. Modeling the injection of liquids in crossflowing airstreams

The numerical model presented in this study is the result of a progressively improving strategy developed over the last years. Even though this thesis does not document the various steps, their track is recorded in the proceedings of the conferences where partial results were presented (Ragucci *et al.*, 2003, Bellofiore *et al.*, 2004, 2005). The guideline of this work was the development of a model able to capture the essential physical phenomena involved in the crossflow atomization process, with no or minimal resort to empirically tuned parameters. On the basis of the results presented in chapter 8, it can be stated that both the targets have been accomplished. The physical model, underlying the mathematical equations, describes a process much simpler than the actual physical phenomenon. The evolution of few variables, representative of the jet features, is evaluated in an eulerian frame of reference, except for the lagrangian tracking of the deformation parameter. The processes taken into account are jet bending, deformation and consumption. In particular the simplified sub-model for deformation considers only a single-parameter elliptical deformation, as well as the atomization model calculates only the liquid mass flow rate stripped from jet surface. With respect to the complex phenomenology described elsewhere in this thesis, numerical investigation demonstrated that accounting for few carefully selected sub-processes can capture the key physics ruling the penetration of the liquid jet.

As already pointed out elsewhere, the account for jet flattening marked a great improvement of the model agreement with experimental trajectories. This fact is attributable to a more accurate description of the effective area of the liquid jet exposed to the air drag. In particular the jet flattening (actually the convolution too) increases the efficiency of the drag forces promoting jet

bending and so a more deflected trajectory is predicted, according to experimental evidence. This plainly modeled drag enhancement is sufficient to predict realistic penetration of the jet, hence at this stage a deeper knowledge of the actual shape of the cross-section of the jet is not required.

The other relevant improvement documented in this thesis is the resort to a more realistic air velocity profile, taking into account the deceleration of the airflow near the duct walls due to the adherence condition. Also in this case, the more detailed description of the airflow was introduced in a simple manner, by attaching the velocity profiles near the wall, derived from the theory of turbulent boundary layers, to a flat velocity profile farther than the assessed boundary layer thickness. The result of this adjustment is a noticeable reduction of the discrepancy from experimental trajectory for all the operating conditions, and in particular the best improvement was achieved in conditions where the penetration of the jet in the premixer is lower. These were indeed the conditions where the original model, i.e. with flat air velocity profile, used to give worse results. The suggested explanation is that in that range the jet is more sensitive to the velocity field close to the injection sidewall, and so a more accurate description of this profile produces higher enhancement of the model.

The accuracy of the model was proved in the whole field of experimental conditions, which cover a wide range of all the relevant parameters. In particular kerosene jets resulted better predicted than water. The difference between the two liquids is little, but anyway it deserves a comment. Even if the general trend is good agreement between model and experimental evidence, due to the fact that the model adequately reproduces the conditions of dominant aerodynamic stripping, it can be supposed that the higher surface tension puts water jets slightly farther from these reference conditions, hence resulting in a faint worsening of model prediction ability.

It is noteworthy that the model does not embed any reference to the traumatic event of structural collapse of the liquid continuum. Nonetheless the model is able to describe the penetration of the jet. This evidence might appear in contrast with the other result, obtained from experiments, that the location of the breakdown point represents the fingerprint (i.e. the only distinctive identifying

characteristic) of a liquid jet. On the basis of further evidence already pointed out in this chapter, it seems possible to state that in the operating conditions of reference the mechanism of liquid stripping has a major influence on the interplay between inertial and drag forces responsible of jet trajectory. The other mechanism, that is the final collapse of the residual liquid column, probably involves only a minimal portion of the liquid, and so it allegedly has the main detectable effect on the whipping of the jet. Because of the progressive alignment of the jet with the airflow and the shrinking of jet thickness, far from the injection the aerodynamic interaction is less violent than in the initial stages of the atomization process. The continuous stripping of liquid from the corrugated jet surface is responsible for a weaker and weaker residual jet, which eventually becomes unable to oppose resistance to the airflow and so larger amplitude oscillations can develop of the bent profile of the leftovers fragments. As a consequence it must be inferred that the sudden loss of resilience connected to the occurrence of breakdown should be a natural, say predictable, consequence of the progressive jet evolution, since the description of the jet trajectory can be indifferently performed by means of either the breakdown point location or the numerical model, which does not account for such a sudden change.

Chapter 10. CONCLUSIONS

The behavior of a liquid jet in crossflow was experimentally investigated, choosing conditions comparable with the actual operation of a gas turbine. Liquid and air velocity, liquid properties and air pressure and temperature were varied in order to explore how some critical features of the jet depend on operating conditions. The investigation was carried out by adopting a flash shadowgraphic scheme. The about 300 explored conditions were used for both statistical analysis of the collected images and validation of a numerical model developed for the description of jet bending, flattening and atomization by transverse crossflow.

As regards the experimental work, a preliminary study, based on a diagnostic setup assuring higher magnification of the near field, aimed to clarify the mechanisms active in the initial stages of the atomization process. This phenomenological analysis provided a deeper insight of surface instabilities operating at different size and time scale on both the minor curvature (due to bending) and the sphere-like curvature of the jet. The concurrence of atomization features typical of either pressure or pneumatic atomizers was pointed out, as resulting from the variegate dependence of the spray characteristics on liquid and gas dynamic pressure. In addition the study proved that, in the range of investigated conditions, the characteristic values of surface tension and velocities place system operation in the full atomization regime, where stripping mechanisms are predominant. On the other hand, the very atomization regime is characterized by a weak dependence of the process on surface tension, due to the extremely high levels of Weber number. This statement is supported by the evidence that in all the explored condition the effect of capillary pressure on jet penetration, spray angle and spray intermittency is nearly negligible with respect to the one of aerodynamic pressure. The sole relevant influence of capillary pressure concerns the jet displacement in the gas-streamwise direction. Results of numerical simulation seem to indicate that surface tension affects the jet displacement, namely the breakdown point coordinate x_{jb} , through the mechanism of jet flattening, which is described by an adapted version of the TAB model, the only sub-model

embedding Weber number.

Statistical analysis investigated average behavior and instability characteristics of the spray windward profile and whole plume. In the former case, i.e. the line describing the upper boundary, the study provided information on the trajectory (from the average behavior) and the breakdown (from the variance) of the liquid jet. In the latter case, that is the surface intercepted by the spray plume, the statistical investigation was applied to both native and binary images. The result is the definition of some promising tools for the evaluation of ensemble features of the spray, namely liquid dispersion and spray unsteadiness.

The trajectory of the liquid jet has always the same shape, well described by a power law functional expression, whatever are the liquid injected or the operating conditions, whereas the length and aspect ratio of this curve scale with two parameters, namely the coordinates of the breakdown point. These scaling factors were empirically correlated with some dimensionless parameters. In particular z_{jb} strongly depends on the liquid-to-air momentum ratio, as already largely pointed out in literature. The other parameter, x_{jb} , depends mainly on the aerodynamic Weber number. Basing on the experimental evidence an empirical model has been proposed to describe the behavior of a liquid jet in crossflow. This model predicts a predominant influence of the momentum ratio on the jet trajectory, while the effect of capillary pressure is almost ruled out. The proposed correlation allows predicting the behavior of the jet up to the breakdown point and has been experimentally validated in the range of q between 5 and 200 and We_{aero} between 10 and 400 circa, at air pressure from 1.0 up to 2.0 MPa and air temperature from 300 up to 600 K.

A numerical model capable of describing the trajectory of a liquid jet injected in a high pressure and velocity air crossflow was implemented and validated against a set of about 300 experimental data obtained in condition significant to the real operating conditions of gas turbines. The model agreement resulted to be quite satisfactory over the whole range of investigated parameters. The progressive introduction of a more detailed description of the effective jet surface exposed to the air

drag (by means of the deformation sub-model) and of the actual air velocity profile (by means of boundary conditions accounting for the adherence condition close to the walls) improved the predictive ability of the model, resulting in rms error, calculated over the whole trajectory, generally better than empirical models available in literature. On the other hand the development of the model was able to preserve a substantial plainness, making it handier than other - usually complex - numerical models. Further remark deserves the total absence of resorting to empirically tuned parameters. Equations and parameters of the model derive from either theoretical assumption or literature evidences. This makes the model confidently reliable in all the conditions where a full atomization regime is developed.

Chapter 11. BIBLIOGRAPHIC REFERENCES

1. Adelberg M. (1967): Breakup rate and penetration of a liquid jet in a gas stream, *AIAA Journal*, 5(8), pp. 1408-1415.
2. Badr H.M. and Kocabiyik S. (1997): Symmetrically Oscillating Viscous Flow over an Elliptic Cylinder, *Journal of Fluids and Structures*, 11(7), pp. 745-766.
3. Baranovsky S.I. and Schetz J.A. (1978): An Experimental Investigation of Methods to Increase the Liquid Jet Penetration into Supersonic Flow, AFOSR-TR-78-1300, Air Force Office Of Scientific Research, Bolling Air Force Base, D. C. June 1978.
4. Battino R., Rettich T.R., Tominaga T. (1984): The Solubility of Nitrogen and Air in Liquids, *J. Phys. Chem. Ref. Data*, 13, 563-600.
5. Bayvel L. and Orzechowski Z. (1993): Liquid Atomization, Taylor and Francis, Washington, DC, USA.
6. Becker J. and Hassa C. (2000): Plain Jet Kerosene Injection into High Temperature, High Pressure Crossflow with and without Filmer Plate, *Proc. 8th Int. Conference on Liquid Atomization and Spray System (ICLASS-2000)*, Pasadena, CA, July 2000.
7. Becker J. and Hassa C. (2002): Breakup and Atomization of a Kerosene Jet in Crossflow at Elevated Pressure, *Atomization and Sprays*, 11(1-3), pp. 49-67.
8. Bellofiore A., Cavaliere A., Ragucci R. (2004): Atomization and Bending of Coherent Jets in Crossflow, *Proceedings of the Joint Meeting of the Italian and Greek Sections of the Combustion Institute*, Corfu, Greece, June 2004.
9. Bellofiore A., Di Martino P., Cavaliere A., Ragucci R. (2005): Atomization and Bending of Coherent Deformed Jets in Crossflow, *Proc. European Combustion Meeting*, Louvain-la-Neuve, Belgium, April 2005.
10. Callaghan E.E. and Ruggeri R.S. (1948): Investigation of the Penetration of an Air Jet Directed

Perpendicularly to an Air Stream, NACA Technical Note TN-1615.

11. Cavaliere A., Ragucci R., D'Alessio A., Noviello C. (1991): Atomization and Evaporation of Diesel Sprays in High-Pressure and High-Temperature Environments, *Atomization and Sprays*, 1(4), pp. 401-419.
12. Cavaliere A., Ragucci R., Noviello C. (2003): Bending and Break-up of a Liquid Jet in a High Pressure Airflow. *Experimental Thermal and Fluid Science*, 27(4), pp. 449-454.
13. Chelko L.J. (1950): Penetration of Liquid Jets into a High-Velocity Air Stream, NACA Report RM E50F21.
14. Chen T.H., Smith C.R., Schommer D.G., Nejad A.S. (1993): Multi-Zone Behavior of Transverse Liquid Jet in High-Speed Flow, *Proc. 31st AIAA Aerospace Sciences Meeting and Exhibit*, Reno, NV, January 1993.
15. Clark B.J. (1964): Breakup of a Liquid Jet in a Transverse Flow of Gas, NASA Technical Note TN D-2424.
16. Delplanque J-P. and Sirignano W.A. (1994): Boundary Layer Stripping Effects on Droplet Transcritical Convective Vaporization, *Atomization and Sprays*, 4(3), pp. 325-349.
17. Dennis S.C.R. and Young P.J.S. (2003): Steady Flow past an Elliptic Cylinder Inclined to the Stream, *Journal of Engineering Mathematics*, 47(2), pp. 101-120.
18. Eggers J. (1997): Nonlinear Dynamics and Breakup of Free-Surface Flows, *Review of Modern Physics*, 69, pp. 865-930.
19. Gooderum P.B. and Bushnell D.M. (1972): Atomization, Drop Size, and Penetration for Cross-Stream Water Injection at High-Altitude Reentry Conditions with Application to the RAM C-I and C-III Flights, NASA Technical Note TN D-6747.
20. Han J. and Tryggvason G. (1999): Secondary Breakup of Axisymmetric Liquid Drops. I. Acceleration by a Constant Body Force, *Physics of Fluids*, 11(12), pp. 3650-3667.
21. Heister S.D., Nguyen T.T., Karagozian A.R. (1989): Modeling of Liquid Jets Injected

- Transversely into a Supersonic Crossflow, *AIAA Journal*, 27(12), pp. 1727-1734.
22. Hojnacki J.T. (1972): Ramjet Engine Fuel Injection Studies, AFAPL-TR-72-76, Air Force Aero Propulsion Laboratory, Wright-Patterson Air Force Base, OH, USA, November 1972.
 23. Igra D. and Takayama K. (2001): Investigation of Aerodynamic Breakup of a Cylindrical Water Droplet, *Atomization and Sprays*, 11(2), pp. 167-185.
 24. Inamura T. and Nagai N. (1985): The Relative Performance of Externally and Internally Mixed Twin-Fluid Atomisers, *Proc. 3rd Int. Conference on Liquid Atomization and Spray System (ICLASS-85)*, London, UK, July 1985, pp. IIC/2/1-11.
 25. Inamura T. and Nagai N. (1997): Spray Characteristics of Liquid Jet Traversing Subsonic Airstreams, *Journal of Propulsion and Power*, 13(2), pp. 250-256.
 26. Ingebo R.D. (1967): Penetration of Drops into High-Velocity Airstreams, NASA TM X-1363.
 27. Ingebo R.D. and Foster H.H. (1957): Drop-Size Distribution for Crosscurrent Breakup of Liquid Jets in Airstreams, NACA Technical Note TN-4087.
 28. International Association for Properties of Water and Steam – IAPWS (2004): Release on Surface Tension of Ordinary Water Substance, September 2004, available on the website <http://www.iapws.org>
 29. Khosla S. and Crocker D.S. (2004): A Boundary Layer Stripping CFD Model for Shear Regime Atomization of Plain Liquid Jets in Cross Flow, *Proc. ILASS-Americas Conference*, Arlington, VA, USA, May 2004.
 30. Kihm K.D., Lyn G.M., Son S.Y. (1995): Atomization of Cross-Injecting Sprays into Convective Air Stream. *Atomization and Sprays*, 5(4-5), pp. 417-433.
 31. Kropinski M.C.A., Ward M.J., Keller J.B. (1995): A Hybrid Asymptotic-Numerical Method for Low Reynolds Number Flows Past a Cylindrical Body, *SIAM Journal on Applied Mathematics*, 55(6), pp. 1484-1510.
 32. Lefebvre A.H. (1989): *Atomization and Sprays*, Hemisphere Publishing Corporation, New

York, USA.

33. Lefebvre A.H. (1995): The role of fuel preparation in low-emission combustion, *J. Eng. Gas Turbine Power*, 117(4), pp. 617-654.
34. Madabhushi R.K. (2003): A Model for Numerical Simulation of Breakup of a Liquid Jet in Crossflow, *Atomization and Sprays*, 13(4), pp. 413-424.
35. Masuda B.J. and McDonnell V.G. (2006): Penetration of a Recessed Distillate Liquid Jet into a Crossflow at Elevated Pressure and Temperature, *Proc. 10th Int. Conference on Liquid Atomization and Spray System (ICLASS-06)*, Kyoto, Japan, August-September 2006.
36. Mazallon J., Dai Z., Faeth G.M. (1999): Primary Breakup of Nonturbulent Round Liquid Jets in Gas Crossflows, *Atomization and Sprays*, 9(3), pp. 291-312.
37. Mittal R. and Balachandar S. (1996): Direct Numerical Simulation of Flow Past Elliptic Cylinders, *Journal of Computational Physics*, 124, pp. 351-367.
38. Nasr G.G., Yule A.J., Bendig L. (2002): *Industrial Sprays and Atomization*, Springer-Verlag, London, UK.
39. Nejad A.S. and Schetz J.A. (1984): Effect of Viscosity and Surface Tension on a Jet Plume in Supersonic Crossflow, *AIAA Journal*, 22(4), pp. 458-459.
40. Nguyen T.T. and Karagozian A.R. (1992): Liquid Fuel Jet in Subsonic Crossflow, *Journal of Propulsion and Power*, 8(1), pp. 21-29.
41. O'Rourke P.J. and Amsden A.A. (1987): The Tab Method for Numerical Calculation of Spray Droplet Breakup, SAE paper 87-2089.
42. Oda T., Nishida K., Hiroyasu H. (1994): Characterization of Liquid Jet Atomization across a High Speed Airstream by Laser Sheet Tomography, *Proc. 6th Int. Conference on Liquid Atomization and Spray System (ICLASS-94)*, Rouen, France, July 1994.
43. Peyret R. (2000): *Computational Fluid Mechanics*, Academic Press, London, U.K.
44. Pilch M. and Erdman C.A. (1987): Use of Breakup Time Data and Velocity History Data to

- Predict the Maximum Size of Stable Fragments for Acceleration-Induced Breakup of a Liquid Drop, *Int. Journal of Multiphase Flow*, 13(6), 741-757.
45. Rachner M., Becker J., Hassa C., Doerr T. (2002): Modelling of the Atomization of a Plain Liquid Fuel Jet in Crossflow at Gas Turbine Conditions, *Aerospace Science and Technology*, 6(7), pp. 495-506.
46. Ragucci R. and Cavaliere A. (2002): Identification of Cross-Flow Liquid Jet Structures by means of Statistical Image Evaluation, *Proc. 18th ILASS-Europe Conference*, Zaragoza, Spain, September 2002, paper #89.
47. Ragucci R., Bellofiore A., Carulli G., Cavaliere A. (2003): Momentum Coherence Breakdown of Bending Atomizing Liquid Jet, *Proc. 9th Int. Conference on Liquid Atomization and Spray System (ICLASS-03)*, Sorrento, Italy, July 2003, pp. 1-13.
48. Ragucci R., Bellofiore A., Cavaliere A. (2004): Statistical Evaluation of Dynamics and Coherence Breakdown of Kerosene and Water Jets in Crossflow, *Proc. 19th ILASS-Europe Conference*, Nottingham, U.K., September 2004, p. 44-49.
49. Ragucci R., Bellofiore A., Cavaliere A. (2007): Trajectory and Momentum Coherence Breakdown of a Liquid Jet in High-Density Air Crossflow, accepted for publication on *Atomization and Sprays*.
50. Ragucci R., Cavaliere A., D'Amico R. (2000): Atomization of a Liquid Jet in Gas-Turbine Configuration, *Proc. 8th Int. Conference on Liquid Atomization and Spray System (ICLASS-2000)*, Pasadena, CA, USA, July 2000, pp. 994-1001.
51. Ranger A. and Nicholls J. A. (1969): Aerodynamic Shattering of Liquid Drops, *AIAA Journal*, 7(2), pp. 285-290.
52. Reitz R.D. (1987): Modeling Atomization Processes in High-Pressure Vaporizing Sprays, *Atomization and Spray Technology*, 3(4), pp. 309-337.
53. Reitz R.D. and Bracco F.V. (1982): Mechanism of Atomization of a Liquid Jet, *Physics of*

- Fluids*, 25(10), pp. 1730-1742.
54. Reitz R.D. and Diwakar R. (1987): Structure of High-Pressure Fuel Sprays, *SAE Transactions*, 96(5), pp. 492-509.
55. Sallam K.A., Aalburg C., Faeth G.M. (2004): Breakup of Round Nonturbulent Liquid Jets in Gaseous Crossflow, *AIAA Journal*, 42(12), pp. 2529-2540.
56. Schetz J.A., Kush E.A. Jr., Joshi P.B. (1980): Wave Phenomena in Liquid Jet Breakup in a Supersonic Crossflow, *AIAA Journal*, 18, pp. 774-778.
57. Sedarsky D., Paciaroni M., Linne M., Meyer T., Kiel B., Gord J. (2006): Ballistic Imaging of the Near Field for Jets in Gaseous Crossflow, *Proc. 10th Int. Conference on Liquid Atomization and Spray System (ICLASS-06)*, Kyoto, Japan, August-September 2006.
58. Sirignano W.A. (1999): Fluid Dynamics and Transport of Droplets and Sprays, Cambridge University Press, Cambridge, UK.
59. Spadaccini L.J. and TeVelde J.A. (1982): Autoignition Characteristics of Aircraft-Type Fuels, *Combustion and Flame*, 46, pp. 283-300.
60. Spangler C.A., Hilbing J.H., Heister S.D. (1995): Nonlinear Modeling of Jet Atomization in the Wind-Induced Regime, *Physics of Fluids*, 7(5), pp. 964-971.
61. Stiesch G. (2003): Modeling Engine Spray and Combustion Processes, Springer-Verlag, Berlin, Germany.
62. Tambe S.B., Jeng S.-M., Mongia H., Hsiao G. (2005): Liquid Jets in Subsonic Crossflow, *Proc. 43rd AIAA Aerospace Sciences Meeting and Exhibit*, Reno, NV, USA, January 2005, AIAA 2005-731.
63. Tanner F.X. (1998): Liquid Jet Atomization and Droplet Breakup Modeling of Non-Evaporating Diesel Fuel Sprays, *SAE 1997 Transactions: Journal of Engines*, 106(3), pp. 127-140.
64. Tanno S., Miura T., Ohtani S. (1985): Atomisation of High-Velocity Liquid by Pneumatic

- Nozzle, *Proc. 3rd Int. Conference on Liquid Atomization and Spray System (ICLASS-85)*, London, UK, July 1985, pp. LP/VB/6/1-8.
65. Taylor G.I. (1963): The Shape and Acceleration of a Drop in a High-Speed Air Stream, in *The Scientific Papers by G.I. Taylor*, edited by G.K. Batchelor (Cambridge University Press, Cambridge, 1963), 3, pp. 457-464.
66. Wang J., Wang Y.J., Im K.S., Fezzaa K., Lee W.K. (2006): X-Ray Visions of Air-Assisted Sprays: From Radiography to Quantitative Phase-Contrast Imaging, *Proc. 10th Int. Conference on Liquid Atomization and Spray System (ICLASS-06)*, Kyoto, Japan, August-September 2006.
67. Wu P.K. and Faeth G.M. (1993): Aerodynamic Effects on Primary Breakup of Turbulent Liquids, *Atomization and Sprays*, 3(3), pp. 265-289.
68. Wu P.K., Kirkendall K.A., Fuller R.P., Nejad A.S. (1997): Breakup Processes of Liquid Jets in Subsonic Crossflows, *Journal of Propulsion and Power*, 13(1), pp. 64-73.
69. Wu, P.K., Kirkendall, K.A., Fuller, R.P. (1998): Spray Structures of Liquid Jets Atomized in Subsonic Crossflows, *Journal of Propulsion and Power*, 14(2), pp. 173-182.
70. Yang H.Q. (1992): Asymmetric Instability of a Liquid Jet, *Physics of Fluids*, 4(4), pp. 681-689.
71. Yates C.L. (1972): Liquid Injection into a Supersonic Stream, AFAPL-TR-97, Air Force Aero Propulsion Laboratory, Wright-Patterson Air Force Base, OH, 1972, Vol. 1.
72. Yoon S.S. and Heister S.D. (2004): A Nonlinear Atomization Model Based on a Boundary Layer Instability Mechanism, *Physics of Fluids*, 16(1), pp. 47-61.